Dissertations, Theses, and Masters Projects   Theses, Dissertations, & Master Projects

1972

An investigation of one and two state molecular systems based on the results of elastic differential scattering experiments

Stephen Michael Bobbio
College of William & Mary - Arts & Sciences

72-16,964

BOBBIO, Stephen Michael, 1943-
    AN INVESTIGATION OF ONE AND TWO STATE MOLECULAR
    SYSTEMS BASED ON THE RESULTS OF ELASTIC
    DIFFERENTIAL SCATTERING EXPERIMENTS.

    The College of William and Mary in Virginia,
    Ph.D., 1972
    Physics, molecular

AN INVESTIGATION OF ONE AND TWO STATE MOLECULAR

SYSTEMS BASED ON THE RESULTS OF ELASTIC

DIFFERENTIAL SCATTERING EXPERIMENTS

———————

A dissertation

Presented to

The Faculty of the Department of Physics

The College of William and Mary in Virginia

———————

In Partial Fulfillment

of the Requirements for the Degree of

Doctor of Philosophy

———————

by

Stephen Michael Bobbio

1971

APPROVAL SHEET

This dissertation is submitted in partial fulfillment of

the requirements for the degree of

Doctor of Philosophy

Stephen Michael Bobbio
Stephen Michael Bobbio

Approved, November 1971

Roy L. Champion

R. Crossfield

E. A. Remler

Megin T. Ralph

L. D. Dorenspike

interest in his work.

He finally acknowledges his colleague Mr. W. G. Rich with whom he has worked closely over the past two years. He thanks him for a multitude of big, small, and intermediate things beginning with the duoplasmatron and ending with the completion of this dissertation.

TABLE OF CONTENTS

LIST OF FIGURES

LIST OF TABLES

ABSTRACT

In this dissertation we discuss two distinct types of molecular systems. In both cases our analyses are based on the low energy (5 eV $\leq E \leq$ 40 eV) elastic differential scattering experiments which we have performed.

The first type of system which we consider concerns the scattering of protons by rare-gas atoms, specifically: H^+ + Ar and H^+ + Kr. Here it is seen that the interference phenomena manifest in the experimental differential cross sections are well understood in terms of semiclassical theory based on a single intermolecular potential corresponding to the ground state of the molecular ion. Furthermore, using a new method, we invert the well-resolved experimental data to find this intermolecular potential.

The second type of system which we consider concerns the elastic scattering of He^+ by Ne. In this case the perturbations seen in the experimental cross section are not due to a single intermolecular potential. Instead, they are attributed to the lowest energy "crossing" of the $(NeHe)^+$ potential curves. In our analysis we have shown that the most modern curve crossing theory predicts a differential cross section which is entirely consistent with our experimental observation. Moreover, the semiclassical method may be extended to explain much of what is seen in the data.

AN INVESTIGATION OF ONE AND TWO STATE MOLECULAR
SYSTEMS BASED ON THE RESULTS OF ELASTIC
DIFFERENTIAL SCATTERING EXPERIMENTS

A Thesis Dedicated to
Jigger, Advocate, and Lunsford

I. INTRODUCTION

The role of differential elastic scattering in the determination of intermolecular forces has increased considerably in the past decade. This has been due to continuous improvements in experimental techniques associated with atom-atom and ion-atom collisions and to a desire to complete a theoretical problem which had its genesis in the early days of quantum mechanics but which had relatively little effort devoted to it until recently. This fundamental problem is the formal inversion of differential elastic scattering data to obtain the corresponding intermolecular potential. It is to this problem that we will address ourselves in Section III.

Calculations based on phenomenological potentials (and the JWKBL approximation) have been used in various iterative schemes to fit calculated differential cross sections to those experimentally observed.[1] Numerical calculations of the differential cross section which utilize up to several thousand partial waves are common. Approximations such as those by Ford and Wheeler,[2] simplify the numerical problem of calculating the differential cross sections and give physical insight into the origin of oscillatory behavior observed in some differential cross sections. These various approximations coupled with phenomenological potentials have proved extremely valuable in semi-quantitative interpretations of

2

the experimental observations. We shall develop the semi-classical approximation to provide insight into the features of the differential cross section; however, for quantitative inversion of the intermolecular potential, V(R), we shall use two new techniques. The first, which involves Regge poles, is due to E. A. Remler[3] and allows the phase shift function, η_ℓ , to be constructed from the high resolution experimental cross section. The second technique, the transformation method of Vollmer,[4] permits the calculation of V(R) from η_ℓ .

The specific molecular systems which are discussed in Section III (ArH$^+$, KrH$^+$) are both bound by several eV. The collision energies for which the differential scattering measurements are made are sufficiently low such that the elastic channel is the only one which is important. However, the collision energies are above the minimum for which barrier penetration and hence (classical) orbiting can occur.

The one state elastic scattering experiments and analyses in Section III form a well-understood closed system. The problem of the two state (NeHe)$^+$ system which we shall undertake in Section IV is considerably more difficult and our discussion is more open-ended. In this case the perturbations which we observe in the elastic scattering cross section are not due to a single potential but rather are caused by the inelastic effect of curve crossing. Here, the potential

curves corresponding to two distinct separate atom limits of the molecular system cross each other at some small internuclear separation. In the vicinity of this crossing the system, originally prepared in the ground state, may make a transition to the other potential curve and exit inelastically from the collision region.

The Stanford Research Institute group has studied the $(NeHe)^+$ system extensively before.[5] Our low energy, large angle differential cross section experiments reported in Section IV have allowed the effect of the lowest energy crossing of the $(NeHe)^+$ system to be isolated. Furthermore, the ab initio calculation of Sidis[6] for the potentials and coupling term as well as the semi-quantal technique of Delos[7] to solve the problem of the nuclear motion and connect the solution with the scattering amplitude have allowed the elastic differential cross section to be more accurately calculated than previously. This calculation compares favorably with our 40 eV He^+ + Ne elastic scattering experiment. Moreover, on the basis of this calculation the features observed in the differential cross section may be discussed in semiclassical terms. By comparison to the single channel work the two state calculation is considerably more involved; therefore, at the end of Section IV, a possible parameterization of the curve crossing problem is given which may facilitate future treatment of this and more complex systems.

II. EXPERIMENTAL APPARATUS AND TECHNIQUE

In this section we shall briefly describe the experimental apparatus and how it is utilized in performing elastic differential scattering experiments.

IIA. Experimental Apparatus

A schematic diagram of the apparatus is shown in figure 1. The main vacuum chamber is a 30" diameter aluminum cylinder of 26" height which is evacuated by a liquid nitrogen trapped 6" mercury diffusion pump. The cylinder is connected via the primary momentum analyzer tube (6" radius of curvature, 90° section) to a smaller chamber which is evacuated by two 2" mercury pumps which are also liquid nitrogen trapped. The pressure in each vacuum chamber is monitored by an ionization gauge.

The ion source, used in our elastic scattering experiments, was of the duoplasmatron variety which was originally devised by Von Ardenne. The model we are presently using is a scaled version of the source used by the experimental group at the Stanford Research Institute and its operational characteristics are well documented.[8]

Positive ions are extracted from the source and accelerated through a series of electrostatic lenses, subsequently

SCHEMATIC
DIAGRAM
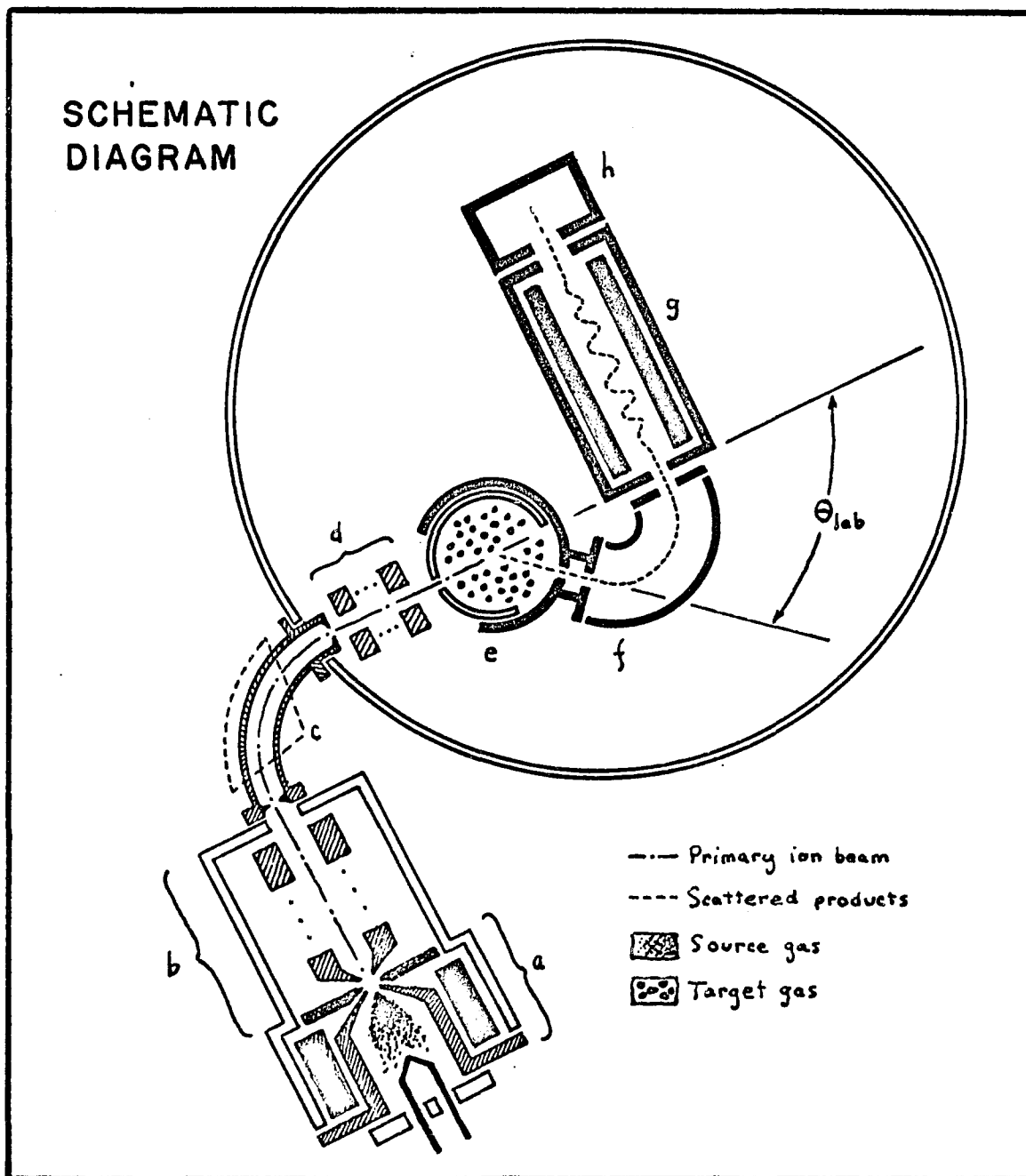
Figure 1: (a) duoplasmatron ion source, (b) accelerating
and focusing electrostatic lens system, (c) magnetic mass
spectrometer, (d) retardation lens system, (e) collision
chamber, (f) energy analyzer, (g) radio frequency mass
spectrometer, (h) particle multiplier. Please note the
product analysis system, consisting of elements f, g, and
h is shown in heavy black lines in the main vacuum chamber.
Furthermore, no attempt has been made to indicate the scale
of the various elements.

being focused onto the entrance slit of a second order focusing magnetic mass spectrometer. Upon leaving the mass spectrometer the ions are retarded by another set of lenses and focused onto the entrance slit of the collision chamber.

The collision chamber is a small vertical cylinder (with radius equal to .45" and height 1.9") inside the main vacuum chamber. It is sealed at the top and bottom, and target gas is admitted through a small aperature in the wall of the cylinder. In order to attain a sufficiently high density of scattering centers within the collision chamber (pressure $\sim 10^{-4}$ torr) and simultaneously maintain a high vacuum on the outside, the entrance and exit slits of the collision chamber must be small. At the same time product ions must be detectable over a range of approximately 90°. To realize both these ends the collision chamber is made of two closely fitting coaxial cylinders. The inner cylinder, which is fixed in the main vacuum chamber, has a narrow (~ 30 mils) entrance slit but its exit slit is, in reality, a horizontal slot whose height is the same as that of the entrance slit but extends for about 90° around the circumference of the inner cylinder. The outer cylinder, which rotates with the detection system, has a 90° entrance slot but its exit slit is very narrow. Within the collision chamber are two electrically isolated plates which enable one to determine the amount of ion current entering the collision chamber. This arrangement

is shown in figure 2. By placing a small voltage between the two plates the "slow" ions which are the products of certain charge transfer reactions may be deflected onto one of the plates and the current measured with an electrometer. If the total cross section is known for such a reaction, the ratio of the deflected product current to primary beam intensity enables one to determine the density of scattering centers in the collision region.
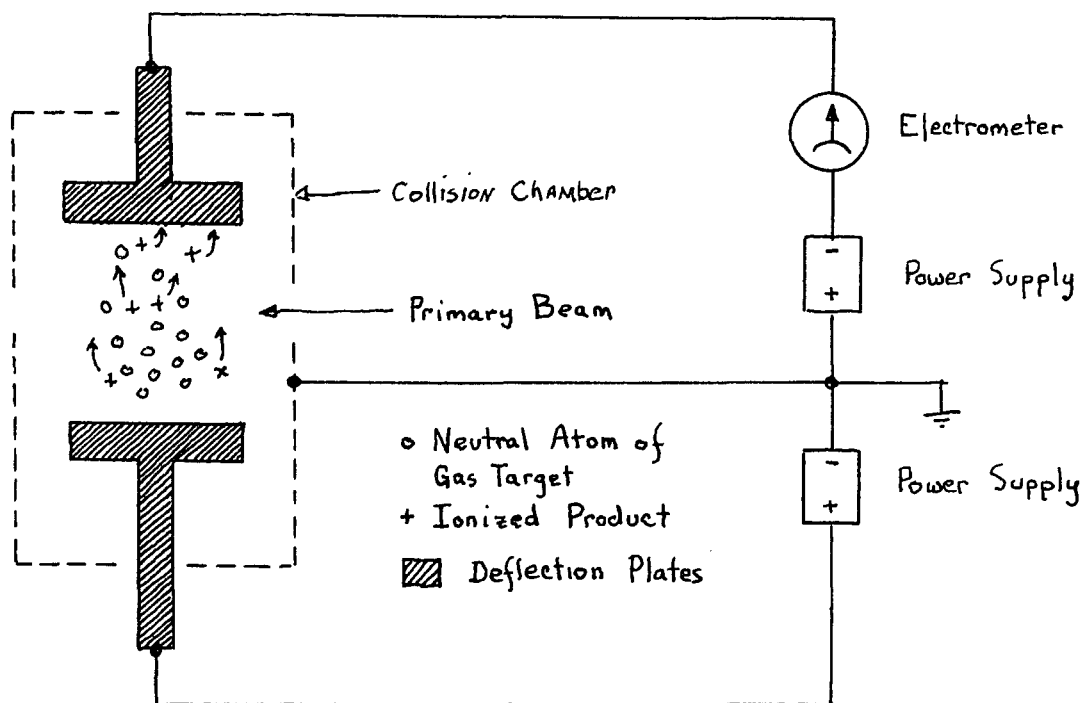
Figure 2: deflection plate detail.

The first element in the detection system is an energy analyzer which is essentially a 127° section of a cylindrical capacitor. The filtering action of this device depends only on the kinetic energy to charge ratio of the product ion. The energy analyzer is calibrated by accelerating the charge transfer products of the reactants He^+ + He (which for $\Theta \sim 0°$ have a kinetic energy $\leq kT$) through a known potential and into the analyzer. The second element of the detection system is a radio frequency mass spectrometer which was originally designed by Paul[9] and, since it is relatively small and very efficient, is admirably suited to its present application. The final element in the detection system is a Bendix particle multiplier. This device employs a continuous dynode surface and crossed $\vec{E}$ and $\vec{H}$ fields for the electron cascading process as well as a large entrance aperature for the efficient detection of product ions. The output of the multiplier is fed to an electrometer (for high ion current) or to a single particle counting system (for lower intensities). The entire multiplier unit is shielded with highly permeable material; and a fine mesh grid, maintained at low voltage, is placed before the entrance of the particle multiplier to prevent "creep-in" fields from entering the radio frequency mass spectrometer.

IIB. Experimental Technique

In this section we shall outline the performance of a typical experiment.

After the entire system is evacuated to about 10^{-6} torr gas is admitted to the duoplasmatron source. An arc (typically 1.5 amp electron current) is struck and a plasma is formed within the source. Ions are then extracted from the most dense portion of this plasma (near the anode), accelerated, momentum analyzed, retarded, and collected on the outside surface of the collision chamber. The primary beam ion current is measured at this point with an electrometer.

Momentum analysis of the primary beam proves necessary since the duoplasmatron produces many species of positive ions with broad energy spectra. If, for instance, the proton source is H_2 , the species H^+, H_2^+ and H_3^+ are extracted with the approximate intensity ratios 2:1:3. Furthermore, only about one part in 350 of the remaining H^+ ion beam has the required energy $\left(E = \Delta V(1 \pm .01) \right.$ where ΔV is the potential difference between anode and analyzer) to pass through the momentum analyzer.

After a current of sufficient intensity is collected at the collision chamber the detection apparatus is set at 0° and the product energy analyzer is adjusted to pass the primary beam.

Obtaining a good ion beam is, of course, the crux of the experimental problem. What qualifies as "good" is a strong function of the type of experiment one wishes to perform. Parameters associated with a 5 eV H^+ beam were: more than 1 ηa. onto the collision chamber with an energy spread of .5 eV, and an angular full width at half maximum of less than 1° (as measured by the detection system). Just how to fulfill these conditions is not easy to explain, but is essentially a matter of experience. A few remarks can, however, be made.

All physical surfaces to which the ion beam is exposed must be regularly cleaned and coated with Aquadag (graphite in alcohol) to prevent space charge buildup. This is particularly important for defining slits and other narrow passages. In tuning the beam, D. C. potentials are placed on the various elements of the system. We have found the voltage profile in Table 1 to give good results.

Once a satisfactory primary beam is obtained, scattering gas is admitted to the collision chamber. Since the leakage rate of target gas into the chamber and the defining slits of the collision chamber are both small, an equilibrium situation exists; and for all practical purposes we have a static gas target for which the pressure and temperature are defined.[10] Since we have no way of accurately measuring this pressure, absolute cross sections cannot be determined.

Table 1: Experimental voltage profile

ELEMENT	POTENTIAL DIFFERENCE BETWEEN ELEMENT AND ANODE
Draw-out (first element of (b) in fig 1)	-5 volts
Second element of (b) in fig 1	-180 volts
Remainder of elements of (b) in fig 1	between -30 and -80 volts
Analyzer ((c) in fig 1)	-35 volts
Retard (first element of (d) in fig 1)	-10 volts
Remainder of elements of (d) in fig 1	between -5 and -20 volts
Collision chamber ((e) in fig 1)	- anode voltage

If the target gas pressure is too high multiple scattering events can occur. Their effect will be manifested by a smearing of fine structure (high frequency oscillations) frequently seen in the angular distribution of the scattered ions. These considerations as well as the total cross section charge exchange experiment previously mentioned have allowed us to adjust the target gas pressure such that high resolution differential scattering measurements are possible.

In performing the experiment we advance the detection system by one-third degree intervals and energy select the elastically scattered product ions which are counted using the particle multiplier (at high gain), a pulse preamplifier,

a pulse shaper/amplifier, and a single channel scaler/analyzer. The angle of observation is recovered as an analog voltage from a slide-wire potentiometer inside the vacuum system. Both angle and corresponding count rate are digitally recorded by a system which includes a teletype code converter unit, and a teletype printer mechanism, and an interface which sequentially addresses the digital voltmeter and scaler/analyzer.

As previously mentioned, the elastically scattered product must be energy selected at each laboratory angle. Accordingly, we will give a brief kinematic treatment which relates the energy loss of the product ion, ΔE_3, to the laboratory scattering angle χ. Letting the subscripts 1,2, 3, 4 refer to the incident, target, detected product, and undetected product particles we may express the conservation of energy and linear momentum for elastic scattering in the following way[11]

$$0 = \left(1 + \frac{M_3}{M_4}\right) E_3 - \left(1 - \frac{M_1}{M_4}\right) E_1 - \frac{2}{M_4} \left(M_1 M_3 E_1 E_3\right)^{1/2} \cos \chi$$

For elastic scattering of the incident ion $M_1 = M_3$, $M_2 = M_4$ consequently

$$\Delta E_3 = E_1 - E_3 = E_1 \left\{ 1 - \frac{M_1^2}{(M_1 + M_2)^2} \left[\cos \chi + \left(\frac{M_2^2}{M_1^2} - \sin^2 \chi \right)^{1/2} \right]^2 \right\}$$

For singly charged particles, a voltage which is equal to ΔE_3 accelerates the scattered ions to the entrance of the energy selector. Since only the elastically scattered product has, at this point, the energy E_1 it is the only component which can pass through the selector.

In order to obtain the center of mass differential cross section from the measured angular distribution two operations must be performed on the experimental data. The reaction volume shown in figure 3 is a function of the scattering angle χ; consequently its χ dependence must be taken into account
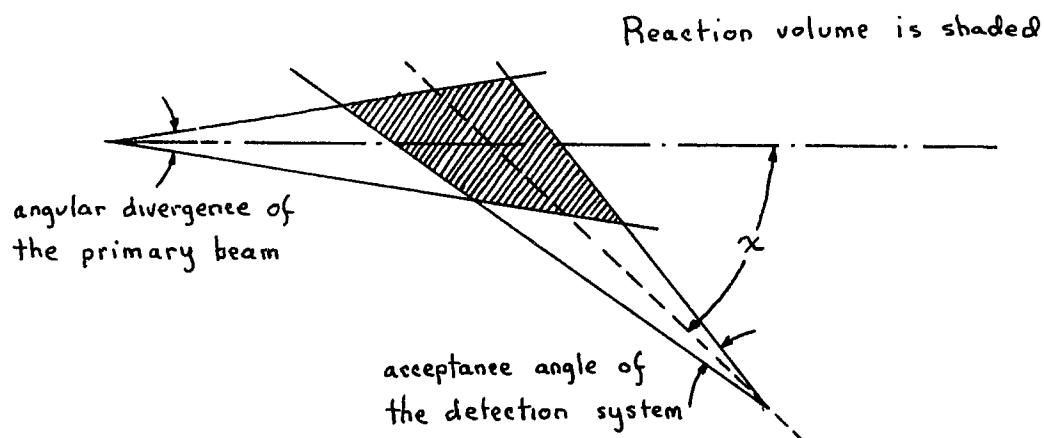
Figure 3: reaction volume.

This particular correction has been discussed in detail previously and will not be elaborated here.[11] It turns out that a knowledge of the apparatus geometry allows one to write the

corrected intensity, $I_c(\chi)$, as a function of the experimental intensity, $I_o(\psi)$, in the following way

$$I_c(\chi) = I_o(\chi)\, C(\chi)$$

Where $C(\chi)$ is the reaction volume correction which goes, for large χ, to $\sin\chi$; and is shown in figure 4.
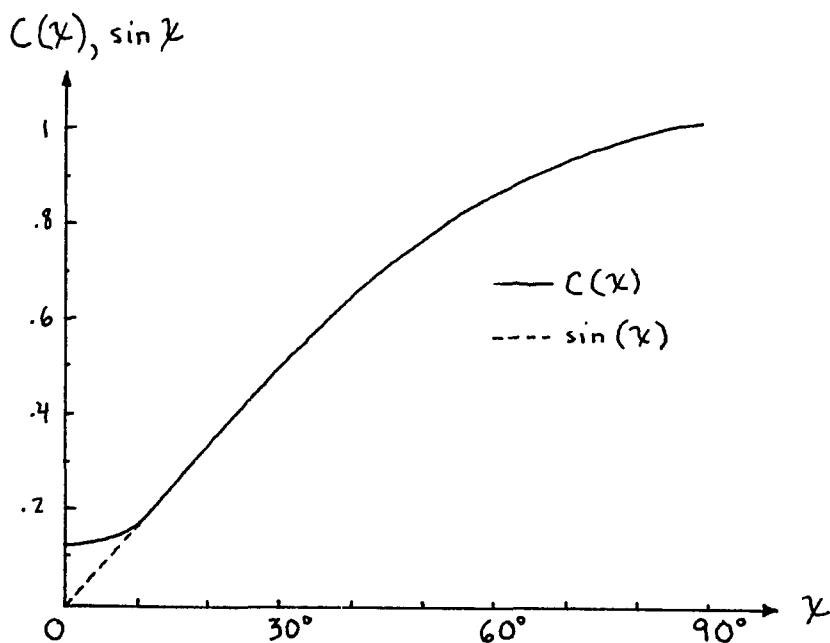
Figure 4: reaction volume correction as a function of scattering angle.

The corrected intensity must now be transformed into the center of mass coordinates. First we define the laboratory differential cross section $\sigma(\chi)$ as

$$\sigma(\chi)\, d\Omega_{lab} = \frac{\left(\begin{array}{c}\text{number of particles scattered}\\ \text{per unit time into } d\Omega_{lab}\end{array}\right)}{\left(\begin{array}{c}\text{number of incident particles}\\ \text{per unit area per unit time}\end{array}\right) \times \left(\begin{array}{c}\text{number of}\\ \text{scattering centers}\end{array}\right)}$$

$$\sigma(\chi) \, d\Omega_{lab} = \frac{1}{K} I_c(\chi) \, d\Omega_{lab}$$

where $d\Omega_{lab}$ is the differential solid angle in laboratory
coordinates and K is a constant which is proportional to
the incident intensity times the pressure of the target gas.
Since we do not know K exactly our experiments measure the
relative differential cross section. Making the C.M. trans-
formation we find that:

$$\tan\theta = \frac{\sin\chi}{(M_1/M_2) + \cos\chi}$$

and

$$\sigma(\theta) = \frac{\left|1 + \frac{M_1}{M_2}\cos\theta\right|}{\left(1 + \frac{M_1^2}{M_2^2} + 2\frac{M_1}{M_2}\cos\theta\right)^{3/2}} \cdot \frac{I_c(\chi)}{K}$$

where θ is the C.M. scattering angle.

Both the volume correction and the C.M. transformation
in the last equation are numerically applied to each set of
experimental data. The effect of these operations is to
smoothly increase the scattering intensity at larger scat-
tering angles, while neither one much affects the location
and periodicity of experimentally resolved oscillations in
the differential cross sections.

One further topic remains to be discussed; that is the

problem of the smearing of high frequency oscillations in
some observed differential cross sections. It would be
extremely useful to put this problem on a quantitative basis
but the complexity of the question presently precludes this.
We can at least point out the principal causes of this effect:
(1) the angular width of the primary beam, (2) the finite
angle subtended by the product analyzer and (3) the thermal
motion of the reactants. To facilitate comparison between
experimental data and calculated cross sections we have done
two things. First, we have convoluted the calculation of the
differential cross sections with a function thought to be
representative of the experimental resolution (this function
has typically had about the same angular width as the pri-
mary beam). The second method we have employed is much
more sophisticated. Utilizing a procedure developed by
G. E. Ioup[12] we have deconvoluted the experimental cross
section. The result of such a deconvolution may be seen
for the 5 eV H^+ + Ar scattering system in figure 5b. The
reader should note that we believe this latter technique
is reliable only insofar as it enhances the structure al-
ready seen in the original data (please compare figures 5a
and 5b.
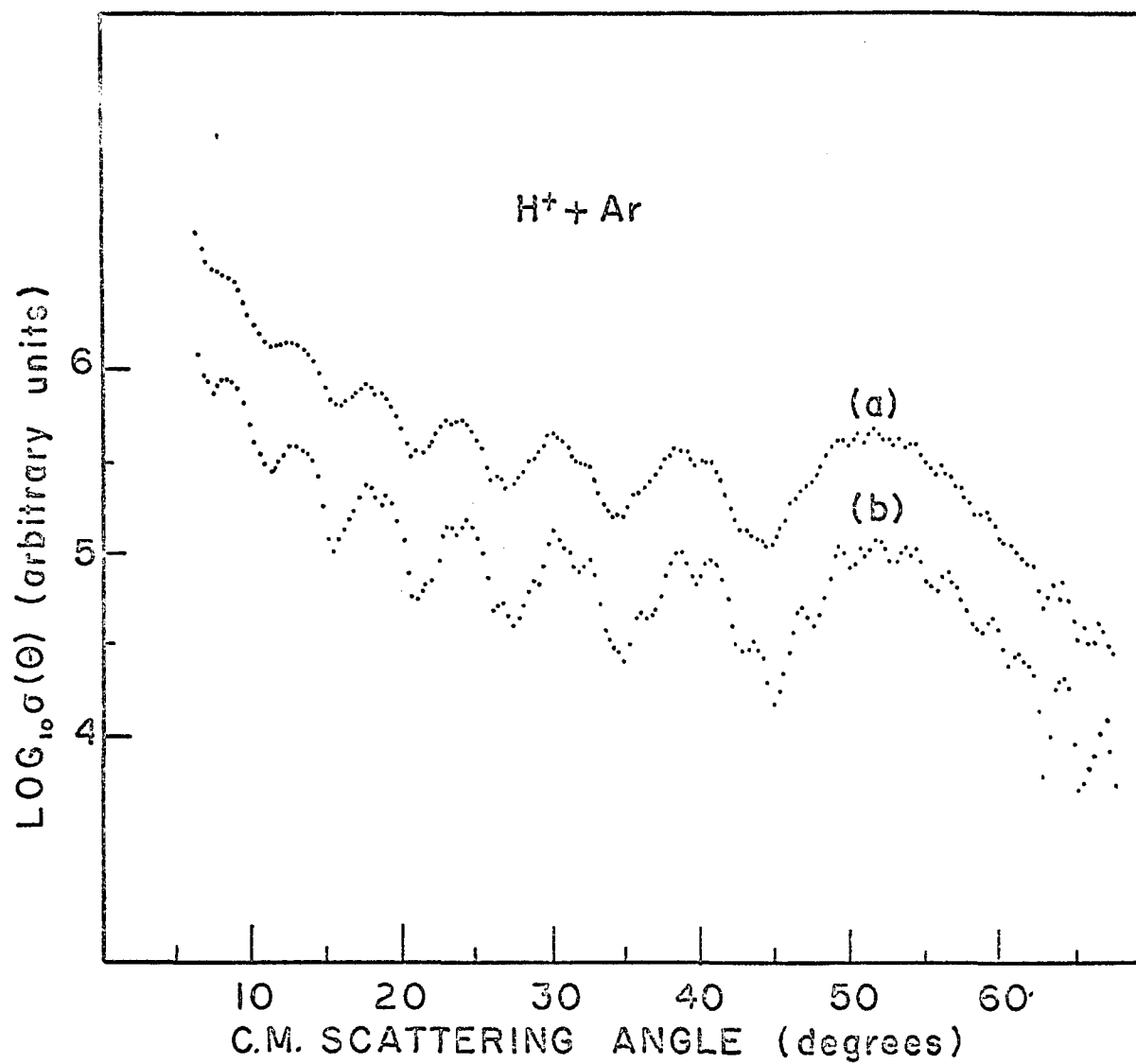
Figure 5: (a) experimental relative differential cross section, (b) deconvolution of the experimental differential cross section. Both curves pertain to the 5eV H^+ + Ar elastic scattering system.

III.   ELASTIC SCATTERING FOR
ONE STATE SPHERICALLY SYMMETRIC SYSTEMS

The focus of this section will be the low energy experimental differential cross section as typified by the H^+ + Ar 5 eV data shown in figure 5a. We will explain the structure seen in this experiment on the basis of semiclassical ideas which shall be developed in some detail. Further, using two new techniques (the Remler-Regge[3] and Vollmer[4] methods) which are also discussed herein, we will construct the inter-molecular potential from the experimental cross section.

Our discussion of this problem will begin with an explicit definition of the intermolecular potential and a reduction of the complete wave equation to the equivalent one particle Schroedinger equation involving this potenital. We shall then review the well-known partial wave[13] and JWKBL phase shift[14] methods which provide a connection between the solution to the reduced wave equation and the differential cross section. In the present case these methods allow accurate calculation of the differential cross section but give little insight into the nature of the structure seen in the experimental data. To afford such insight we shall use the deflection function of classical mechanics in a semiclassical way. That is, further approximations will be made to the partial wave method the result of which allows the differential cross section to be discussed in terms of the classical deflection function. At

different points in the development of these ideas we have
thought it appropriate to make some explicit connection with
our experiment, and have done so. Through Sections
IIIA and IIIB the differential cross section is viewed as
resulting from scattering by an intermolecular potential.
In Section IIIC we show, by using the Remler-Regge[3] and Vollmer[4]
methods, how this potential can be efficiently constructed from
the experimental data; while, in Section IIID we apply the
methods of IIIC to two particular experiments, H^+ + Ar and H^+
+ Kr.

IIIA. The Quantum Mechanical and JWKBL Methods

It will be shown that the results of the low energy H^+ + Ar and H^+ + Kr experiments are consistent with the scattering predicted by using a single elastic channel in the calculation. New theoretical work[15] on the $(ArH)^+$ system bears out our contention that only one channel need be considered. Since the basic thrust of our investigation is to recover the intermolecular potential from the scattering data we shall begin this section by indicating explicity in quantum mechanical terms what is meant by the intermolecular potential.

The Schroedinger equation for a system of N electrons and two nuclei may be written in center of mass coordinates as

$$(\text{III-1}) \quad \left[-\frac{\hbar^2}{2m_e} \sum_{i=1}^{N} \nabla_i^2 - \frac{\hbar^2}{2M} \nabla_R^2 + V(r_i, R) + \frac{Z_a Z_b e^2}{R} - E \right] \Psi = 0$$

where $\{\vec{r}_i\}$ is the set of C.M. electron coordinates, $\vec{R}$ is the internuclear separation, and M is the reduced mass of the nuclear system. Since we assume it is appropriate to consider only one channel we write $\Psi(\vec{r}_i, \vec{R})$ as

$$\Psi(\vec{r}_i, \vec{R}) = F(\vec{R}) \, \varphi(\vec{r}_i, \vec{R})$$

where $\varphi(\vec{r}_i, \vec{R})$ is the ground state solution to

$$H_{el} \, \varphi(\vec{r}_i, \vec{R}) = \left[-\frac{\hbar^2}{2m_e} \sum_{i=1}^{N} \nabla_i^2 + V(\vec{r}_i, \vec{R}) \right] \varphi(\vec{r}_i, \vec{R}) = \epsilon(R) \, \varphi(\vec{r}_i, \vec{R})$$

Let us suppose that this electronic Schroedinger equation has been solved exactly at all internuclear separations R and that the total electron binding energies $\epsilon(R)$ have been obtained. If equation III-1 is multiplied by φ^* and integrated over the electron coordinates we obtain

$$\epsilon(R)\,F(\vec{R}) - \left\langle \varphi \left| \frac{\hbar^2}{2M} \nabla_R^2 \right| F(\vec{R})\,\varphi \right\rangle + \frac{Z_a Z_b}{R}\,e^2\,F(\vec{R}) = E\,F(\vec{R})$$

The second term of the last equation may be expanded

$$\left\langle \varphi \left| \frac{\hbar^2}{2M} \nabla_R^2 \right| F(\vec{R})\,\varphi \right\rangle = \frac{\hbar^2}{2M} \nabla_R^2 F(\vec{R}) + \frac{\hbar^2}{M} \nabla_R \cdot F(\vec{R}) \left\langle \varphi | \nabla_R | \varphi \right\rangle$$

$$+ \frac{\hbar^2}{2M} F(\vec{R}) \left\langle \varphi | \nabla_R^2 | \varphi \right\rangle$$

So that

$$\left(-\frac{\hbar^2}{2M} \nabla_R^2 + \frac{Z_a Z_b}{R}\,e^2 + \epsilon(R) - E \right) F(\vec{R}) = \frac{\hbar^2}{2M} \left(\langle \nabla_R^2 \rangle + 2\langle \nabla_R \rangle \cdot \nabla_R \right) F(\vec{R})$$

We now assume that the nuclear velocity is negligibly small and make the Born-Oppenheimer approximation by setting the right hand side of the above equation to zero, and obtain

(III-2)

$$\left(-\frac{\hbar^2}{2M} \nabla_R^2 + \frac{Z_a Z_b}{R}\,e^2 + \epsilon(R) - \epsilon(\infty) \right) F(\vec{R}) = \left(E - \epsilon(\infty) \right) F(\vec{R})$$

This equation is the nuclear Schroedinger equation from which

we identify the intermolecular potential (adjusted to yield

$V(R)=0$ as $R \rightarrow \infty$), $V(R)$ as

(III-3) $\qquad V(R) = \epsilon(R) + \dfrac{Z_a Z_b}{R} e^2 - \epsilon(\infty)$

Please note that since the electron binding energy only depends

upon $|\vec{R}| = R$ for a diatomic system, therefore the potential is

only a function of the magnitude of the internuclear separation.

For many systems, including those discussed herein, $\epsilon(R)$

leads to some nuclear attraction as is seen in figure 6.
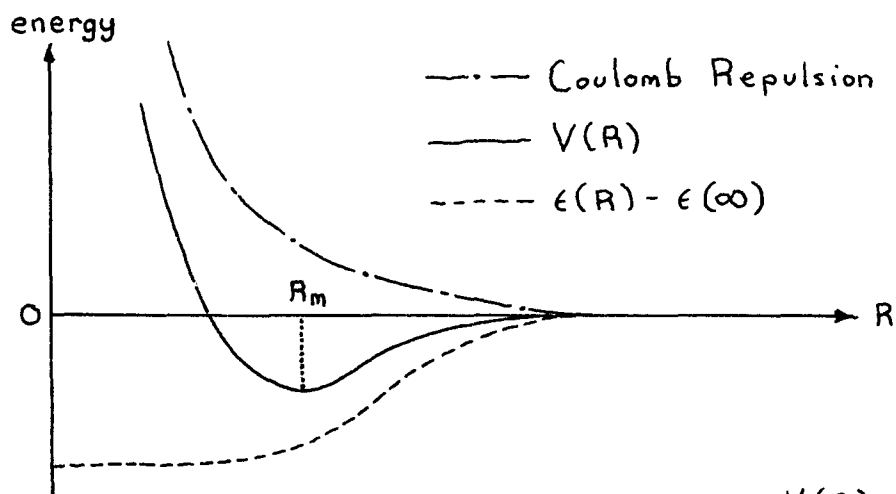
Figure 6: the origin of the attractive well in $V(R)$.

Having defined $V(R)$ we shall now solve equation III-2

by using the partial wave method.[13] To do this we write $F(\vec{R})$

asymptotically as

(III-4) $\qquad F(\vec{R}) = e^{ikz} + \dfrac{e^{ikR}}{R} f(\theta)$

which represents an incident plane wave e^{ikz} and a spherical scattered wave $f(\theta)e^{ikR}/R$ radially outgoing from the center of force (i.e. nuclear center of mass). Using the expression for the current density

$$\vec{j} = \frac{\hbar}{2M}\left(\Psi^* \nabla \Psi - \Psi \nabla \Psi^*\right)$$

for incident and scattered fluxes the differential cross section, $\sigma(\theta)$, may be identified from its definition as:

$$(III-5) \qquad \sigma(\theta) = |f(\theta)|^2$$

To find $f(\theta)$ we expand $F(\vec{R})$

$$F(\vec{R}) = \sum_{\ell=0}^{\infty} A_\ell \frac{\mathcal{F}_\ell(R)}{kR} P_\ell(\cos\theta)$$

where $\mathcal{F}_\ell(R)$ satisfies the radial part of equation III-2 that is:

$$(III-6) \qquad \frac{d^2 \mathcal{F}_\ell(R)}{dR^2} + \left(k^2 - \frac{2M}{\hbar^2}V(R) - \frac{\ell(\ell+1)}{R^2}\right)\mathcal{F}_\ell(R) = 0$$

Since $V(R) \to 0$ as $R \to \infty$ we choose the asymptotic form of $\mathcal{F}_\ell(R)$ as

$$(III-7) \qquad \mathcal{F}_\ell(R) \xrightarrow[R \to \infty]{} \sin\left(kR - \tfrac{1}{2}\ell\pi + \eta_\ell\right)$$

Before proceding further let us make a few remarks about η_ℓ . If $V(R)$ were identically zero the solution to equation III-6 would have:

$$\eta_\ell(R) \propto J_{\ell+\frac{1}{2}}(kR)$$

which goes asymptotically as:

$$\eta_\ell(R) \xrightarrow[R \to \infty]{} \sin\left(kR - \tfrac{1}{2}\ell\pi\right)$$

So that η_ℓ is really the phase shift between the scattered partial wave with $V(R)$ present and with $V(R)=0$. In this sense η_ℓ is a measure of the strength of $V(R)$. Further η_ℓ will be positive for attractive potentials and negative for repulsive ones.[16]

For ℓ very large in equation III-6 the angular momentum term will dominate $V(R)$ and $|\eta_\ell|$ will be small.

Rather than repeat a well-known derivation we simply give the result that $f(\theta)$ may be expressed as an infinite sum over terms involving η_ℓ .

$$(III-8) \qquad f(\theta) = \frac{1}{2ik} \sum_{\ell=0}^{\infty} (2\ell+1)\left(e^{2i\eta_\ell}-1\right) P_\ell(\cos\theta)$$

Equation III-8 is called the Rayleigh-Faxen-Holtzmark (RFH) sum.[13]

We can now relate the potential of equation III-3 to the differential cross section in equation III-5 via equations III-6, III-7, III-8. Although it is possible to proceed in exactly this fashion we will greatly simplify matters by using an approximation for the phase shift which relates η_ℓ directly to $V(R)$. This approximation,[14] called JWKBL, is basically due to the work of Jeffreys. In order to discuss this technique let us consider the one dimensional Schroedinger equation

$$\frac{d^2\Psi}{dx^2} + \frac{p^2}{\hbar^2}\Psi = 0 \quad \text{with} \quad p = \sqrt{2M(E-V(x))}$$

and let

$$\Psi(x) = \varphi(x)\, e^{\pm i\hbar^{-1}\int p(x)\,dx}$$

Upon substituting this expression into the one dimensional wave equation we find:

$$\frac{\hbar}{ip}\frac{d^2\varphi}{dx^2} \pm \left(2\frac{d\varphi}{dx} + \frac{1}{p}\frac{dp}{dx}\varphi\right) = 0$$

If $\dfrac{\hbar}{p}$ is small we neglect the first term above and solve

$$\frac{2}{\varphi}\frac{d\varphi}{dx} + \frac{1}{p}\frac{dp}{dx} = 0 = \frac{d}{dx}\ln\varphi^2 p$$

and

$$\varphi = k \, p^{-1/2}$$

to see precisely what this approximation means we resubstitute the solution

(III-9) $$\psi = k \, p^{-1/2} \, e^{\pm i \hbar^{-1} \int p \, dx}$$

back into the original equation with the result:

$$\frac{d^2 \psi}{dx^2} + \left[\frac{p^2}{\hbar^2} - \frac{3}{4} \left(\frac{p'}{p} \right)^2 + \frac{p''}{2p} \right] \psi = 0$$

giving the exact condition for the approximation

(III-10) $$\left| \frac{\hbar \, p'}{p^2} \right| \sqrt{\frac{3}{4} - \frac{1}{2} \left(\frac{p p''}{p'^2} \right)} \; \ll \; 1$$

This condition will be fulfilled if p^2 is large with respect to $\hbar p'$; that is, if λ is small with respect to changes of the potential. So for smooth slowly changing potentials and reasonably short wave lengths for the free particle, equation III- 9 should be a good approximation.
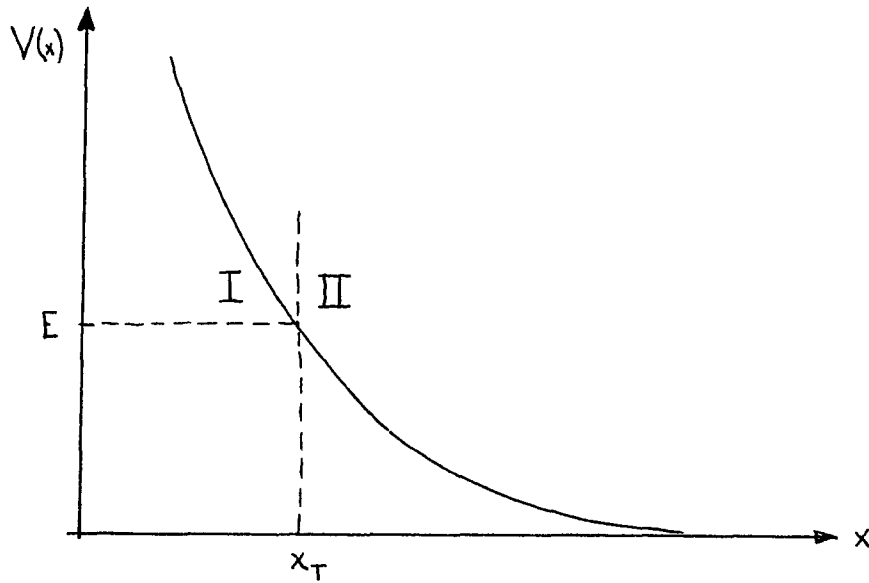
Figure 7: one dimensional V(x) showing classical and non-classical regions.

To the right of the classical turning point, x_T , in figure 7 $E > V$ and p is real so that the solution to equation III- 9 is oscillatory; while to the left of $x_T, E < V$, p is imaginary and ψ is exponentially damped. This is in good agreement with the classical result which forbids the particle to exist in region I. What we have said thus far is not valid for $x \sim x_T$, since $p \sim 0$ and equation III-10 is not in general true. Jeffreys has provided the appropriate connection formula in the region of the turning point.[14]

Assume $V(x)$ is linear in a small region about x_T i.e. let:

$$V(x) = E - A(x - x_T)$$

so,

$$\frac{d^2 \psi}{dx^2} + \frac{2MA}{\hbar^2} (x - x_T) \psi = 0$$

Define:

$$z = - \left(\frac{2MA}{\hbar^2} \right)^{1/3} (x - x_T)$$

So the Schroedinger equation becomes

$$\frac{d^2 \psi}{dz^2} - z\psi = 0$$

The solution to this equation is the Airy function,

$$Ai(z) \equiv \frac{1}{\pi} \int_0^\infty \cos\left(\frac{s^3}{3} + sz \right) dS$$

which has the asymptotic forms

$$Ai(z) \sim \frac{1}{2\sqrt{\pi}\, z^{1/4}} \cdot e^{-\frac{2}{3}(-z)^{3/2}} \qquad \text{for} \quad z > 0$$

and

$$Ai(z) \sim \frac{1}{\pi(-z)^{1/4}} \cdot \sin\left(\frac{2}{3}(-z)^{3/2} + \frac{\pi}{4} \right) \quad \text{for} \quad z < 0$$

To identify the connection with equation III-9 we resub-
stitute as follows:

$$\frac{2}{3}(-z)^{3/2} = \frac{2}{3}\sqrt{\frac{2MA}{\hbar^2}} (x-x_T)^{3/2} = \frac{1}{\hbar} \int_{x_T}^x \sqrt{2MA(x-x_T)}\, dx$$

$$= \frac{1}{\hbar} \int_{x_T}^x \sqrt{2M(E-V)}\, dx = \frac{1}{\hbar} \int_{x_T}^x p\, dx$$

Which gives ψ for regions I and II in agreement with equation

III-9 as:

$$\psi_I = |p|^{-1/2}\, e^{\hbar^{-1} \int_{x_T}^x |p|\, dx}$$

and

(III-11) $\quad \Psi_{II} = 2 \, p^{-1/2} \sin \left(\hbar^{-1} \int_{x_T}^{x} p \, dx + \frac{\pi}{4} \right)$

We could now hope to use equation III-11 to evaluate η_ℓ
first having let

$$p = \sqrt{2M(E - V_{eff})}$$

where the effective potential is

$$V_{eff} \equiv V(R) + \frac{\ell(\ell+1)\hbar^2}{2MR^2}$$

It would, however, be incorrect to do so since our previous
solution was exponentially damped in region I as $x \longrightarrow -\infty$
We must solve the problem for Ψ_I to go to zero as $R \longrightarrow 0$

The equation we must solve is

(III-6) $\quad \dfrac{d^2 \, {}^{o}\!\mathcal{F}_\ell(R)}{dR^2} + \dfrac{2M}{\hbar^2} (E - V_{eff}) \, {}^{o}\!\mathcal{F}_\ell(R) = 0$

If we define

$$\rho = \ln R \quad \text{and} \quad \xi_\ell \, R^{-1/2} = {}^{o}\!\mathcal{F}_\ell(R)$$

Equation III- 6 becomes, after some algebra:

$$\frac{d^2 \xi_\ell}{d\rho^2} + e^{2\rho} \left[\frac{2M}{\hbar^2} (E - V) - \frac{(\ell + \frac{1}{2})^2}{e^{2\rho}} \right] \xi_\ell = 0$$

For this equation we have the same boundary conditions in region I as before — so we may simply use our former result for region II.

$$\xi_{\ell\,II} = \frac{2 \sin\left(\frac{\pi}{4} + \int_{\rho_T}^{\rho} \sqrt{e^{2\rho}\,2M(E-V) - (\ell+\frac{1}{2})^2\,\hbar^2}\,d\rho\right)}{\sqrt[4]{e^{2\rho}\,2M(E-V) - (\ell+\frac{1}{2})^2\,\hbar^2}}$$

Therefore:

$$\sigma\mathcal{F}_\ell(R) = 2\,Q^{-1/4} \sin\left(\frac{\pi}{4} + \int_{R_T}^{R} Q^{1/2}\,dR\right)$$

with

$$Q = \frac{2M}{\hbar^2}(E-V) - \frac{(\ell+\frac{1}{2})^2}{R^2}$$

or

$$\sigma\mathcal{F}_\ell(R) = 2\,Q^{-1/4} \sin\left(\frac{\pi}{4} + \int_{R_T}^{R}(Q^{1/2}-k)\,dR + kR - kR_T\right)$$

As R becomes large,

$$\sigma\mathcal{F}_\ell(R) \sim \sin\left(\frac{\pi}{4} + \int_{R_T}^{\infty}(Q^{1/2}-k)\,dR + kR - kR_T\right)$$

Comparing this result with the required asymptotic form,

equation III- 7, we may identify η_ℓ as:

$$(\text{III-12}) \quad \eta_\ell = \frac{\pi}{4} + \frac{\ell\pi}{2} - k R_T + \int_{R_T}^{\infty} \left(\sqrt{\frac{2M}{\hbar^2}(E-V) - \frac{(\ell+\frac{1}{2})^2}{R^2}} - k \right) dR$$

The agreement between the JWKBL phase shift which we have just calculated, equation III-12 and η_ℓ obtained from the numerical solution to equation III- 6 has been found to be[17] extremely good. A typical phase shift function corresponding to figure 6 is shown in figure 8 .
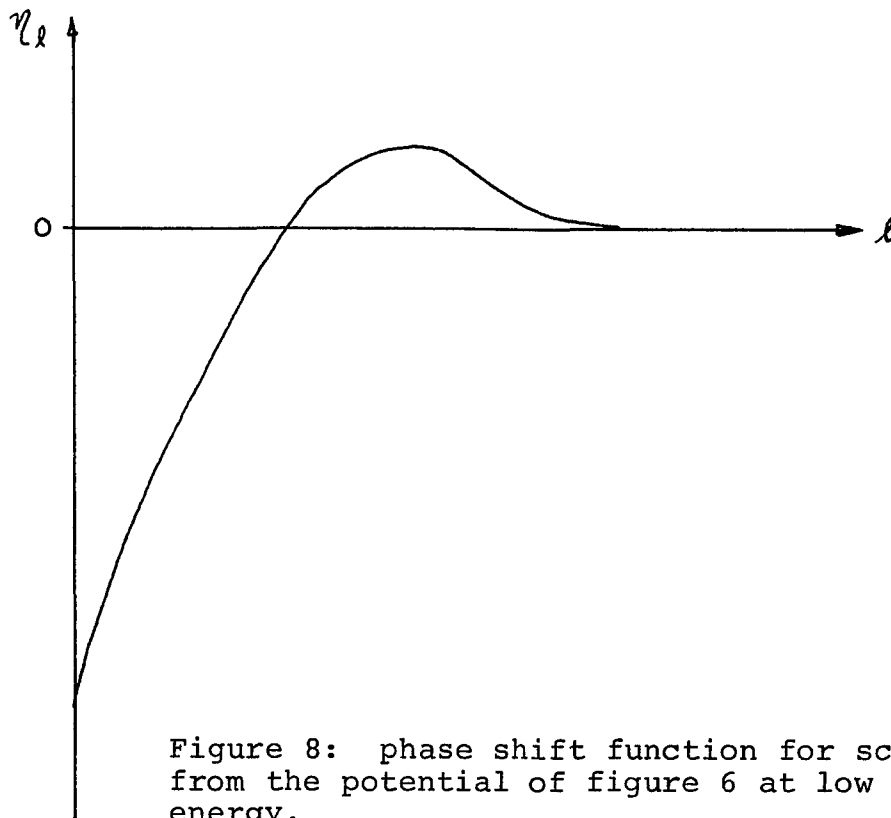
Figure 8: phase shift function for scattering from the potential of figure 6 at low collision energy.

We shall now digress briefly to discuss how the results thus far obtained are relevant to the low energy scattering experiments in Section IIID. In an earlier attempt to recover the intermolecular potential[18] we assumed an analytic form for $V(R)$

$$(\text{III-13}) \quad V(R) = \frac{C_1 e^{C_2 R}}{R} - \frac{C_3}{R^6} - \frac{C_4}{R^4}$$

We then calculated the JWKBL phase shifts corresponding to this potential and used the partial wave sum to find the cross section. The parameters C_1, C_2 and C_3 were varied in the calculation until the predicted cross section was in "satisfactory" agreement with the experimental data. The resulting values of C_1, C_2 and C_3 as well as C_4 (which is not a free parameter but is fixed by the dipole polarizability of the target atom) determine the intermolecular potential through the assumed form of equation III-13. This procedure, although numerically correct, has two major diadvantages. First, no insight is given into the scattering features; and second, for the systems of present interest, the upper limit on the sum in equation III-8 must be quite large, about 800, for proper convergence of the phase shifts

While the semiclassical method [19] affords insight into the nature of the scattering the Remler-Regge[3] and Vollmer[4] methods allow a much more efficient recovery of $V(R)$ from the experi-

mental cross section. Therefore, we shall proceed to develop these topics.

IIIB.   The Classical and Semiclassical Methods

Consider a purely repulsive spherically symmetric field of force with a beam of non-interacting classical particles incident upon it as shown in figure 9.
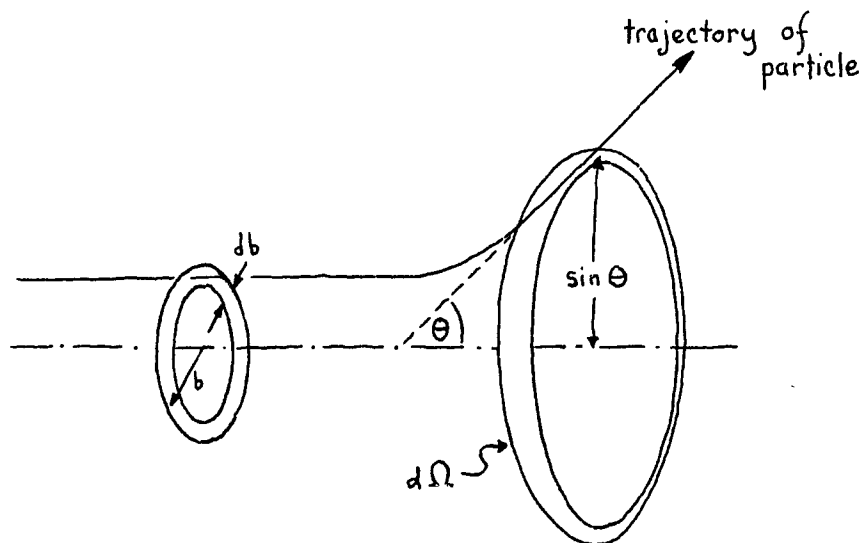
Figure 9:   scattering by a repulsive center of force.

From the definition of differential cross section given in Section IIIA we have:

Number scattered into $d\Omega = \sigma(\theta)\, I\, d\Omega$

where I is the incident beam intensity. If all of the incident particles having impact parameter between b and $b+db$ are scattered into the $d\Omega$ shown in figure 9 then

$$I\,(2\pi b\, db) = -\sigma(\theta)\, I\, 2\pi \sin\theta\, d\theta$$

where the minus sign indicates that increasing b decreases θ. Therefore the classical cross section is given as

$$\sigma(\theta) = -\frac{b\,db}{\sin\theta\,d\theta}$$

We can write b in terms of the angular momentum L:

$$L = M_v b = \sqrt{2ME}\,b$$

So that

(III-14) $\quad\sigma(\theta) = \dfrac{L}{2ME\sin\theta}\left(-\dfrac{d\theta}{dL}\right)$

If one can find the relation between θ and L then equation III-14 may be used to find $\sigma(\theta)$.

This connection is provided by the equation of orbit for a classical particle whose angular momentum in conserved.[20]

(III-15) $\quad\varphi(R) = \varphi_T + \displaystyle\int_{R_T}^{R} \frac{dR}{R^2\left[\dfrac{2ME}{L^2} - \dfrac{2MV(R)}{L^2} - \dfrac{1}{R^2}\right]^{1/2}}$
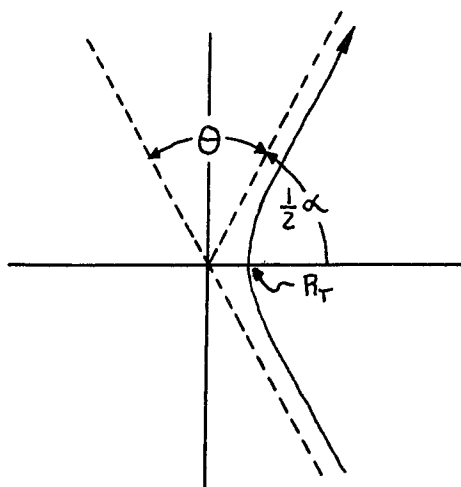
Figure 10: trajectory of a repulsively scattered particle.

From figure 18 it is seen that the C.M. scattering angle, Θ , is:

$$\Theta = \pi - \alpha$$

And from equation III-15

$$\frac{1}{2}\alpha = 0 + \frac{L}{\sqrt{2M}} \int_{R_T}^{\infty} \frac{dR}{R^2\sqrt{E-V_{eff}}}$$

where

$$V_{eff} = V(R) + \frac{L^2}{2MR^2}$$

Our discussion to this point has been for simple repulsive trajectories only. However, we may take the same result over for attractive scattering and define the classical deflection function, Θ , just as before, i.e.

$$\Theta(L) \equiv \pi - \alpha$$

We note that for repulsive paths $\Theta = \Theta$ and for attractive trajectories $\alpha > \pi$ and $\Theta < 0$. In fact, for attractive scattering $\Theta = -\Theta$. Using our previous result

$$(\text{III-16}) \quad \Theta(L) = \pi - \frac{2L}{\sqrt{2M}} \int_{R_T}^{\infty} \frac{dR}{R^2\sqrt{E-V_{eff}}}$$

For purely repulsive potentials there is very little effect on the path of a particle having large L (i.e. large b) so Θ (large L) is small and positive; while the particle which is directly incident on the center of force, $L = 0$, is reflected back along this same line so $\Theta(0) = \pi$. Figure 11 shows a typical repulsive $\Theta(L)$.
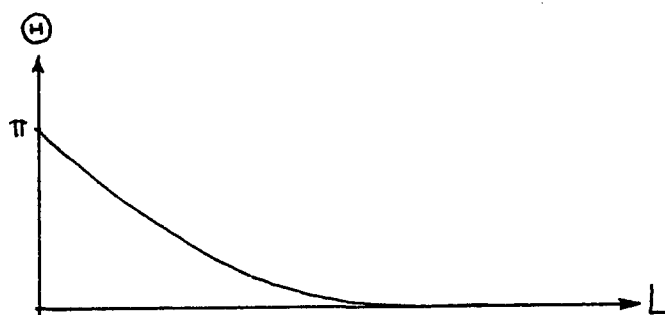
Figure 11: $\Theta(L)$ for repulsive potentials.

The type of intermolecular potentials which we will consider in this section are not purely repulsive but have an attractive well as shown by the solid line of figure 6 . Figure 12 will aid in the construction of $\Theta(L)$ for this case.
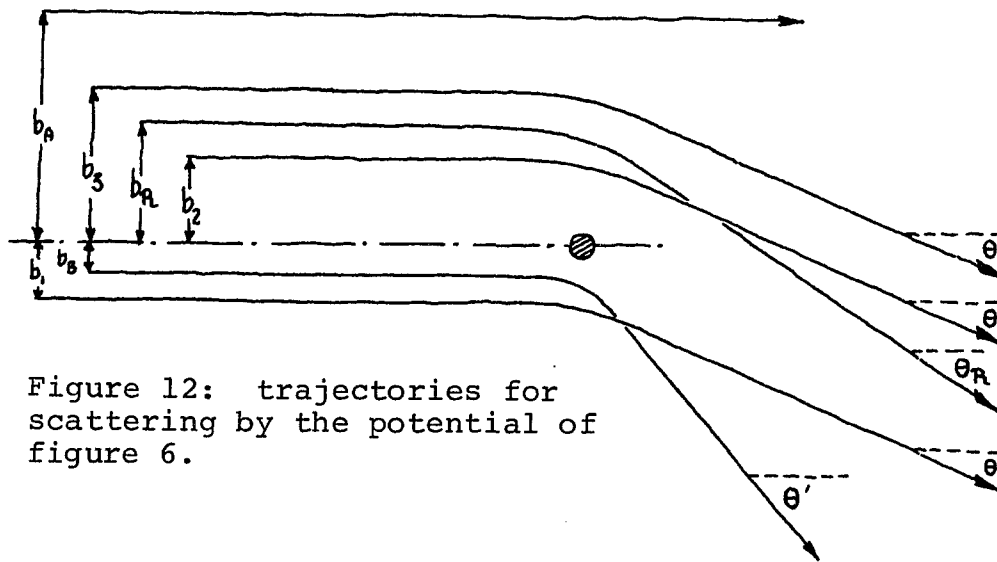
Figure 12:   trajectories for scattering by the potential of figure 6.

Here the particle having $b = b_A$ shows no deflection and

the one with $b = b_3$ shows some attraction. At $b = b_R$ a maximum

attractive deflection called the rainbow angle, Θ_R , is

reached. For $b < b_R$ the trajectory becomes increasingly

repulsive as is shown for $b = b_2, b_1, b_B$. The limit of π

for $\textcircled{H}(0)$ is obtained as before. Note, in figure 12

the attractive trajectories have been placed above the center-

line so as to point out the fact that particles having $b = b_1, b_2, b_3$

appear at the same lab angle $\ominus$. The deflection function

corresponding to figure 12 is shown in figure 13.
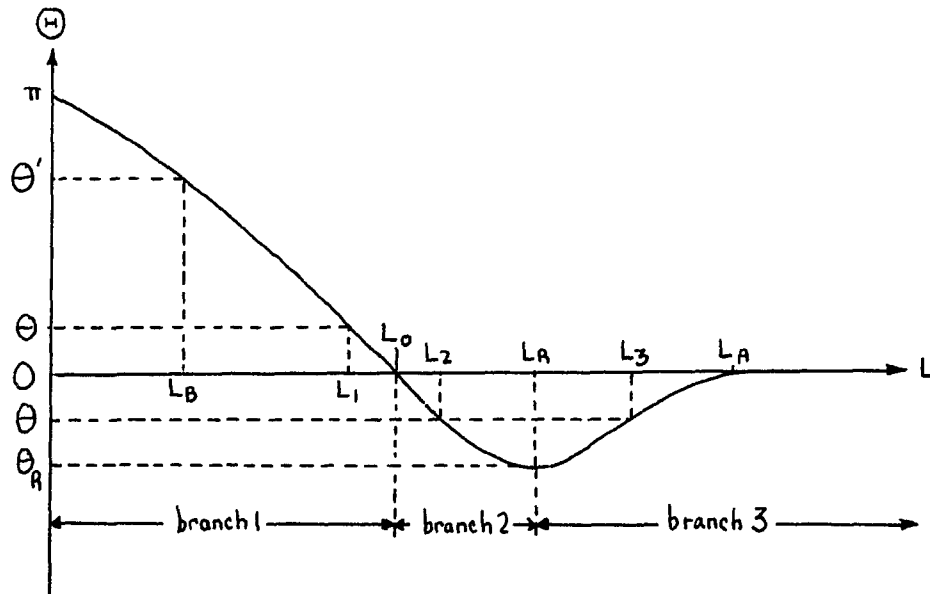
Figure 13: $\textcircled{H}(L)$ corresponding to $V(R)$ in figure 6.

By analogy with equation III-14 the classical cross section is

given for $\ominus < \Theta_R$ as the sum of the classical cross sections

for the three branches of the deflection function[21] shown in

figure 13.

$$\sigma(\theta)_{\theta < \Theta_R} = \sum_{\substack{branches \\ i=1}}^{3} \frac{L_i}{2ME \sin\theta \left|\frac{d\Theta}{dL}\right|_{L=L_i}}$$

While only branch 1 contributes for $\Theta > \Theta_R$

$$\sigma(\theta)_{\theta > \Theta_R} = \frac{L_1}{2ME \sin\theta \left|\frac{d\Theta}{dL}\right|_{L=L_1}}$$

For

$$\Theta = 0 \quad , \quad \sin\Theta = 0 \quad , \quad L_3 \longrightarrow \infty$$

and $\left|\frac{d\Theta}{dL}\right|_{L=L_3} = 0$; and for all these reasons $\sigma(0) = \infty$. For $\Theta = \Theta_R$, $\left|\frac{d\Theta}{dL}\right|_{L=L_3, L_2} = 0$ and $\sigma(\Theta_R) = \infty$. Therefore the classical prediction for $\sigma(\theta)$ appears as shown in figure 14.
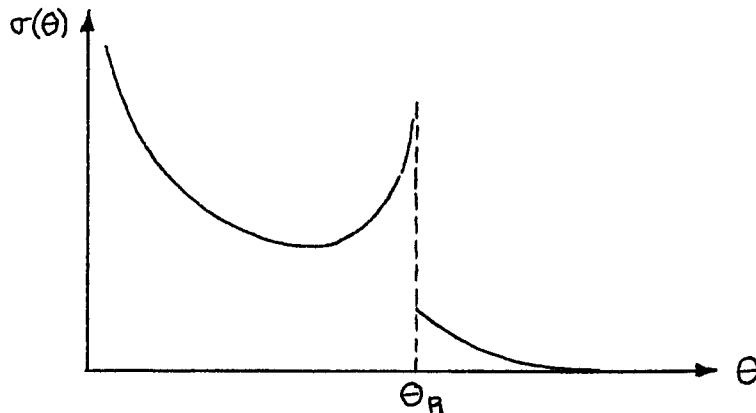
Figure 14: prediction of $\Theta(L)$ in figure 13 for the differential cross section.

This certainly does not look like the experiment in figure 5a and, thus, the classical treatment needs considerable refinement. Such refinement is provided by the semiclassical method

which takes into account the phase relations of the scattered partial waves.

The starting point for the semiclassical method is the RFH partial wave sum

$$(\text{III-8}) \quad f(\theta) = \frac{1}{2ik} \sum_{\ell=0}^{\infty} (2\ell+1) \left(e^{2i\eta_\ell} - 1 \right) P_\ell (\cos \theta)$$

The orthogonality[22] of the Legendre functions shows

$$\sum_\ell (2\ell+1) \, P_\ell (\cos \theta) = 2\delta (1 - \cos\theta)$$
$$\text{where } \delta \text{ is the Dirac delta function}$$

So if we are not interested in $\theta = 0$ we may drop the -1 in equation III-8. Further, we use Laplace's approximation for large ℓ (i.e. for $\ell \geq 1/\sin\theta$) :

$$P_\ell (\cos \theta) \sim \sqrt{\frac{2}{\pi \ell \sin\theta}} \, \sin \left((\ell + \tfrac{1}{2}) \theta + \pi/4 \right),$$

thus

$$f(\theta) = \frac{1}{k} \sum_\ell \sqrt{\frac{\ell}{2\pi \sin\theta}} \left(e^{i B_2} - e^{i B_1} \right)$$

with

$$B_2 = 2\eta_\ell - (\ell + \tfrac{1}{2})\theta - \pi/4$$

and

$$B_1 = 2\eta_\ell + (\ell + \tfrac{1}{2})\theta + \pi/4$$

Replacing the sum $\sum_{\ell=0}^{\infty}$ by $\int_0^{\infty} d\ell$ and also letting $\ell + \tfrac{1}{2} \to \ell$ (again good

for large ℓ) we have

$$(\text{III-17}) \quad f(\theta) = -\frac{1}{k\sqrt{2\pi\sin\theta}} \int_0^\infty d\ell \sqrt{\ell} \left(e^{i B_1(\ell)} - e^{i B_2(\ell)} \right)$$

where now,

$$B_1(\ell) = 2\eta_\ell + \ell\theta + \frac{\pi}{4}$$

$$B_2(\ell) = 2\eta_\ell - \ell\theta - \frac{\pi}{4}$$

Since the arguments B_1, B_2 in the above integral are, in general, rapidly changing functions of ℓ the exponentials are, therefore, very high frequency terms. The stationary phase approximation states that the only contributions to the integral of equation III-17 come from those values of ℓ where either phase B_1 or B_2 is stationary; and gives:

$$\frac{dB_1}{d\ell} = 0 = 2\frac{d\eta_\ell}{d\ell} + \theta$$

$$\frac{d\eta_\ell}{d\ell} = -\frac{1}{2}\theta$$

$$\frac{dB_2}{d\ell} = 0 = 2\frac{d\eta_\ell}{d\ell} - \theta$$

$$\frac{d\eta_\ell}{d\ell} = \frac{1}{2}\theta$$

Both of these requirements may be combined in the following fashion:

$$(\text{III-18}) \quad \frac{d\eta_\ell}{d\ell} = \frac{1}{2}\circledR .$$

43

We then identify the term containing (B_1, B_2) in equation III-17 as corresponding to (attractive, repulsive) scattering.

Equation III-18 , called the semiclassical equivalence relation, furnishes the important connection between the quantum mechanical phase shifts and the classical deflection function.

In the full quantum treatment each partial wave was able to contribute to the scattering amplitude at every center of mass angle. The equivalence relation greatly restricts the situation and constrains each partial wave to contribute at essentially one scattering angle corresponding to a point on the classical deflection function. However, if $\Theta(L)$ is multiply branched (as shown in figure 13), more than one partial wave can contribute at the same angle. To calculate the differential cross section let us expand the attractive scattering phase, $B_1(\ell)$, about a stationary point $\ell = L$

$$B_1(\ell) = B_1(L) + B_1'(L)(\ell-L) + \frac{1}{2} B_1''(L)(\ell-L)^2 + \text{higher order terms}$$

By the requirement of stationary phase $B_1' = 0$. Neglecting higher order terms we may write

$$f(\theta)_{\text{attractive}} = -\frac{1}{k} \left[\frac{L}{2\pi \sin\theta} \right]^{1/2} e^{iB_1(L)} \cdot J$$

with

$$J = \int\limits_{-L}^{\infty} d(\ell \cdot L)\, e^{i\left(\eta_L'' (\ell - L)^2\right)} \quad .$$

For $\ell < -L$ the above integrand is rapidly oscillating and averages to zero. Consequently we may extend the lower limit to $-\infty$ and evaluate J for $\eta_L'' > 0$ (corresponding to branch 3 of the deflection function shown in figure 13). The result is

$$J = \left(\frac{\pi}{\eta_{L_3}''} \right)^{1/2} e^{-i\,\pi/4}$$

If we let $\eta_L'' < 0$ corresponding to branch 2

$$J = \left(-\frac{\pi}{\eta_{L_2}''} \right)^{1/2} e^{-i\,\pi/4}$$

We could then expand B_2 about its one $\left(\eta_{L_1}'' < 0 \right)$ stationary point and repeat the procedure just completed. The result is that we can associate with each branch, i , of the classical deflection function a partial $f_i(\theta)$ and obtain

$$f_1(\theta) = \sqrt{\sigma_{c_1}}\; e^{i\left(2\eta_{L_1} - L_1\theta - \frac{\pi}{2}\right)}$$

(III-19)
$$f_2(\theta) = \sqrt{\sigma_{c_2}}\; e^{i\left(2\eta_{L_2} + L_2\theta - \pi\right)}$$

$$f_3(\theta) = \sqrt{\sigma_{c_3}}\; e^{i\left(2\eta_{L_3} + L_3\theta + \frac{\pi}{2}\right)}$$

with the classical cross sections σ_{ci} given in accordance with equation III-14.

$$\sigma_{ci} = \frac{L_i}{k^2 \, 2 \, | \eta_{L_i}'' | \, \sin \theta} = \frac{L_i}{k^2 \, \sin \theta \, \left| \frac{d\Theta}{dL} \right|_{L_i}}$$

The semiclassical cross section is then

$$(III-20) \qquad \sigma_{sc} (\theta) = \left| f_1(\theta) + f_2(\theta) + f_3(\theta) \right|^2$$

This result is valid when B_1 has two stationary phase points as shown in figure 15.
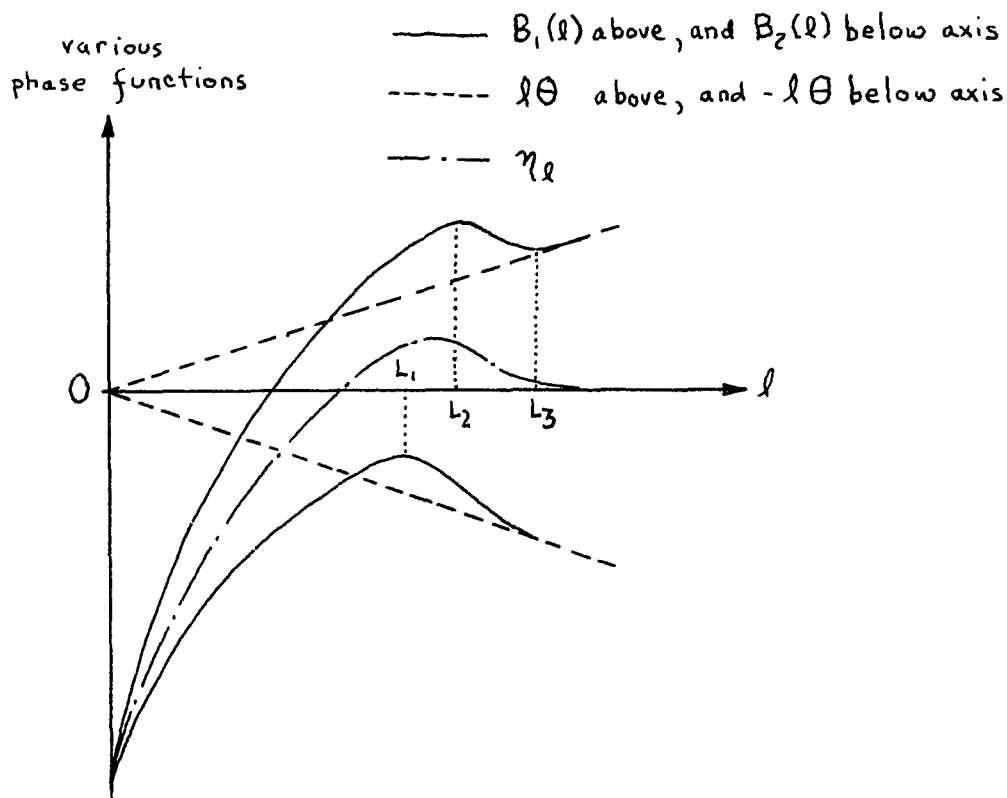
Figure 15: the origin of the stationary phase points corresponding to the three branches of $\Theta(L)$ in figure 13.

When Θ is sufficiently large the slope of $\ell\Theta$ is steep, B_1 has no stationary points (shown in figure 16) and only branch 1 contributes to the scattering.
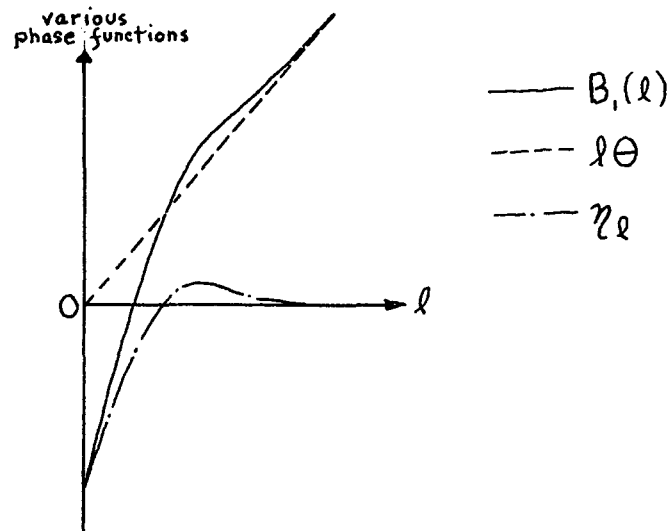
Figure 16: the disappearance of the attractive stationary point for large Θ .

Equation III=20 shows, that in this case, the classical result is valid.

In the angular range about which $\Theta(L)$ possesses a minimum (i.e. the rainbow angle) $\eta''_{L_{2,3}} = O$ and equations III-19 do not apply.

Ford and Wheeler [2] in a famous set of papers kept the third derivative term in the phase B_1 and assumed that the deflection function was parabolic about L_R (the angular momentum quantum number corresponding to Θ_R).

(III-21) $\qquad \Theta = \Theta_R + q \left(L - L_R \right)^2$

Therefore

$$B_1 = 2\eta_{L_R} - \Theta_R(L - L_R) + \frac{1}{3}q(L - L_R)^3 + L\Theta + \frac{\pi}{4} \,,$$

and

$$f_{attractive}(\Theta) = -\frac{1}{k}\left[\frac{L_R}{2\pi\sin\Theta}\right]^{1/2} e^{i\left(2\eta_{L_R} + L_R\Theta + \frac{\pi}{4}\right)} \cdot \mathcal{A} \,,$$

where

$$\mathcal{A} \equiv \int_{-\infty}^{\infty} e^{i\left(\frac{1}{3}q(L-L_R)^3 + (\Theta-\Theta_R)(L-L_R)\right)} d(L - L_R) \,.$$

Letting

$$x = q^{-1/3}(\Theta - \Theta_R)$$

and defining

$$Ai(x) \equiv \frac{1}{2\pi}\int_{-\infty}^{\infty} e^{i\left(xz + \frac{1}{3}z^3\right)} dz$$

We find

$$f_{attractive}(\Theta) = \sqrt{\sigma_R}\, e^{i\eta}$$

with

$$\text{(III-22)} \quad \sigma_R = \frac{1}{k^2}\frac{2\pi L_R}{\sin\Theta} q^{-2/3} Ai^2\left(q^{-1/3}(\Theta - \Theta_R)\right)$$

and

$$\eta = 2\eta_{L_R} + L_R\theta - \frac{3}{4}\pi$$

So that

$$\sigma_{sc}(\theta) = \left| \sqrt{\sigma_{c_1}} \, e^{i\gamma_1} + \sqrt{\sigma_R} \, e^{i\eta} \right|^2$$

where γ_1 is the phase of the repulsively scattered partial wave

From equation III-19

$$\gamma_1 = 2\eta_{L_1} - L_1\theta - \frac{1}{2}\pi$$

and we may write

$$(III-23) \quad \sigma_{sc}(\theta) = \sigma_{c_1} + \sigma_R + 2\sqrt{\sigma_{c_1}\sigma_R} \, \cos(\eta - \gamma_1)$$

In the above equation σ_{c_1} is a monotonically decreasing function of θ and σ_R has the periodicity of:

$$A_i^2\left(q^{-1/3}(\theta - \theta_R)\right)$$

The first two terms in equation III-23 are shown and combined in figure 17. They clearly account for the low frequency structure in the differential cross section around θ_R (see for example the experimental cross section in figure 5a).

low frequency components of $\sigma(\theta)$

The rainbow

approximation

is invalid in

this region

$\cdots - \sigma_{c_i}$

$---- \sigma_R$

$\underline{\quad\quad} \sigma_R + \sigma_{c_i}$

θ

θ_R
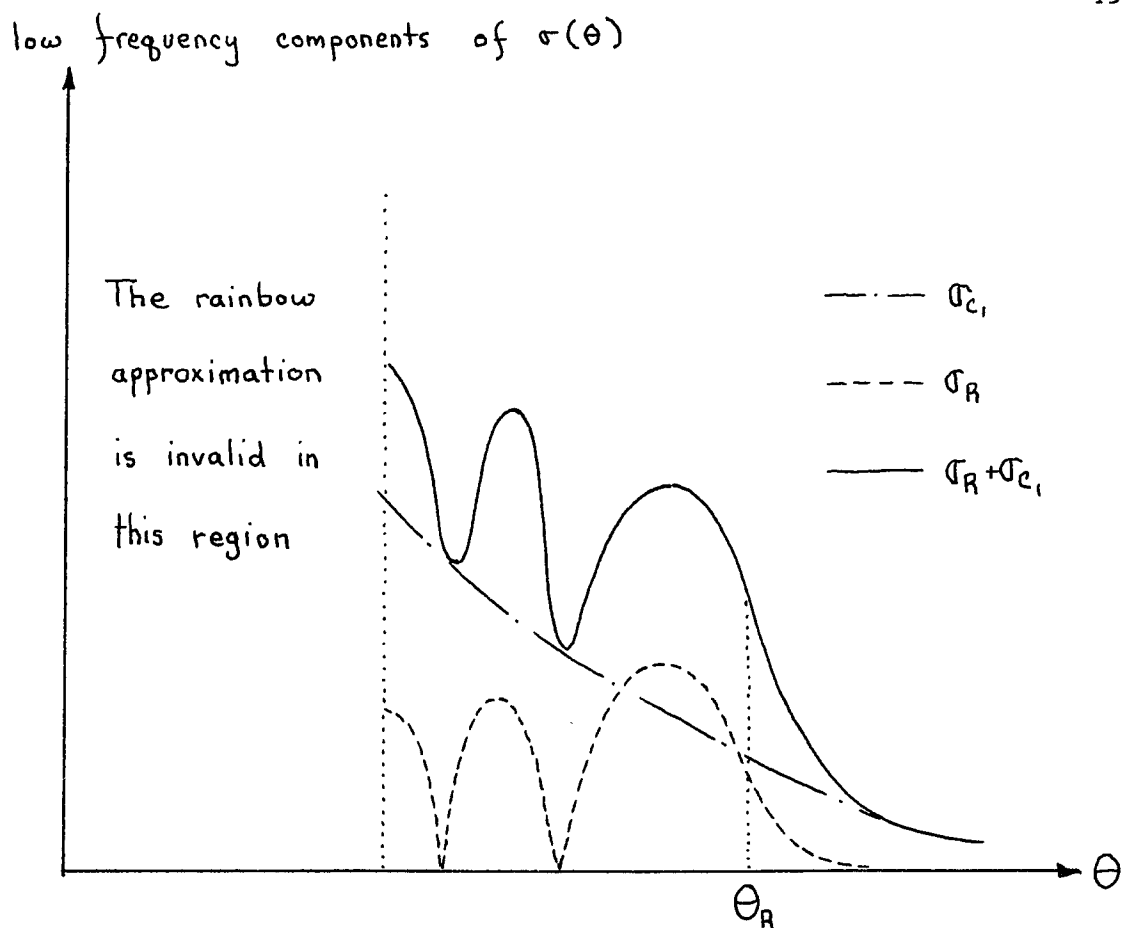
Figure 17: low frequency components of $\sigma(\theta)$ for scattering around θ_R in the semiclassical regime.

The last term of equation III-23 is the source of the high frequency structure seen in well-resolved experimental cross sections. Its phase is

$$\eta - \gamma_i = 2(\eta_{L_R} - \eta_{L_i}) + \theta(L_R + L_i) - \frac{\pi}{4}$$

giving the spacing between adjacent maxima as:

$$(III-24)\, \Delta\theta = \frac{2\pi}{L_R + L_i}$$

The envelope of equation III-23 is seen to be

$$\sigma_{Max} = \left(\sqrt{\sigma_R} + \sqrt{\sigma_{C_1}} \right)^2$$

$$\sigma_{Min} = \left(\sqrt{\sigma_R} - \sqrt{\sigma_{C_1}} \right)^2$$

The semiclassical result for scattering in the vicinity of the rainbow angle is presented in figure 18 (again compare with the experimental data in figure 5a.
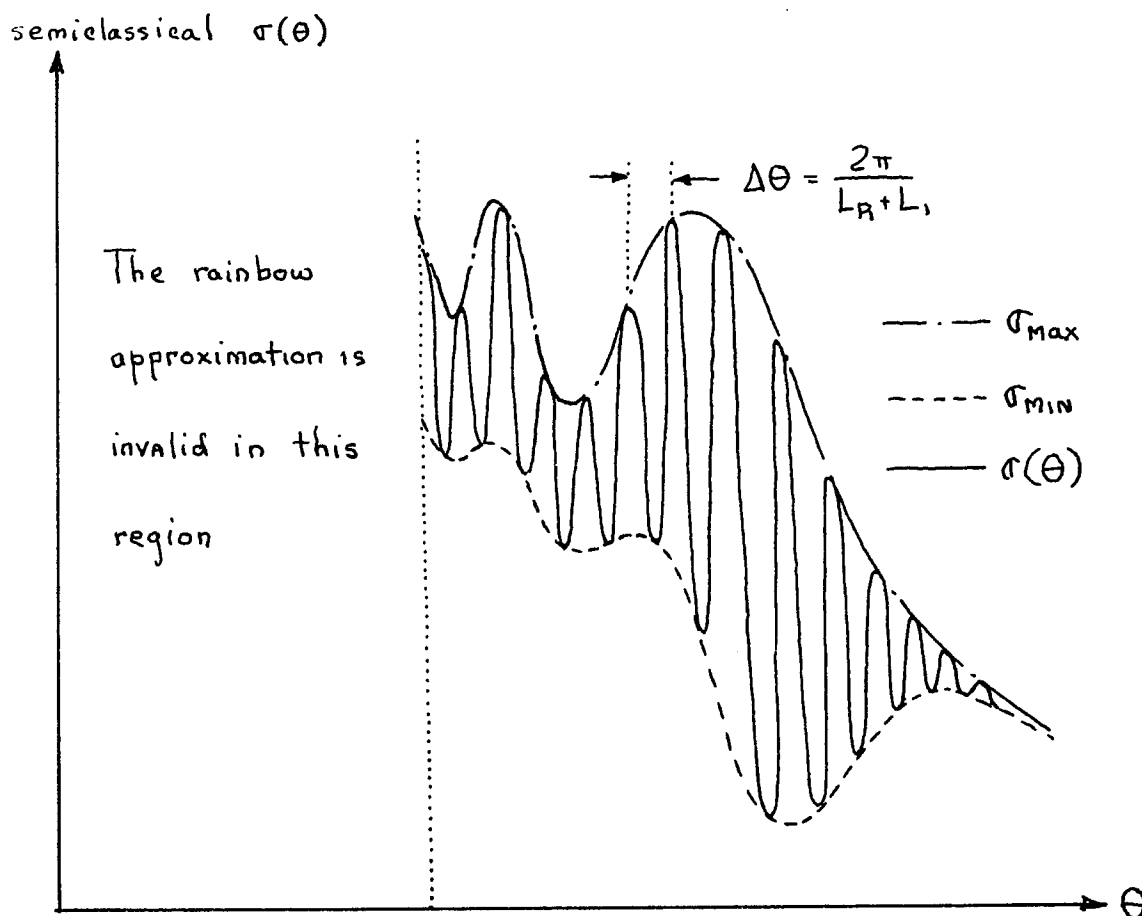
Figure 18: prediction for the high and low frequency components of $\sigma(\theta)$ for scattering around Θ_R in the semiclassical regime.

Let us conclude this semiclassical discussion by examining the small angle behaviour of the cross section. As $\theta \to 0$ the repulsive and innermost attractive branches come together. Thus,

$$L_1 \to L_2 \to L_0$$

$$\sigma_{c_1} \to \sigma_{c_2} \to \sigma_0 \equiv \frac{L_0}{k^2 \sin\theta \, |\eta_{L_0}''| 2}$$

and

$$\eta_{L_1} \to \eta_{L_2} \to \eta_{L_0}$$

Therefore equation III-19 leads to:

$$f_1(\theta) + f_2(\theta) = \sqrt{\sigma_0} \; e^{i\left(2\eta_{L_0} - \frac{3}{4}\pi\right)} \left[e^{i\left(L_0\theta - \frac{\pi}{4}\right)} + e^{-i\left(L_0\theta - \frac{\pi}{4}\right)} \right]$$

$$= 2\sqrt{\sigma_0} \; e^{i\gamma_0} \cos\left(L_0\theta - \frac{\pi}{4}\right)$$

with

$$\gamma_0 \equiv 2\eta_{L_0} - \frac{3}{4}\pi$$

Adding $f_3(\theta)$ we find:

$$f(\theta) = \sqrt{\sigma_{c_3}} \; e^{i\gamma_3} \left[1 + 2\sqrt{\frac{\sigma_0}{\sigma_{c_3}}} \; e^{i(\gamma_0 - \gamma_3)} \cos\left(L_0\theta - \frac{\pi}{4}\right) \right]$$

where

$$\gamma_3 \equiv 2\eta_{L_3} + L_3\theta - \frac{\pi}{2}$$

This gives the expression for the cross section

(III-25) $\sigma_{sc}(\theta) = \sigma_{c_3}\left[1 + y^2(\theta) + 2y(\theta)\cos\gamma\right]$

where

$$y(\theta) \equiv 2\sqrt{\frac{\sigma_0}{\sigma_{c_3}}}\cos\left(L_0\theta - \frac{\pi}{4}\right)$$

and

$$\gamma = 2\left(\eta_{L_0} - \eta_{L_3}\right) - L_3\theta - \frac{\pi}{4}$$

The last term in equation III-25 contains two frequency components (the sum and difference of the frequencies of the multiplicative terms). The lower frequency term, having period

(III-26) $\quad \Delta\theta = \dfrac{2\pi}{L_3 - L_0}$

is dominant in the low angle range, while the higher frequency term has period

(III-27) $\quad \Delta\theta = \dfrac{2\pi}{L_3 + L_0}$

The y^2 term of equation III-25 has

$$\Delta\theta = \frac{\pi}{L_0}$$

which is quite comparable to the period of the high frequency oscillations around θ_R given in equation III-24.

As the scattering angle is decreased the y^2 term is more quickly damped than the $y\cos\gamma$ term since the amplitude

of $\mathcal{Y}$ (namely $2\sqrt{\frac{\sigma_0}{\sigma_{\ell_3}}}$) is becoming considerably less than one.

Although recent developments[23] have allowed a uniform approximation (covering all angular ranges) to be made in the semiclassical regime we have not discussed this technique. Its omission is due to the fact that we rely on the semiclassical method only for insight into the scattering features. For quantitative calculation of the cross section we do not have to make the semiclassical approximations — rather we will use the Remler-Regge method[3] which is presented next.

IIIC. The Remler-Regge Method and Inversion Procedure

In our previous discussions concerning the partial wave method we have pointed out two disadvantages associated with the RFH sum: (1) the length of the numerical computation for the systems of present interest, and (2) the lack of insight into the observed scattering features afforded by this scheme. The semiclassical method just presented dealt admirably with the latter objection at the expense, however, of further approximations to the formalism and consequent loss of accuracy.

Concurrently with the historical development of the semiclassical method Regge[24] was investigating the properties of the S-matrix considered as a function of a complex angular momentum variable. One of the results of this investigation was a type of singularity in the S-matrix elements which is presently called a Regge pole. Using the Watson-Sommerfeld[25] method the infinite partial wave sum may, in many cases, be replaced by a sum over a finite number of such poles. Remler[3] has applied this result to low energy atomic scattering problems; and we find, in the 6 eV H^+ + Ar problem, that the partial wave sum over 750 values of ℓ may be replaced by a sum over 13 poles in the complex ℓ plane. Moreover, Remler[3] has explicitly connected the singularities in the diagonal S-matrix elements with the deflection function thus providing the intuitive connection between the pole parameters (number and location) and the scattering features.

We shall now discuss the Remler-Regge method.[3] We begin

by defining

$$S_p(\lambda) = e^{2i\eta_{\lambda - 1/2}} \quad \text{with} \quad \lambda = \ell + 1/2$$

The RFH sum, equation III-8 may be rewritten

$$i k f_p(\theta) = \sum_\lambda \lambda \, P_{\lambda - 1/2}(\cos\theta)(S_p - 1)$$

We now apply the Watson-Sommerfeld method[25] to the above sum. That is, the summand above is multiplied by a function which contains first order poles for integer ℓ and then integrated over a clockwise contour, C_1, containing the real axis of the $[\lambda]$ plane and closing at $\ell = +\infty$, we obtain:

$$(\text{III-28}) \qquad i k f_p(\theta) = \oint_{C_1} \frac{\pi}{\cos\pi\lambda} \lambda \, P_{\lambda - 1/2}(-\cos\theta)(S_p - 1) \, d\lambda$$

If S_p contains a finite number N, of singularities $\{\lambda_p\}$ off the real axis, C_1 may be opened to C_2 (a contour which stretches along the imaginary axis, I, and, since the set $\{\lambda_p\}$ may not be passed through, extrudes from I so as to encircle each λ_p in the first and fourth quadrants in a counter-clockwise fashion. Further if S_p is symmetric the integrand is antisymmetric and the contribution along I vanishes, so that Cauchy's theorem may be used to evaluate the integral.

Remler[3] has let

$$S_p = \prod_{\substack{\text{Poles} \\ P=1}}^{N} S_{\lambda_p}$$

where S_{λ_p} is unitary, symmetric, and first order.

(III-29) $\qquad S_{\lambda_p} = \dfrac{\lambda^2 - \lambda_p^{*2}}{\lambda^2 - \lambda_p^2}$

Therefore equation III-28 becomes

(III-30) $\qquad ik\,f_p(\theta) = \sum\limits_{p=1}^{N}{}' \dfrac{\pi}{2}\, \dfrac{P_{\lambda_p - \frac{1}{2}}(-\cos\theta)}{\cos \pi\lambda_p}(\lambda^2 - \lambda_p^{*2}) \prod\limits_{i \neq p} \dfrac{\lambda_p^2 - \lambda_i^{*2}}{\lambda_p^2 - \lambda_i^2}$

Where the coefficient, above, has the following approximation[3] (suitable for numerical computation)

$$\frac{\pi}{2}\frac{P_{\lambda_p - \frac{1}{2}}(-\cos\theta)}{\cos \pi\lambda_p} = \sqrt{\frac{\pi}{2(\lambda_p + \frac{1}{4})\sin\theta}}\left(1 - \frac{1}{64(\lambda_p + \frac{1}{4})^2}\right)\frac{e^{i\left(\frac{\pi}{4} + \lambda_p\theta\right)}}{1 + e^{2\pi i\lambda_p}}\cdot A_s$$

with

$$A_s = \sum\limits_{j=0}^{\infty}\left(-\frac{i\,e^{i\theta}}{2\sin\theta}\right)^j h_j \quad where \quad h_0 = 1, \; h_j = \frac{(j - \frac{1}{2})^2}{j(j + \lambda_p)}h_{j-1}$$

Since N is relatively small ($N \leq 16$ for the systems reported herein) the sum in equation III-30 proves to be a very efficient method of calculating $f_p(\theta)$.

The expression for a single pole, equation III-29, may be directly related to the phase shift:

$$\arg S_{\lambda_p} = \arg\left(\frac{\lambda^2 - \lambda_p^{*2}}{\lambda^2 - \lambda_p^2}\right) = -2\arg(\lambda^2 - \lambda_p^2) = -2\arg\left[(\lambda - \lambda_p)\cdot(\lambda + \lambda_p)\right]$$

$$\arg S_{\lambda_p} = -2\left[\arg(\lambda - \lambda_p) + \arg(\lambda + \lambda_p)\right]$$

Recalling that, $\eta_{\lambda_p} = \frac{1}{2} \arg S_{\lambda_p}$ we have:

$$\eta_{\lambda_p} = -\arg(\lambda - \lambda_p) - \arg(\lambda + \lambda_p)$$

$$\eta_{\lambda_p} = \tan^{-1} \frac{Im\,\lambda_p}{\lambda - Re\,\lambda_p} - \tan^{-1} \frac{Im\,\lambda_p}{\lambda + Re\,\lambda_p}$$

and, using the equivalence relation, we have

$$(III-31) \qquad \Theta_{\lambda_p} = 2\left[\frac{Im\,\lambda_p}{(\lambda + Re\,\lambda_p)^2 + (Im\,\lambda_p)^2} - \frac{Im\,\lambda_p}{(\lambda - Re\,\lambda_p)^2 + (Im\,\lambda_p)^2} \right]$$

$$\Theta_{\lambda_p} = -\frac{4\,Im\,\lambda_p^2}{|\lambda^2 - \lambda_p^2|^2}$$

These two functions are shown in figure 19 , where it is seen that Θ_{λ_p} is essentially a pulse centered at $Re\,\lambda_p$ having (for $Re\,\lambda_p \gg Im\,\lambda_p$) $\frac{1}{2}$ width $\Gamma_{1/2} \sim 2\,Im\,\lambda_p$ and depth $\sim 2/Im\,\lambda_p$
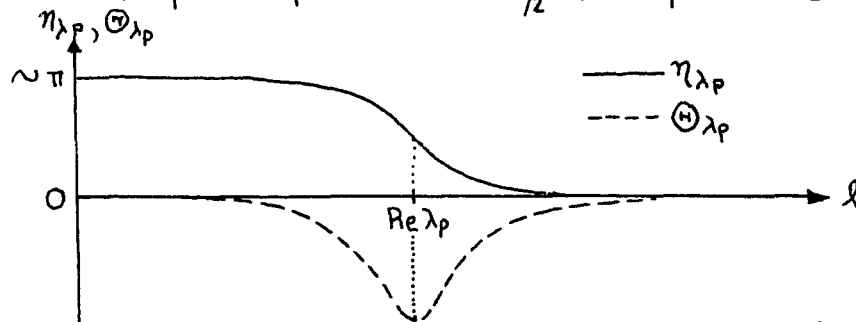
Figure 19: phase shift and deflection functions for a single pole.

If N poles are placed on a circle of radius ρ centered at λ_p , it is shown in Appendix B that

$$\eta_p = \sum_{p=1}^{N} \eta_{\lambda_p} = N\eta_{\lambda_p}$$

and

$$(III-32) \qquad \Theta_p = N\,\Theta_{\lambda_p}$$

A typical phase shift function may then be constructed, as shown in figure 20, by adding to η_p a function $\eta_{core} \equiv \eta_c$ which goes smoothly to zero for $\lambda = \lambda_c$[26] and is large and negative for $\lambda = 1/2$
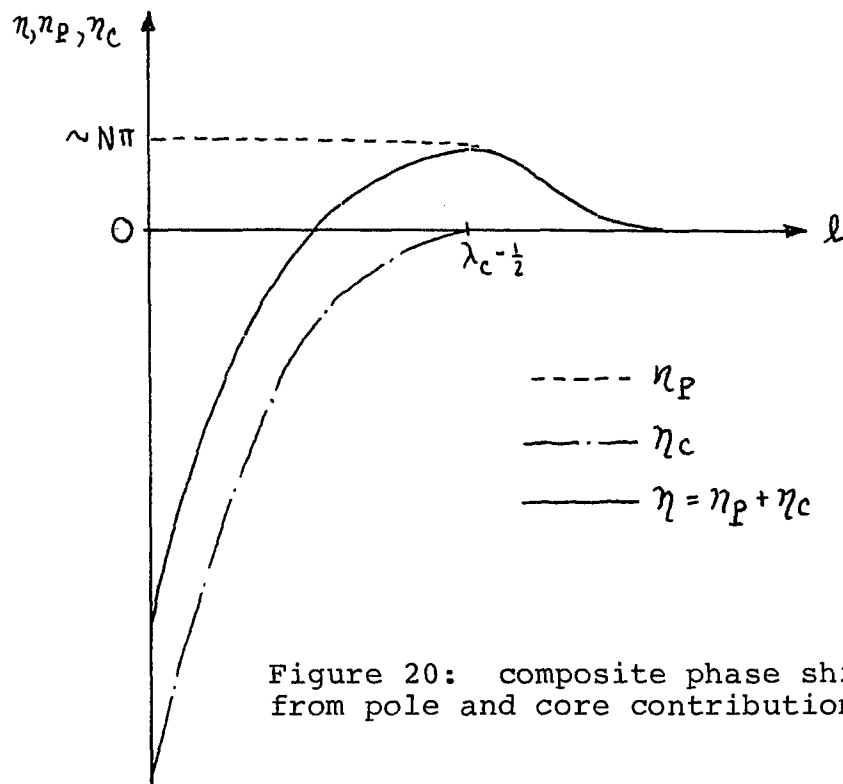
Figure 20: composite phase shift function from pole and core contributions.

Our present expression for η_c contains two curvature parameters and one parameter which determines L_o in the classical deflection function.

The complete scattering amplitude may be evaluated

$$i k f(\theta) = \sum_{\lambda = 1/2}^{\infty} \lambda \, P_{\lambda - 1/2}(\cos \theta) \left(S_p S_c - 1 \right)$$

$$\text{(III-33)} \quad i k f(\theta) = \sum_{\lambda = 1/2}^{\infty} \lambda \, P_{\lambda - 1/2}(\cos \theta) \left(S_p - 1 \right) + \sum_{\lambda = 1/2}^{\lambda_c} \lambda \, P_{\lambda - 1/2}(\cos \theta) \, S_p \left(S_c - 1 \right)$$

The first sum of equation III-33 has already been
evaluated in equation III-30; the second must only be cal-
culated from ½ to λ_c since $S_c \approx 1$ for $\lambda \geq \lambda_c$. It should be
noted that even though a part of the RFH sum is retained,
equation III-33 still represents a considerable improvement
since $\lambda_c < 150$ for all systems considered here.

Equation III-31 and III-32 allow a simple connection to
be made between the relevant semiclassical quantities and the
pole parameters, that is:

$$(\text{III-34}) \quad L_R = \text{Re}\,\lambda_P \;,\quad \Theta_R \sim \frac{2N}{\text{Im}\,\lambda_P} \;,\quad \Gamma_{1/2} \sim 2\,\text{Im}\,\lambda_P$$

The first step in recovering the intermolecular potential
is to construct the phase shift and deflection functions from the
data. This is accomplished as follows. Using the high and low
frequency oscillations observed in the experimental cross section
the pole and core parameters are initially estimated using the
semiclassical ideas presented before, together with the relations
III-34. The Remler-Regge[3] calculation is now iteratively per-
formed. That is, equation III-33 is used to calculate $\sigma(\theta)$. If
the result is not in good agreement with the experimental cross
section, the pole and core parameters are estimated again and
the calculation is repeated until satisfactory agreement between
$\sigma_{calc}(\theta)$ and $\sigma_{expt}(\theta)$ is achieved. The entire "trial-and-error"
procedure is guided by one's semiclassical intuition. A detailed
example of this method will be given in the discussion of
the 5 eV H^+ + Ar scattering system.

Having determined the phase shifts the transformation method of Vollmer [4] may be used to find $V(R)$. In this step we restrict ourselves once more to the JWKBL approximation.

We begin by writing the JWKBL phases, equation III-12 in a different but equivalent fashion

$$\eta_\ell = \lim_{R \to \infty} \left\{ \int_{R_T}^{R} dR \left[k^2 - \frac{2M}{\hbar^2} V(R) - \frac{(\ell + 1/2)^2}{R^2} \right]^{1/2} \right. $$

$$ \left. - \int_{(\ell + 1/2)/k}^{R} dR \left[k^2 - \frac{(\ell + 1/2)^2}{R^2} \right]^{1/2} \right\}$$

Making the substitution

$$\mathcal{f} = R \left[1 - \frac{V(R)}{E} \right]^{1/2}$$

We have:

$$\eta_\beta = k \int_{\beta}^{\infty} d\mathcal{f} \sqrt{\mathcal{f}^2 - \beta^2} \left[\frac{R'(\mathcal{f})}{R(\mathcal{f})} - \frac{1}{\mathcal{f}} \right]$$

where

$$\beta \equiv (\ell + 1/2)/k$$

Letting $\omega = \sqrt{\mathcal{f}^2 - \beta^2}$ and $dz = d\mathcal{f}\left(R'/R - 1/\mathcal{f} \right)$ and integrating by parts we obtain:

$$\eta_\beta = -\frac{k}{2E} \int_{\beta}^{\infty} d\mathcal{f} \, \mathcal{f} \, \frac{Q(\mathcal{f})}{\sqrt{\mathcal{f}^2 - \beta^2}}$$

with

(III-35) $\qquad Q(\mathcal{f}) \equiv 2E \ln \frac{R}{\mathcal{f}}$

Consequently the transformation equations are

(III-36) $R(\ell) = \ell \, e^{Q(\ell)/2E}$

$V(R) = E\left(1 - e^{-Q(\ell)/E}\right)$

Equation III-35 represents an integral equation for $Q(\ell)$ which Vollmer solves by multiplying both sides by

$$\beta \left(\beta^2 - u^2\right)^{-1/2}$$

and integrating over β. Thus:

$$-\frac{2E}{k} \int_u^\infty \frac{d\beta \, \beta \, \eta_\beta}{\sqrt{\beta^2 - u^2}} = \int_u^\infty \frac{d\beta \, \beta}{\sqrt{\beta^2 - u^2}} \int_\beta^\infty \frac{d\ell \, \ell \, Q(\ell)}{\sqrt{\ell^2 - \beta^2}}$$

He reduces the right hand side to[4]

$$\frac{\pi}{2} \int_u^\infty \ell \, d\ell \, Q(\ell)$$

differentiates both sides of the resulting equation with respect to ℓ , and then replaces u by ℓ obtaining the desired expression for Q .

$$Q(\ell) = \frac{4E}{\pi k} \cdot \frac{1}{\ell} \frac{d}{d\ell} \int_\ell^\infty \frac{d\beta \, \beta \, \eta_\beta}{\sqrt{\beta^2 - \ell^2}}$$

In order to numerically compute Q we have made the substitution

$$\beta = \frac{\ell}{\cos\alpha}$$

which, after some algebra, leads to the equation:

$$\text{(III-37)} \quad Q(\ell) = \frac{4E}{\pi k \ell} \left[\int_0^{\pi/2} \frac{\eta_{(\ell/\cos\alpha)} \, d\alpha}{\cos^2\alpha} \right.$$

$$\left. + \frac{k\ell}{2} \int_0^{\pi/2} \frac{\Theta_{(\ell/\cos\alpha)} \, d\alpha}{\cos^3\alpha} \right]$$

where $\quad \Theta = (2/k) \cdot \frac{d}{d(\ell/\cos\alpha)} \eta$

With the phase shift and deflection functions constructed from the data via the Remler-Regge method equation III-37 is used to find $Q(\ell)$ over a range of ℓ. Each $(\ell, Q(\ell))$ is transformed by equation III-36 to find a point $(R, V(R))$ on the intermolecular potential.

When $V(R) = 0$, $\ell = R$ and $Q(\ell) = 0$; also when $V(R) = E$, $\ell = 0$ and $Q \to +\infty$. Therefore, within the extremely small range of R between the zero of the potential and the distance of closest approach $Q(\ell)$ must rise from zero to infinity. The steep rise and large values for Q introduce numerical errors into the inversion procedure for $V(R) > 0$. The onset of these errors in first manifested by a non-monotonic behaviour of $R(\ell)$. Such anamolous effects could be minimized by rescaling E and k; this was not done, however, since the positive

region of $V(R)$ is not effectively sampled by our low energy experiments. $V(R)$ was adjusted in this region in a different way for the H^+ + Ar scattering system which shall be discussed next.

Before ending this section it should be stated that both the Remler-Regge and Vollmer methods have been separately tested. The former has yielded results which are the same as the prediction of a complete partial wave calculation; while the latter has reproduced a potential taking as input information the JWKBL phase shifts and deflection function (calculated via equation III-12) corresponding to that potential.

The entire inversion procedure has produced results for the H^++He $4eV$ scattering system[27] which are in good agreement with the ab initio potential calculated by Wolniewicz,[28] which is thought to be quite accurate.

IIID. Proton-Rare Gas Atom Scattering Experiments

We shall now detail the inversion procedure for the $5eV$ $H^+ + Ar$ experiment shown in figure 21a. The discussion concerning it will be brief since all that has been said thus far finds particular and satisfying application in this case.

The experimental cross section has been deconvoluted,[12] shown in figure 21b, to further enhance the structure seen in the data.

To begin, an initial semiclassical guess is made at the Remler-Regge pole and core parameters as follows. The two largest angle minima of the low frequency oscillations in the cross section are fit to the corresponding minima of the $Ai^2 \left(q^{-1/3} (\theta - \theta_R) \right)$ function which, from the semiclassical point of view, is the attractive contribution to the low resolution large angle scattering (equation III-22). Having thus estimated the rainbow angle θ_R and the deflection function curvature parameter q, these quantities are related to the pole parameters in equations III-34 where the additional equation $\Gamma_{1/2} = \sqrt{2\theta_R/q}$ has been used for the half width of the (assumed parabolic in this range) attractive well of $\Theta(L)$.

The high frequency oscillations in the vicinity of θ_R determine the value of $L_R + L_1$ via equation III-24.

The value of L_0, although more precisely obtainable by fitting the periodicity of the high and low frequency oscil-
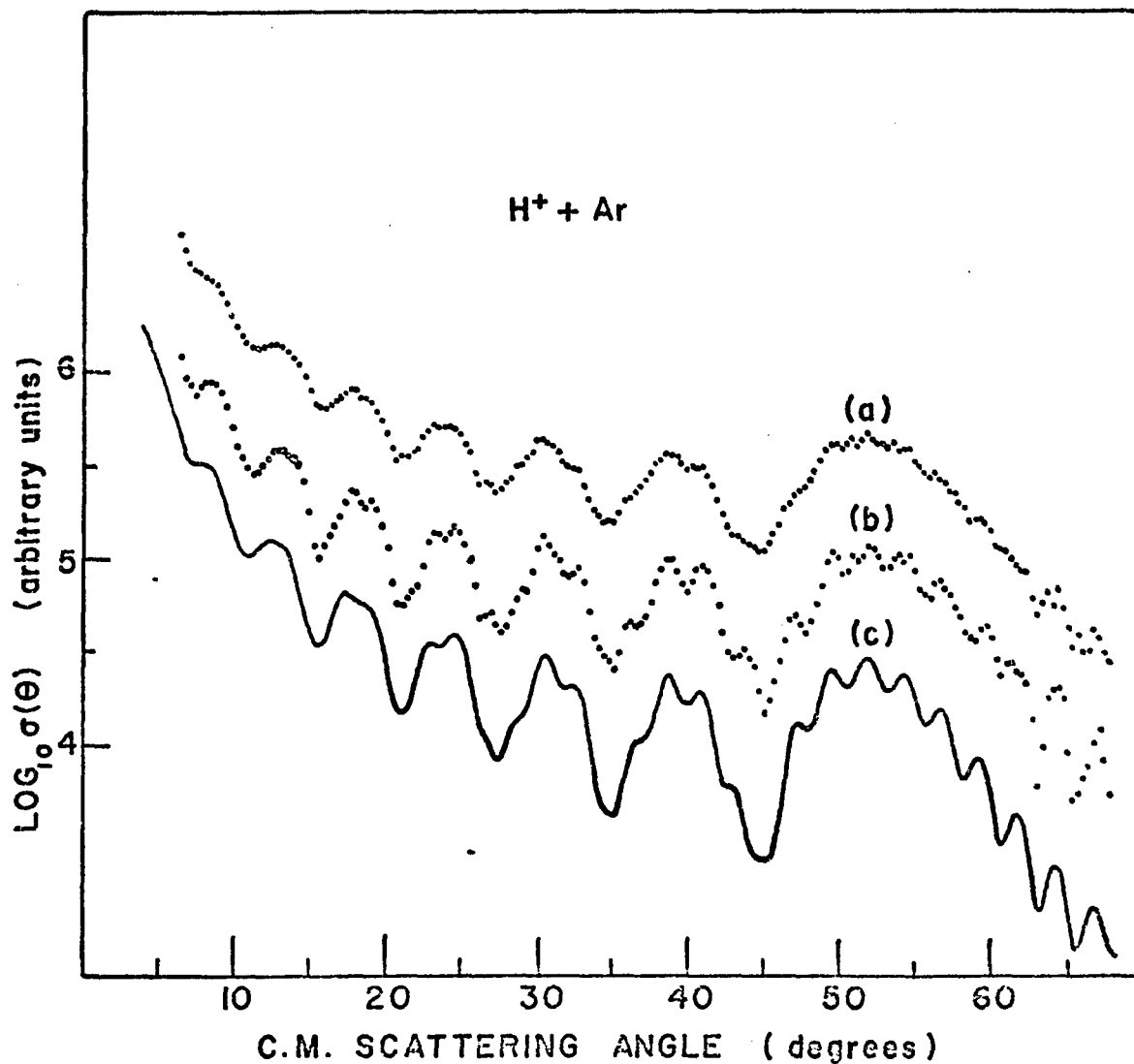
Figure 21:   (a) experimental relative differential cross
section, (b) deconvolution of the experimental differen-
tial cross section, (c) convolution of the calculated
differential cross section.   All curves pertain to the
5eV H+ + Ar elastic scattering system.

lations at small scattering angles to the predictions of
equations III-26 and III-27, has been simply approximated
as the average of L_R and L_1 . The condition that $\textcircled{H}(L)$
goes smoothly through $\left\{(0,\pi),(L_1,\theta_R),(L_0,0),(L_R,-\theta_R)\right\}$
with curvature q_D at the last point mentioned allows the
initial estimation of L_R and therefore $Re\lambda_p$.

More sophistication than this is not necessary since
the next step is to iteratively use the Remler-Regge method
in order to reproduce all details of the experimental cross
section. This has been done until the convoluted calculation,
figure 21c, is in excellent agreement with the deconvoluted
data, figure 21b.

The resulting phase shift function, shown in figure 22 ,
together with the semiclassically equivalent deflection
function have been used in Vollmer's method to recover the
intermolecular potential shown in figure 23 and tabulated
in Table 2 .

To verify and extend the repulsive portion of the in-
verted intermolecular potenital, it was extrapolated from
$V(R) \gtrsim 0$ to about $30eV$. Velocity independence was explicitly
assumed and this intermolecular potential was used to predict
the cross section at $14eV$ collision energy. The result was
compared to a higher energy experiment which showed little
of the interference effects but presented a large decrease of
intensity on the dark side of θ_R (corresponding to scattering
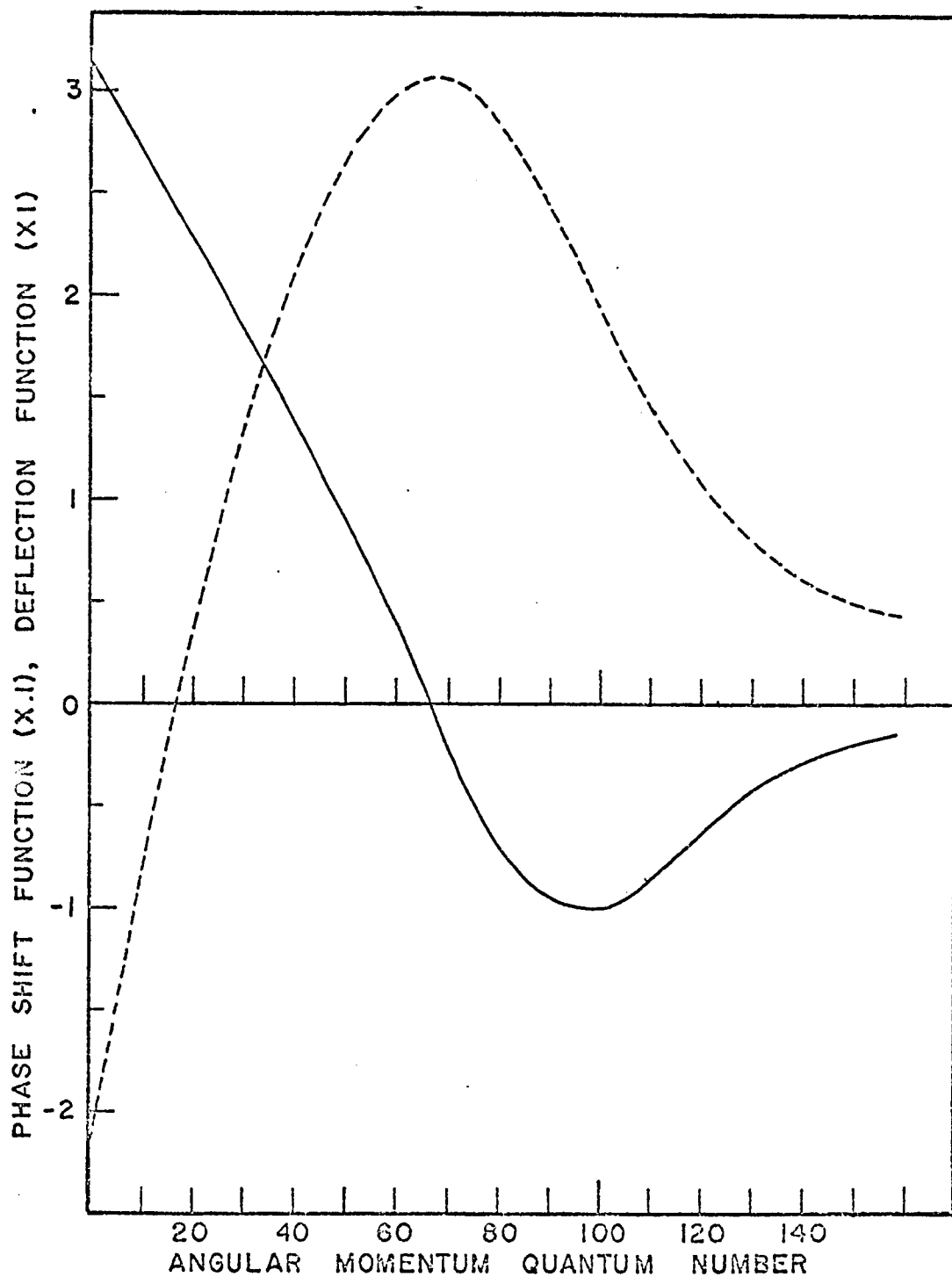
Figure 22: dashed line - phase shift function value (multiplied by .1), solid line - deflection function. Both curves correspond to the 5 eV H+ + Ar scattering system.
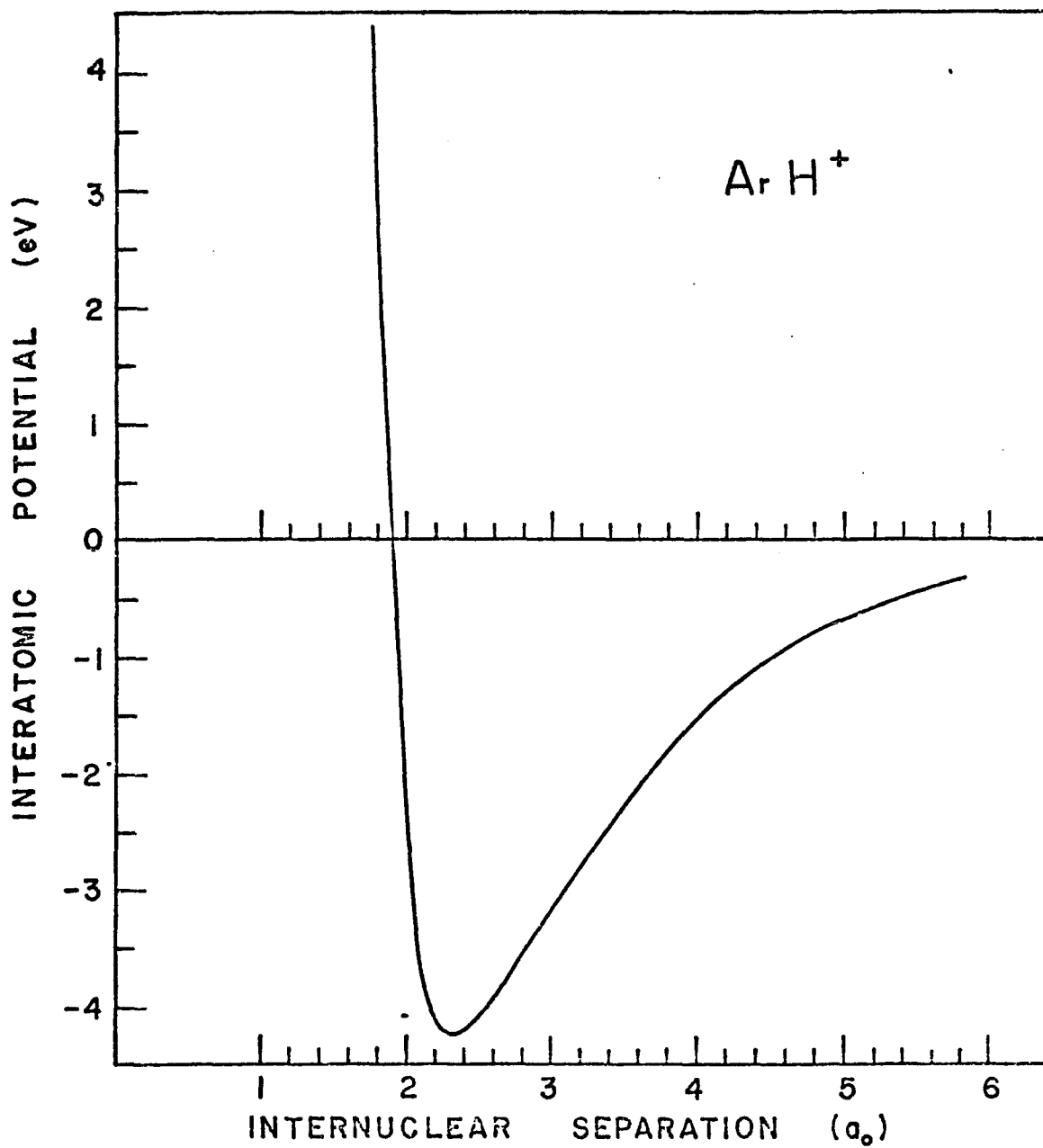
Figure 23: inverted intermolecular potential for the (ArH)$^+$ system.

Table 2: ArH$^+$ intermolecular potential

R in a$_o$	V(R) in eV
1.750	+7.25
1.775	+4.40
1.804	+2.40
1.807	+2.00
1.819	+1.60
1.835	+1.20
1.848	+0.77
1.868	+0.36
1.889	-0.06
1.912	-0.47
1.934	-0.90
1.955	-1.33
1.976	-1.77
1.998	-2.22
2.020	-2.66
2.045	-3.08
2.076	-3.46
2.115	-3.76
2.162	-3.99
2.219	-4.14
2.284	-4.21
2.357	-4.22
2.439	-4.16
2.528	-4.04
2.625	-3.89
2.728	-3.71
2.837	-3.50
2.951	-3.29
3.071	-3.07
3.196	-2.83
3.328	-2.59
3.465	-2.35
3.606	-2.11
3.750	-1.88
3.894	-1.68
4.037	-1.49
4.178	-1.33
4.316	-1.18
4.452	-1.06
4.585	-0.95
4.715	-0.85
4.843	-0.76
4.968	-0.69

for $\Theta > \Theta_R$). The results of this calculation were in gratifying agreement with the data as shown in figure 24.

Because of the detailed nature of the 5eV experiment as well as the validity of the approximations (JWKBL phase shifts and Born-Oppenheimer theorem) for the H^+ + Ar system at this energy, we believe the intermolecular potential in figure 23 is highly accurate.

By comparison with the $(ArH)^+$ data the 6eV H^+ + Kr experiment, figure 25, gives less useful information. The cross section, which at first glance appears to be quite detailed, shows no fine oscillations and therefore presents no information to accurately determine the L scale of the deflection function. We will expand on this point.

The shape of the attractive well of $\Theta(L)$ may be found as before; namely q_b and Θ_R can be inferred from the large angle low frequency oscillations and equation III-22. The small angle low frequency component and equation III-26 specify the deviation of branch 3 of $\Theta(L)$ from a parabola for $\Theta < 30°$. This, however, is all that we can accurately determine.

The infinite set of deflection functions $\{\Theta_i\}$ shown in figure 26 all have identically shaped attractive portions, all equally well reproduce the periodicity of the low frequency component of the cross section, and individually lead to the corresponding set of quite different potentials $\{V_i\}$
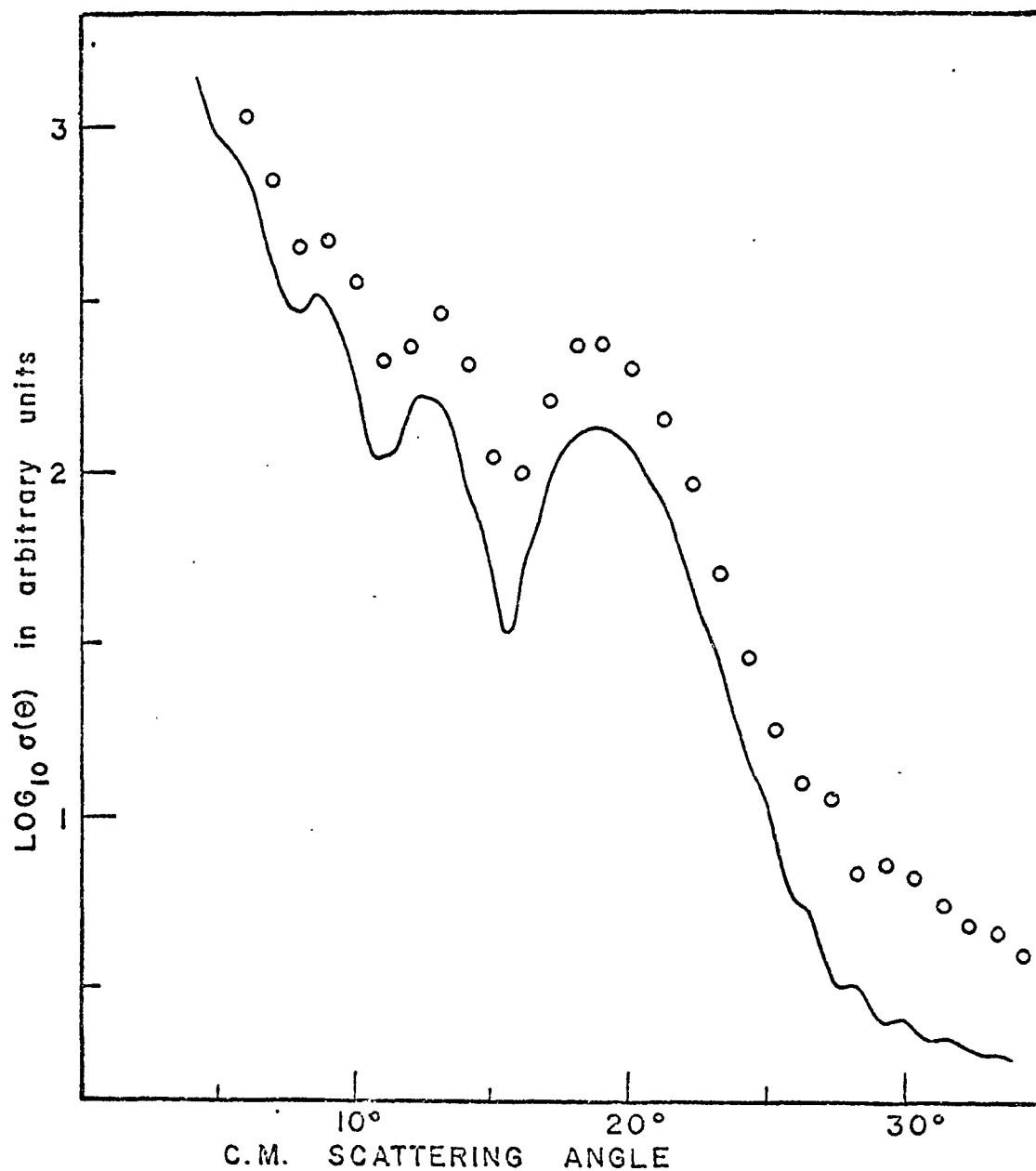
Figure 24: open circles - experimental relative differential cross section, solid line - convolution of calculated cross section predicted by the intermolecular potential in figure 23. Both cross sections pertain to the 14 eV H^+ + Ar scattering system. Please note that the curve representing the calculation has been shifted down to facilitate comparison with the experimental result.
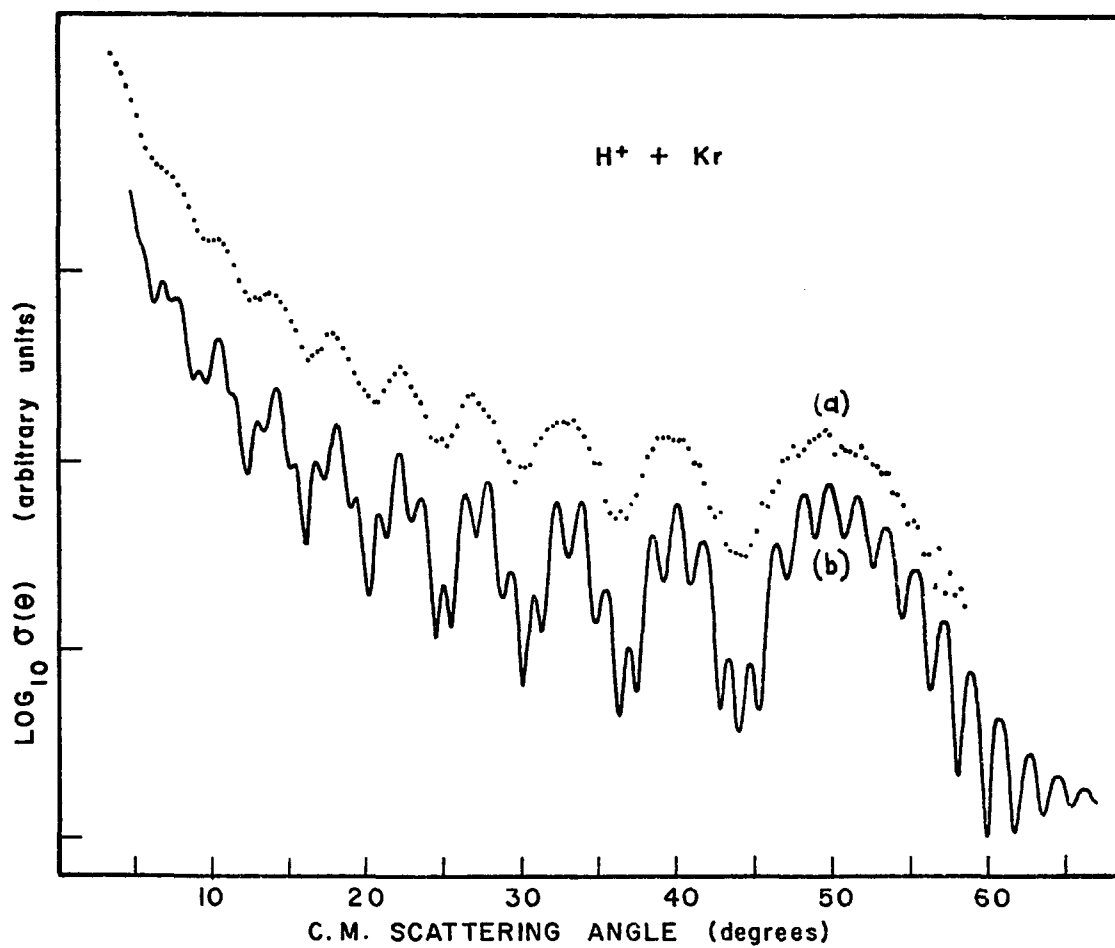
Figure 25 : (a) experimental relative differential cross section, (b) convolution of the calculated cross section. Both curves pertain to the 6eV H^+ + Kr elastic scattering system.

in figure 27.
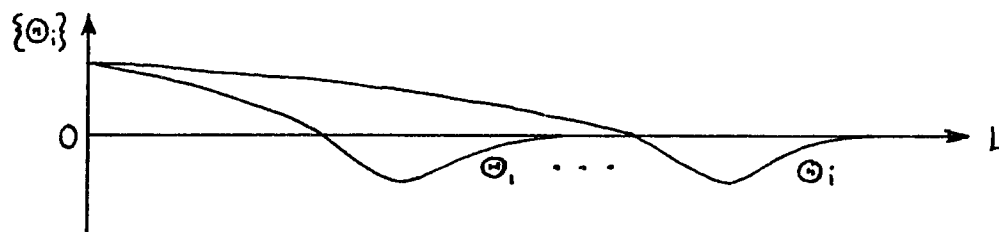
Figure 26:   the set of deflection functions which all predict the same periodicity for the low frequency oscillations in $\sigma(\theta)$.
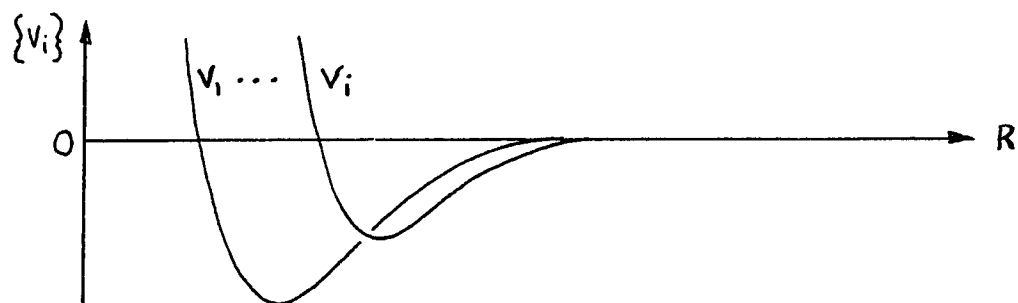
Figure 27:   the potentials corresponding to the deflection functions in figure 26.

The observation (based on the H^+ + He, H^+ + Ne, and H^+ + Ar systems where fine oscillations have been resolved) that the average small angle low frequency periodicity has

$$\frac{L_1 - L_2}{L_0} \sim 2$$

provides a crude device to fix the scale of L. This assumption was invoked, and the potential of figure 28 and Table 3 corresponding to the calculated cross section in figure 25 was recovered using the Remler-Regge[3] and Vollmer[4] treatments.

This potential is clearly much less reliable than the $(ArH)^+$ result.
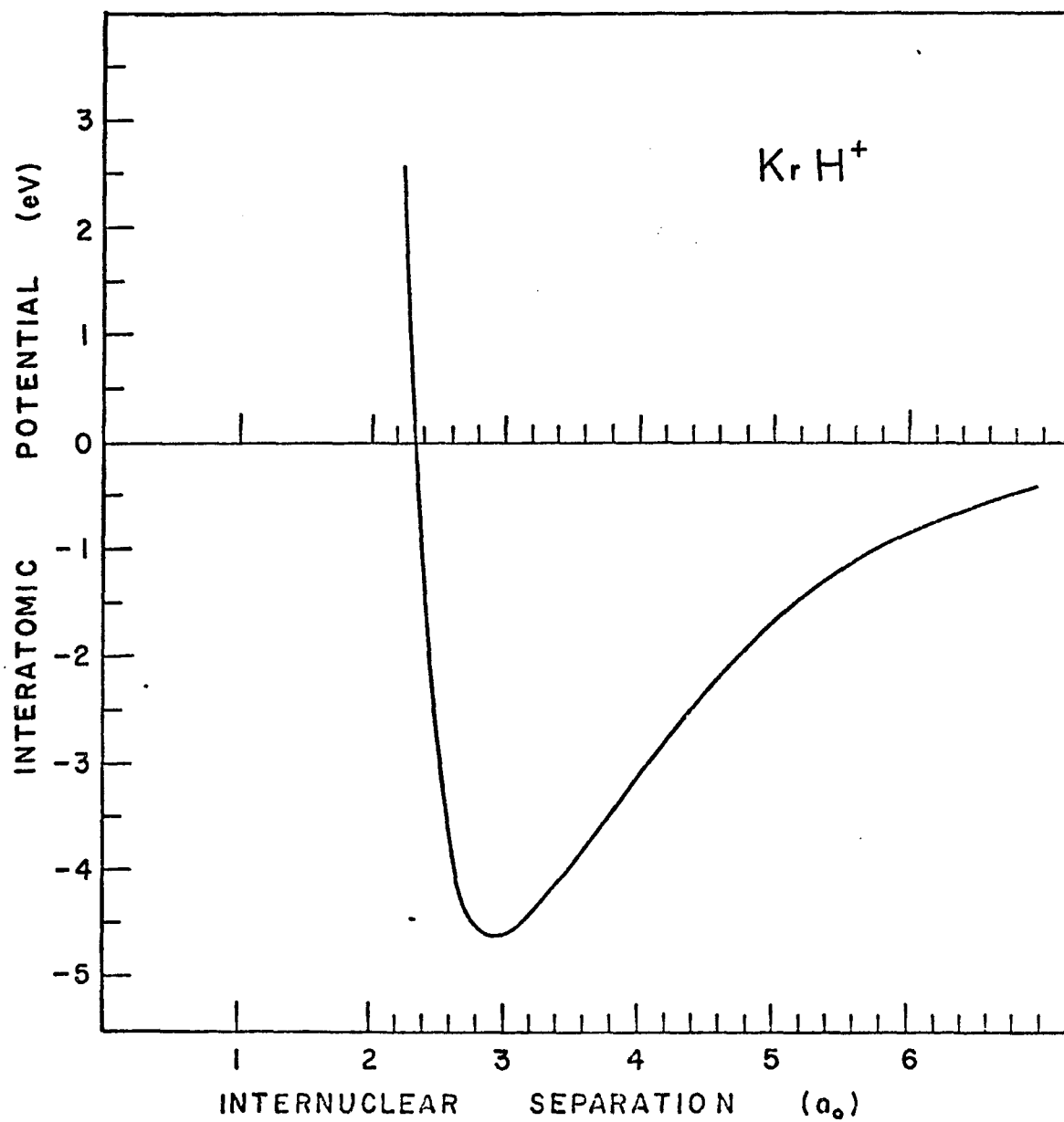
Figure 28 : inverted intermolecular potential for the (KrH)$^+$ system.

Table 3 :   Inverted points on V(R) for (KrH)$^+$

R in a_o	V(R) in eV
2.254	+1.74
2.269	+1.34
2.281	+0.92
2.300	+0.51
2.320	+0.10
2.342	-0.30
2.367	-0.69
2.393	-1.08
2.420	-1.46
2.449	-1.85
2.476	-2.23
2.504	-2.61
2.532	-3.00
2.561	-3.37
2.594	-3.71
2.633	-4.00
2.678	-4.25
2.730	-4.43
2.790	-4.55
2.855	-4.62
2.928	-4.65
3.006	-4.62
3.091	-4.55
3.182	-4.45
3.278	-4.32
3.380	-4.17
3.485	-4.00
3.596	-3.82
3.710	-3.63
3.828	-3.43
4.078	-3.02
4.349	-2.58
4.633	-2.15
4.920	-1.77
5.200	-1.45
5.470	-1.20
5.740	-1.00
6.000	-0.85
6.240	-0.71
6.480	-0.60
6.720	-0.51
6.950	-0.44

Table 4 :   Pole and core parameters for the one state systems

System	Energy	L_0	N	Re λ_p	Im λ_p
H^+ + Kr	6eV	91.5	16	138.15	33.55
H^+ + Ar	5eV	67.0	13	100.20	25.78

The final pole and core parameters for this, as well as
the preceding experiment, are listed in Table 4.

Some ideas which may be of help to determine the L scale of
$\oplus$ (L) in future low resolution experiments and analyses are
presented in Appendix C. The best rule to follow is, however:
resolve the high frequency oscillations.

IV. ELASTIC SCATTERING FOR THE TWO STATE CURVE CROSSING SYSTEM $(NeHe)^+$

The experimental differential elastic cross section for the He^+ + Ne system at 40eV collision energy is shown in figure 29. By comparison to the 5eV $(ArH)^+$ data this experimental cross section looks very simple; and, one would hope that its analysis would prove easy, almost trivial.

Nothing could be farther from reality. To a theoretician, the problem appears to be one of eleven electrons and two nuclei in relatively close proximity existing in a variety of molecular states many of which are coupled together. In the present treatment we shall have recourse to two potentials corresponding to two classical trajectories as well as to a third function which represents the probability of following one of the other of these paths. This is not all, however, since two additional "phase shift" functions, arising from the coupling itself, will be found necessary to describe our scattering experiment.

We shall endeavor to be quite explicit in the discussion about the diabatic and adiabatic terms. In describing the new theoretical work of Sidis[6] and Delos[7] we shall attempt to be clear about their results but the intermediate steps will be outlined only; a complete and rigorous treatment being outside the scope of this dissertation.

The subject of curve crossing is by no means closed and
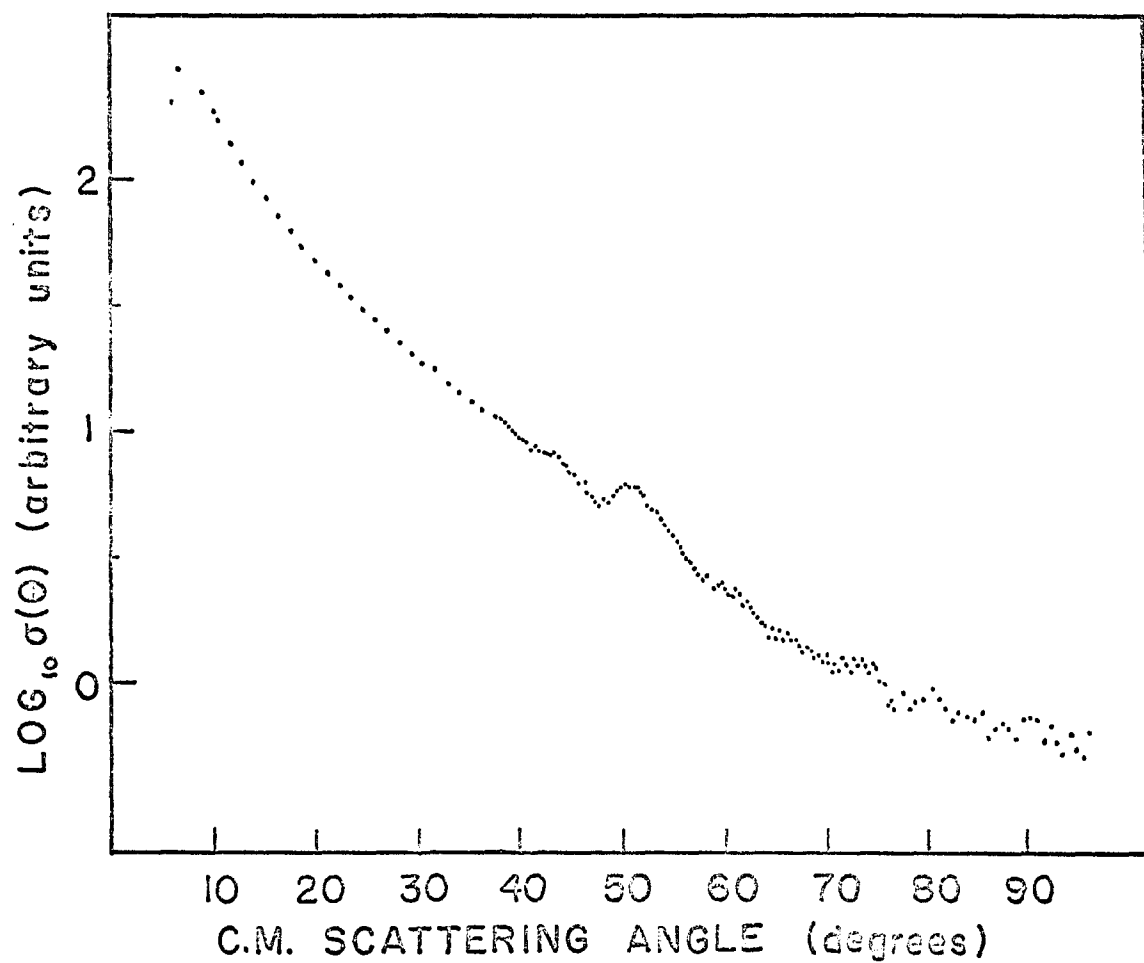
Figure 29: experimental differential elastic scattering cross section for He⁺ + Ne at 40ₑᵥ.

the present work should be taken as a phenomenological indication, rather than proof, of the viability of the most modern theory; a theory which does, in the low energy He^+ + Ne case, reduce to the fairly clear explanation that the uncomplicated aspect of the experimental data portends.

IVA. Adiabatic, Diabatic, and Quasi-Diabatic Potentials

Let us begin this section with a discussion of the potent-
ials. As in Section IIIA we write the complete Schroedinger
equation in C.M. coordinates:

$$\left(-\frac{\hbar^2}{2M_e}\sum_{i=1}^{N}\nabla_i^2 - \frac{\hbar^2}{2M}\nabla_R^2 + V_T(\vec{r}_i,\vec{R}) - E\right)\Psi = 0$$

and expand Ψ . This time we explicitly use the complete set
of molecular wave functions $\mathscr{G}_J(\vec{r}_i,\vec{R})$ since the coupling terms
will be of paramount importance,

(IV-1) $\Psi = \sum_J F_J^a(\vec{R})\,\mathscr{G}_J(\vec{r}_i,\vec{R})$

where, the superscript a refers to "adiabatic."

Each of the $\mathscr{G}_J$ satisfies the electronic Schroedinger
equation:

(IV-2) $\left(-\frac{\hbar^2}{2M_e}\sum_{i=1}^{N}\nabla_i^2 + V(\vec{r}_i,\vec{R})\right)\mathscr{G}_J(\vec{r}_i,\vec{R}) = E_J^a(R)\,\mathscr{G}_J(\vec{r}_i,\vec{R})$

where the $V(\vec{r}_i,\vec{R})$ in the above equation does not include the
coulomb repulsion $V_{coul} = Z_a Z_b e^2/R$

Inserting equation IV-1 into the complete equation, pre-
multiplying by $\mathscr{G}_K^*(\vec{r}_i,\vec{R})$ and integrating over electron coordi-
nates we obtain:

(IV-3)

$$\left(-\frac{\hbar^2}{2M}\nabla_R^2 + V_{coul} + E_K^a(R) - E\right) F_K^a(\vec{R})$$

$$= \frac{\hbar^2}{2M}\sum_J \left(\langle \varphi_K|\nabla_R^2|\varphi_J\rangle + 2\langle \varphi_K|\nabla_R|\varphi_J\rangle \cdot \nabla_R\right) F_J^a(\vec{R})$$

In the above equation we define the non-crossing[29] adiabatic potential for the Kth molecular state to be (apart from an additive constant)

(IV-4) $$V_K^a(R) = V_{coul} + E_K^a(R)$$

where $E_K^a(R)$ has been defined in equation IV-2.

For low collision velocities we proceed as in Section IIIA and neglect the diagonal terms on the right of equation IV-3. Furthermore, in this same limit (slowly moving nuclei) Sidis[6] lets $\langle \varphi_K|\nabla_R|\varphi_J\rangle \rightarrow \langle \varphi_K|\frac{d}{dR}|\varphi_J\rangle \hat{R}$ and therefore:

(IV-5) $$\left(-\frac{\hbar^2}{2M}\nabla_R^2 + V_K^a - E\right) F_K^a(\vec{R})$$

$$= \frac{\hbar^2}{2M}\sum_{J\neq K} \left(\langle \varphi_K|\nabla_R^2|\varphi_J\rangle + 2\langle \varphi_K|\frac{d}{dR}|\varphi_J\rangle\frac{d}{dR}\right) F_J^a(\vec{R})$$

If the remaining terms on the right hand side are small or zero then $V_K^a(R)$ specifies the nuclear trajectory. If on the other hand they are large, equation IV-5 is a complicated expression and $V_K^a(R)$ loses its meaning in this context. Let us examine $\langle \varphi_K|\frac{d}{dR}|\varphi_J\rangle$ to see when this will occur. From

equation IV- 2:

$$H_{el} \, |\varphi_K\rangle = E_K^a \, |\varphi_K\rangle$$

So that,

$$\langle \varphi_K | \frac{d}{dR} H_{el} | \varphi_J \rangle = E_J^a \langle \varphi_K | \frac{d}{dR} | \varphi_J \rangle$$

$$= \langle \varphi_K | \left(\frac{d V(\vec{r}_i,\vec{R})}{dR}\right) | \varphi_J \rangle + \langle \varphi_K | H_{el} \frac{d}{dR} | \varphi_J \rangle$$

In Appendix E it is shown that

$$\langle \varphi_K | H_{el} \frac{d}{dR} | \varphi_J \rangle = E_K^a \langle \varphi_K | \frac{d}{dR} | \varphi_J \rangle$$

Therefore,

$$\text{(IV-6)} \qquad \langle \varphi_K | \frac{d}{dR} | \varphi_J \rangle = \frac{\langle \varphi_K | \left(\frac{d}{dR} V(\vec{r}_i,\vec{R})\right) | \varphi_J \rangle}{E_J^a - E_K^a}$$

If figure 30 represents the results of an adiabatic cal-
culation for two states φ_K and φ_J of the same molecular
symmetry, then in the region of R_c, $|E_J^a - E_K^a|$ is small and
equation IV- 6 tells us that $\langle \varphi_K | \frac{d}{dR} | \varphi_J \rangle$ is large and the
states are strongly coupled; so that the adiabatic potentials
are not good in this region. On the other hand, far away from
R_c the potentials are smooth and widely spaced so that $V_J^a(R)$
and $V_K^a(R)$ adequately describe the nuclear motion (i.e.
equation IV- 5 with the right hand side equal to zero is valid).
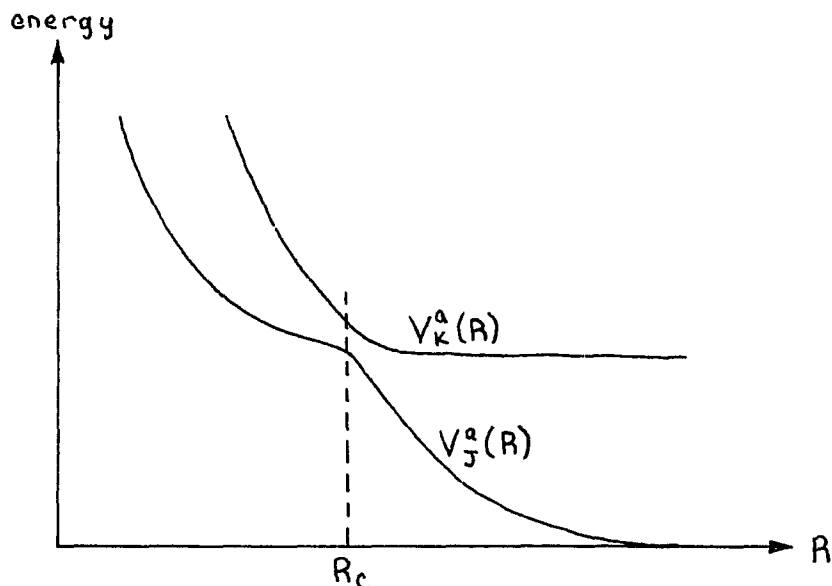
Figure 30: adiabatic potentials for the two state problem.

We will now discuss another representation, the diabatic, which allows the coupling to be much more readily dealt with.

This representation was originally suggested by Lichten[30] and has been rigorously defined by Smith[31]. Let us define the functions $\mathcal{X}_J$ as those which diagonalize $\frac{d}{dR}$ so that

(IV-7) $$\left\langle \mathcal{X}_K \left| \frac{d}{dR} \right| \mathcal{X}_J \right\rangle = \delta_{KJ}$$

Since the $\mathcal{X}_J$ are not exact solutions of the electronic Schroedinger equation, $\langle H_{el} \rangle$ may have off-diagonal elements in this representation; and the diabatic curves defined by,

(IV-8) $$V_K^d(R) = \left\langle \mathcal{X}_K \left| H_{el} \right| \mathcal{X}_K \right\rangle + V_{coul} + constant$$

can cross. The complete Schroedinger equation is now solved

by expanding,

$$\Psi = \sum_{J} \chi_J (\vec{r_i}, \vec{R}) \, F_J^d(\vec{R})$$

Proceding exactly as before we find:

(IV-9)
$$\left(-\frac{\hbar^2}{2M} \nabla_R^2 + V_K^d - E \right) F_K^d(\vec{R})$$

$$= \frac{\hbar^2}{2M} \sum_{J \neq K} \left(\langle \chi_K | \nabla_R^2 | \chi_J \rangle + 2 \langle \chi_K | \frac{d}{dR} | \chi_J \rangle \frac{d}{dR} \right) F_J^d(\vec{R})$$

$$- \sum_{J \neq K} \langle \chi_K | H_{el} | \chi_J \rangle F_J^d(\vec{R})$$

For low collision velocity Sidis[6] neglects the angular portion of ∇_R^2 and thus:

$$\nabla_R^2 = \frac{d^2}{dR^2} + \frac{2}{R} \frac{d}{dR}$$

Further, he expands $\frac{d^2}{dR^2}$ as

$$\langle \chi_K | \frac{d^2}{dR^2} | \chi_J \rangle = \sum_{\lambda} \left(\langle \chi_K | \frac{d}{dR} | \chi_\lambda \rangle \langle \chi_\lambda | \frac{d}{dR} | \chi_J \rangle \right)$$

$$+ \frac{d}{dR} \langle \chi_K | \frac{d}{dR} | \chi_J \rangle$$

Therefore, all but the last set of terms in equation IV-9 are, by the requirement of equation IV-7, identically zero, so:

(IV-10)
$$\left(-\frac{\hbar^2}{2M} \nabla_R^2 + V_K^d - E \right) F_K^d(\vec{R}) = -\sum_{J \neq K} \langle \chi_K | H_{el} | \chi_J \rangle F_J^d(\vec{R})$$

Equation IV-10 shows that the smaller $\langle \chi_K \mid H_{el} \mid \chi_J \rangle$ is, the more truly $V_K^d(R)$ represents the intermolecular potential.

For example we could, in our particular case, develop as follows. First, simplify to a two state process. Next, allow the left hand side of equation IV-10 to represent the unperturbed Schroedinger equation. And finally, treat the one remaining term on the right side as a time dependent perturbation. The time dependency comes through a prescription of the unperturbed classical path R(t); while the fact that perturbation theory can be used at all is due to the fact that the relevant $\langle \chi_K \mid H_{el} \mid \chi_J \rangle$ is small (Sidis[6]calculates .26eV for the lowest energy crossing of the (NeHe)[+] system).

Let us now draw a connection between the two representations. At the crossing of two diabats, figure 31, the partial $\langle H_{el} \rangle$ matrix looks like:

$$\begin{pmatrix} \langle \chi_J \mid H_{el} \mid \chi_J \rangle & \langle \chi_J \mid H_{el} \mid \chi_K \rangle \\ \langle \chi_K \mid H_{el} \mid \chi_J \rangle & \langle \chi_K \mid H_{el} \mid \chi_K \rangle \end{pmatrix}$$

Since the matrix elements are to be evaluated at R_c, however:

$$\langle \chi_J \mid H_{el} \mid \chi_J \rangle = \langle \chi_K \mid H_{el} \mid \chi_K \rangle \equiv E_c$$

$$\langle \chi_J \mid H_{el} \mid \chi_K \rangle = \langle \chi_K \mid H_{el} \mid \chi_J \rangle \equiv H_{KJ}$$

So that the 2 X 2 matrix becomes

$$\begin{pmatrix} E_c & H_{KJ} \\ H_{KJ} & E_c \end{pmatrix}$$

To find the adiabatic energies, E_J^a and E_K^a, we diagonalize obtaining:

$$E_{J,K}^a = E_c \pm H_{KJ}$$

and

$$E_J^a - E_K^a = 2 H_{KJ}$$

This result is also shown in figure 31.
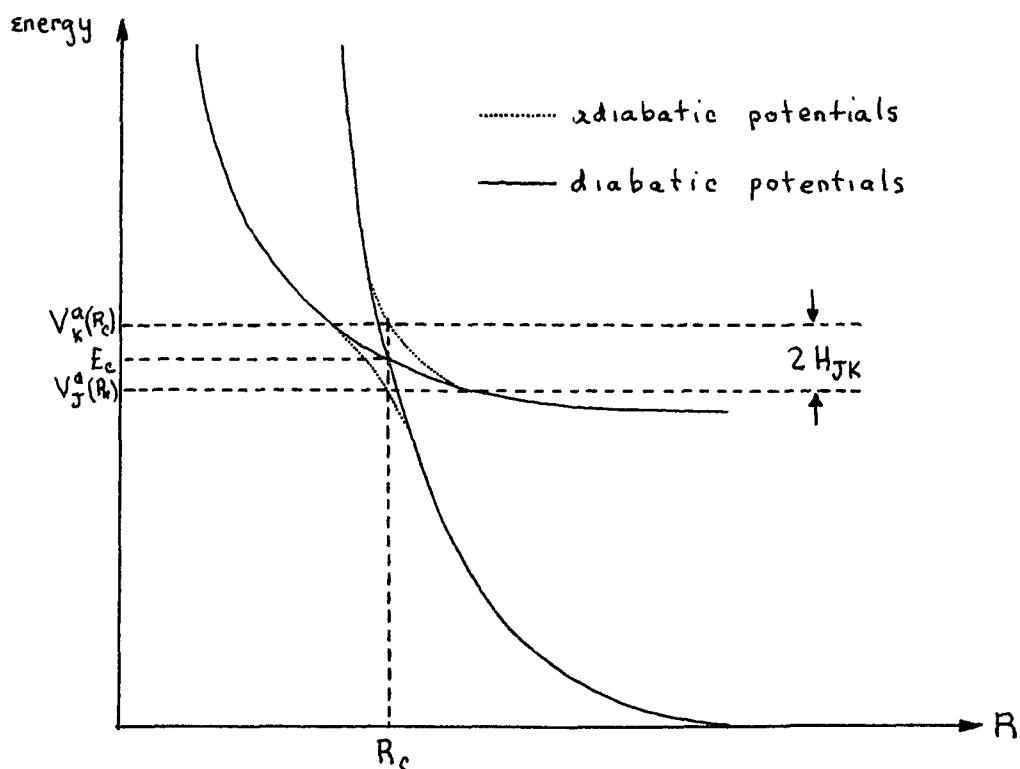
Figure 31:   a comparison of the diabatic and adiabatic potentials in the vicinity of the crossing.

Since equation IV-7 defines the functions, χ, apart from an R-independent unitary transformation, these functions are chosen to solve equation IV-7 and to separate to the correct asymptotic separate atom limits; and thus they coalesce to the adiabats as R becomes large.

The adiabatic representation, although more readily found, proves insufficient in the case where two adiabatic curves are close together. The coupling between the states appears as a complicated breakdown of the Born-Oppenheimer approximation involving not only the matrix elements $\left\langle \frac{d}{dR} \right\rangle$ and $\left\langle \frac{d^2}{dR^2} \right\rangle$, but the operator $\frac{d}{dR}$ itself. The coupling terms in the diabatic representation are simply off-diagonal matrix elements of H_{el} which are more easily calculable and have been found to be small and slowly varying for the case in question.

Determining the diabatic representation, according to equation IV-7, proves to be the problem. To accomplish this Sidis notices that $\frac{d}{dR}$ acts on a Slater determinant wave function like a one electron operator.[6] Consequently, if two such wave functions, $\psi_{1,2}$, differ by two or more molecular orbitals, MO's, the matrix element $\left\langle \psi_1 \left| \frac{d}{dR} \right| \psi_2 \right\rangle$ will be zero. He therefore chooses to represent many of the crossing diabatic states by determinantal wave functions whose elements are MO's, the columns of which do differ by two or more orbitals. He finds that $\left\langle \frac{d}{dR} \right\rangle$ is not identically zero for some of the states, but since these correspond to smooth

well-separated curves in the adiabatic case this representation is called quasi-diabatic. The two states which will be of particular interest to us differ by two MO's and so for our case this representation is essentially the diabatic.

The MO's are constructed as linear combinations of Slater type atomic orbitals the parameters of which Sidis obtains from the work of Gilbert and Wahl.[32] The determinantal wave functions are then constructed and the expansion coefficients in the individual MO's are varied to minimize the diagonal element $\langle H_{el} \rangle$ at each R.

The lowest energy crossing is found to be the intersection of the curves corresponding to the two molecular states

State 1: $1\sigma^2, 2\sigma^2, 4\sigma^2, 1\pi^4, 3\sigma ; \; ^2\Sigma^+$

which Sidis calls the B state

State 2: $1\sigma^2, 2\sigma^2, 3\sigma^2, 1\pi^4, 5\sigma ; \; ^2\Sigma^+$

which Sidis calls the C state

State 1 connects with the ground states of both ion and atom:

State 1: $He^+ (1s ; \; ^2S), \; Ne (1s^2, 2s^2, 2p^6 ; \; ^1S)$

while State 2 corresponds, at large R, to the excited state of the atom:

State 2: $He^+ (1s ; \; ^2S), \; Ne^* (1s^2, 2s^2, 2p^5, 3s ; \; P^o)$

Sidis locates the crossing at $R_c = 1.86 \, a_o, \; E = 17.8 \, eV$

and finds that

$$\langle \chi_1 | H_{el} | \chi_2 \rangle \Big|_{R=R_c} \equiv V_{12}(R_c) = .26\,eV$$

The points which he has calculated for these two curves as well as the analytic functions which we have employed to represent them will be seen in Section IIIC.

We shall use these calculations of $V_1(R), V_2(R), V_{12}(R)$ in our initial attempt to predict the $He^+ + Ne$ elastic scattering cross section. It will be seen, in Section IVC, that only a slight modification to the potentials is necessary in order to bring $\sigma_{calc}(\theta)$ into good agreement with $\sigma_{expt}(\theta)$.

IVB. Solution of the Coupled Equations and Connection with the Scattering Formalism

The methods presented in Section IVA have greatly reduced the difficulty of solving the complete Schroedinger equation. The information provided to this Section, then, consists of two coupled equations in the diabatic (really, quasi-diabatic) representation. Specializing equation IV-10 to two states we have:[33]

$$\left(-\frac{\hbar^2}{2M}\frac{d^2}{dR^2} + V_1(R) - E\right)\mathcal{F}_1(R) + V_{12}\mathcal{F}_2(R) = 0$$

(IV-11)

$$\left(-\frac{\hbar^2}{2M}\frac{d^2}{dR^2} + V_2(R) - E\right)\mathcal{F}_2(R) + V_{21}\mathcal{F}_1(R) = 0$$

where, for instance, the terms $V_1(R), V_2(R), V_{21}(R)$ and $V_{12}(R)$ are known from the work of Sidis.[6]

In Section IVB, therefore, we shall solve the set IV-11 and relate the solution to the differential cross section. This shall be done by following the method of Delos.[7] Actually Delos presents four methods of solution,[7] and, before discussing any of them in detail, a few general remarks are in order. In all cases the $\mathcal{F}(R)$ functions in equation IV-11 are expanded in terms such as

$$C(z)\, e^{i\hbar^{-1}\int \omega(z)\,dz}$$

and the solution of Schroedinger's equation is reduced to solving coupled first order equations for the C's, which are

called the "classical" equations. Two of the derivations take ω as a momentum and z as the conjugate displacement. In one of these (called diabatic configuration space) the momentum corresponds to the diabatic potentials of equations IV-11.

$$\omega_{1,2} = \sqrt{2M(E - V_{1,2})}$$

The other (adiabatic configuration space) still solves what we have previously termed the diabatic equations (IV-11) but is called adiabatic since ω is taken to be:

$$\omega_{+,-} = \left\{ 2M \left[\frac{(E+V_1) + (E+V_2)}{2} \pm \sqrt{\left(\frac{(E+V_1) - (E+V_2)}{2} \right)^2 + V_{12}^2} \right] \right\}^{1/2}$$

These are just the momenta corresponding to a diagonalization of

$$\begin{pmatrix} V_1 & V_{12} \\ V_{12} & V_2 \end{pmatrix}$$

that is, to the adiabatic potentials. As we shall see, the configuration space representations break down when the classical turning point is in the vicinity of the crossing. To establish the validity of his treatment for this region Delos transforms equations IV-11 to momentum space and derives (where the roles of ω and z are interchanged) the same classi-

cal equations,[7] this time making approximations which are valid
for the turning point close to the crossing but invalid else-
where. [34]

In order to derive the classical equations and connect
their solutions with the scattering problem we shall outline
Delos' method in the diabatic configuration space representation.

First, expand as:

$$\mathcal{F}_1(R) = a_{1+}(R) e^{i\hbar^{-1} S_1(R)} + a_{1-}(R) e^{-i\hbar^{-1} S_1(R)}$$

(IV-12)

$$\mathcal{F}_2(R) = a_{2+}(R) e^{i\hbar^{-1} S_2(R)} + a_{2-}(R) e^{-i\hbar^{-1} S_2(R)}$$

with

$$S_{1,2}(R) = \int_{R_{T_{1,2}}}^{R} P_{1,2}(R)\, dR$$

Here, already, although no approximations have yet been
made the problem is cast in a classical light; and one sees
in equations IV-12 the nuclei (i.e. the C.M. coordinate R)
moving up to and away from the classical turning points $R_{T_{1,2}}$
with diabatic momenta $P_{1,2}$ (which, since both possibilities
have been explicitly allowed in equation IV-12, is in-
herently a positive quantity).

Since substitution of equation IV-12 into equation IV-11
would give two equations in four unknowns, Delos is free to
make an additional two restrictions on the coefficients, as

follows:

$$\left(\frac{d}{dR}a_{1+}\right)e^{i\hbar^{-1}S_1} + \left(\frac{d}{dR}a_{1-}\right)e^{-i\hbar^{-1}S_1} = 0$$

(IV-13)

$$\left(\frac{d}{dR}a_{2+}\right)e^{i\hbar^{-1}S_2} + \left(\frac{d}{dR}a_{2-}\right)e^{-i\hbar^{-1}S_2} = 0$$

This eliminates the second order terms, and with the additional substitution:

$$b_{1,2\pm} = \sqrt{P_{1,2}}\ a_{1,2\pm}$$

equations IV-11 and IV-13 give four complex first order equations for the new coefficients, b:

(IV-14)

$$\frac{d}{dR}\begin{pmatrix} b_{1+} \\ b_{1-} \\ b_{2+} \\ b_{2-} \end{pmatrix} = \begin{pmatrix} 0 & \frac{\left(\frac{d}{dR}P_1\right)}{2P_1}e^{-2iS_1} & \frac{MV_{12}e^{i\hbar^{-1}(S_2-S_1)}}{i\hbar\sqrt{P_1P_2}} & \frac{MV_{12}e^{-i\hbar^{-1}(S_2+S_1)}}{i\hbar\sqrt{P_1P_2}} \\ \frac{\left(\frac{d}{dR}P_1\right)}{2P_1}e^{2iS_1} & 0 & -\frac{MV_{12}e^{i\hbar^{-1}(S_2+S_1)}}{i\hbar\sqrt{P_1P_2}} & -\frac{MV_{12}e^{-i\hbar^{-1}(S_2-S_1)}}{i\hbar\sqrt{P_1P_2}} \\ \frac{MV_{12}e^{-i\hbar^{-1}(S_2-S_1)}}{i\hbar\sqrt{P_1P_2}} & \frac{MV_{12}e^{-i\hbar^{-1}(S_2+S_1)}}{i\hbar\sqrt{P_1P_2}} & 0 & \frac{\left(\frac{d}{dR}P_2\right)}{2P_2}e^{-2iS_2} \\ -\frac{MV_{12}e^{i\hbar^{-1}(S_2+S_1)}}{i\hbar\sqrt{P_1P_2}} & -\frac{MV_{12}e^{i\hbar^{-1}(S_2-S_1)}}{i\hbar\sqrt{P_1P_2}} & \frac{\left(\frac{d}{dR}P_2\right)}{2P_2}e^{2iS_2} & 0 \end{pmatrix}\begin{pmatrix} b_{1+} \\ b_{1-} \\ b_{2+} \\ b_{2-} \end{pmatrix}$$

Equations IV-14, entirely equivalent to IV-11, are now reduced to two by making three approximations.

In the first of these approximations, the WKB, we neglect the b_{1+}, b_{1-} and b_{2+}, b_{2-} coupling. This assumes that the

terms

(IV-15)
$$\frac{\left(\frac{d}{dR} P_{1,2}\right)}{2 P_{1,2}} e^{\pm 2i S_{1,2}}$$

are small, and will be true if

$$[R] \frac{d}{dR} P_{1,2} \ll P_{1,2}$$

where $[R]$ is the unit length in particular system of units in which R and $P_{1,2}$ are expressed.

As before in Section IIIA, this means that the potential is slowly changing and the free particle wavelength is relatively small. Actually $\left(\frac{d}{dR} P_{1,2}\right)/2 P_{1,2}$ need not be small if it is fairly constant and $P_{1,2}$ is large; then the coupling term will be a rapidly oscillating quantity which averages to zero.

Second, the b_{1+}, b_{2-} and b_{2+}, b_{1-} coupling terms are ignored. Here it is assumed that the terms

(IV-16)
$$\pm \frac{M V_{12}}{i\hbar \sqrt{P_1 P_2}} e^{\pm \frac{i}{\hbar} (S_1 + S_2)}$$

are much less important than;

$$\pm \frac{M V_{12}}{i\hbar \sqrt{P_1 P_2}} e^{\pm \frac{i}{\hbar} (S_2 - S_1)}$$

This approximation necessitates the requirement that

$$| P_1 + P_2 | \gg | P_1 - P_2 |$$

and also that $V_{12}(R)$ be a slowly varying function. Delos[7] further shows that a second condition must hold for V_{12}, namely

$$V_{12} \ll \frac{P_1^2 + P_2^2}{2M}$$

If the three requirements stated above are fulfilled, then (IV-16) will be a rapidly oscillating term whose deviation from the approximation averages to zero.

While it is reasonable that the terms in (IV-15) and (IV-16) are unimportant in the classical region (i.e. for real momenta to the right of the turning point), it is clear that in the vicinity of $R_{T_{1,2}}$ neither is valid since $P_{1,2} = 0$. If the turning point is not too near the crossing point, R_c, then the coupling between the 1 and 2 states may be ignored in the non-classical region and a connection formula obtained (as was done in Section IIIA).

So, under the assumption that $R_{T_{1,2}}$ are not close to R_c equations IV-14 are reduced to:

$$(\text{IV-17}) \qquad i\hbar \frac{\sqrt{P_1 P_2}}{M} \frac{d}{dR} \begin{pmatrix} b_{1\pm} \\ b_{2\pm} \end{pmatrix} = \begin{pmatrix} 0 & \pm V_{12} e^{\pm i\hbar^{-1}(S_2 - S_1)} \\ \pm V_{12} e^{\mp i\hbar^{-1}(S_2 - S_1)} & 0 \end{pmatrix} \begin{pmatrix} b_{1\pm} \\ b_{2\pm} \end{pmatrix}$$

The JWKB boundary conditions give in this case:[7]

$$b_{1,2+}(R_T) = e^{-i\frac{\pi}{2}} b_{1,2-}(R_T)$$

where R_{T_1} is the larger of R_{T_1}, R_{T_2}. We now define a new variable, $\tau(R)$, with units of time, and let:

$$\tau(R_T) \equiv \tau_T$$

$$\frac{d\tau}{dR} = \frac{M}{\sqrt{P_1 P_2}} \qquad \text{for the } b_{1,2+} \text{ equations}$$

and

$$\frac{d\tau}{dR} = -\frac{M}{\sqrt{P_1 P_2}} \qquad \text{for the } b_{1,2-} \text{ equations}$$

With the further substitution:

$$C_{1,2}(\tau) = b_{1,2+}(\tau) \, e^{i\pi/2} \qquad \tau > \tau_T$$

$$C_{1,2}(\tau) = b_{1,2-}(\tau) \qquad \tau < \tau_T$$

We may write equation IV-17 as:

(IV-18)
$$i\hbar \frac{d}{d\tau}\begin{pmatrix} C_1(\tau) \\ C_2(\tau) \end{pmatrix} = \begin{pmatrix} 0 & V_{12}(\tau) e^{i\Delta} \\ V_{12}(\tau) e^{-i\Delta} & 0 \end{pmatrix} \begin{pmatrix} C_1(\tau) \\ C_2(\tau) \end{pmatrix}$$

with

$$\Delta = \pm \frac{i}{\hbar}\left[S_2(R(\tau)) - S_1(R(\tau)) \right] \qquad \text{for } \tau \gtrless \tau_T$$

Our problem is now to solve these two complex first order equations, called the classical equations. In the next steps we shall further reduce equation IV-18 to three real equations,

the solutions of which are directly related to the scattering amplitude.

Accordingly, we define the "evolution matrix" $G(\tau,\tau_T)$ as:

$$\begin{pmatrix} C_1(\tau) \\ C_2(\tau) \end{pmatrix} = G(\tau,\tau_T) \cdot \begin{pmatrix} C_1(\tau_T) \\ C_2(\tau_T) \end{pmatrix}$$

So that $G(\tau,\tau_T)$ satisfies:

(IV-19) $\qquad i\frac{d}{d\tau} G(\tau,\tau_T) = \begin{pmatrix} 0 & \hbar V_{12} e^{i\Delta} \\ \hbar V_{12} e^{-i\Delta} & 0 \end{pmatrix} G(\tau,\tau_T)$

with the boundary condition that

(IV-20) $\qquad G(\tau_T,\tau_T) = 1$

From the last two equations:[35] $GG^\dagger = 1$, $G = G^{-1}$ and $\det G = 1$. Consequently G may be parameterized as:

(IV-21) $\qquad G(\tau,\tau_T) = \begin{pmatrix} \sqrt{1-z^2}\, e^{i\Gamma_1} & -z\, e^{i\Gamma_2} \\ z\, e^{i\Gamma_2} & \sqrt{1-z^2}\, e^{-i\Gamma_1} \end{pmatrix}$

Equation IV-19 then shows that z, Γ_1, Γ_2 must solve the set:

$$\frac{dz}{d\tau} = -\hbar V_{12} \sqrt{1-z^2}\, \sin\left(\Delta + \Gamma_2 - \Gamma_1\right)$$

(IV-22) $\qquad \dfrac{d\Gamma_1}{d\tau} = -\hbar V_{12} \dfrac{z}{\sqrt{1-z^2}} \cos\left(\Delta + \Gamma_2 - \Gamma_1\right)$

$$\frac{d\Gamma_2}{d\tau} = -\hbar V_{12} \frac{\sqrt{1-z^2}}{z} \cos\left(\Delta + \Gamma_2 - \Gamma_1\right)$$

with the boundary conditions from equation IV-20:

$$Z(\tau_T, \tau_T) = 0$$

(IV-23)
$$\Gamma_1(\tau_T, \tau_T) = 0$$

$$\Gamma_2'(\tau_T, \tau_T) = \pm \pi$$

Using the definition of G as well as the property that:

$$G^*(-\tau, \tau_T) = G(\tau, \tau_T)$$

we find

(IV-24)
$$\begin{pmatrix} C_1(\tau) \\ C_2(\tau) \end{pmatrix} = e^{-i\frac{\pi}{2}} G(\tau, \tau_T) \tilde{G}(\tau, \tau_T) \begin{pmatrix} C_1(-\tau) \\ C_2(-\tau) \end{pmatrix}$$

This is an important result in that it shows equations IV-22 need only be integrated over one half their range. That is, the wavefunction can be specified in some state at $\tau = -\infty$ before the scattering and G, defined in equation IV-21, is then employed to find the wavefunction at $\tau = +\infty$ long after the interaction. To accomplish this, equation IV-24 tells us that the parameters Z, Γ_1, Γ_2' need be integrated over only the half space $\tau = \tau_T$ to $\tau = +\infty$. We define S as

(IV-25)
$$S = G(\tau, \tau_T) \tilde{G}(\tau, \tau_T)$$

and the S matrix element for channel 1 elastic scattering is S_{11}, given by:

$$\mathcal{F}_1(R) = (k_1)^{-\frac{1}{2}} e^{-i\left(k_1 R - \frac{\ell\pi}{2}\right)} - \mathcal{S}_{11}(k_1)^{-\frac{1}{2}} e^{i\left(k_1 R - \frac{\ell\pi}{2}\right)}$$

Recalling the expansion for $\mathcal{F}_1(R)$

$$\mathcal{F}_1(R) = (p_1)^{-\frac{1}{2}} b_{1-}(R(\tau)) e^{-iS_1\hbar^{-1}} + (p_1)^{-\frac{1}{2}} b_{1+}(R(\tau)) e^{iS_1\hbar^{-1}}$$

we identify

$$\lim_{R \to \infty} b_{1-}(R(\tau)) = \lim_{R \to \infty} \sqrt{\hbar} \; e^{i\left(S_1\hbar^{-1} - k_1 R + \frac{\ell\pi}{2}\right)}$$

and

$$\mathcal{S}_{11} = \lim_{R \to \infty} b_{1+}(R(\tau)) \frac{1}{\sqrt{\hbar}} e^{i\left(S_1\hbar^{-1} - k_1 R + \frac{\ell\pi}{2}\right)}$$

but from equation IV-24

$$C_1(\infty) = e^{i\frac{\pi}{2}} \mathcal{S}_{11} C_1(-\infty)$$

therefore

$$\lim_{R \to \infty} b_{1+}(R(\tau)) = e^{i\frac{\pi}{2}} \mathcal{S}_{11} \lim_{R \to \infty} b_{1-}(R(\tau))$$

So that

$$\mathcal{S}_{11} = e^{i\frac{\pi}{2}} \mathcal{S}_{11} \lim_{R \to \infty} e^{2i\left(S_1\hbar^{-1} - k_1 R + \frac{\ell\pi}{2}\right)}$$

Recalling the definition of S_1 in equation IV-12 and

η_{JWKBL} in equation III-12 we see that:

(IV-26) $$\mathcal{S}_{11} = S_{11} e^{2i\eta_1}$$

where η_1 , is the JWKBL phase shift corresponding to the diabatic potential $V_1(R)$.

We can now connect the solutions Z, Γ_1, Γ_2 of the classical equations with the scattering amplitude and write:

$$f(\theta) = \frac{1}{2ik_1} \sum_{\ell} (2\ell+1) P_\ell(\cos\theta) (\mathcal{S}_{11} - 1)$$

(IV-27) $$f(\theta) = \frac{1}{2ik_1} \sum_{\ell} (2\ell+1) P_\ell(\cos\theta) \left[Z^2 e^{2i(\eta_1 - \Gamma_2)} + (1-Z^2) e^{2i(\eta_1 + \Gamma_1)} \right]$$

Here, we have used equations IV-25 and IV-21 to evaluate S_{11}. The values of Z, Γ_1, Γ_2 used in equation IV-27 result from the integration of the set IV-22 from $\tau = \tau_T$ to $\tau = +\infty$ with the boundary conditions IV-23. The one problem remaining in this discussion is the solution of equations IV-22.

In order to deal with the phase Δ,

$$\Delta = \frac{1}{\hbar} \int_{\tau_T}^{\tau} \left[V_1(R(\tau)) - V_2(R(\tau)) \right] d\tau$$

Delos introduces two new unitless variables λ and s.[7]

(IV-28) $$s(\tau) = \frac{1}{\hbar} \int_0^{\tau} V_{12}(\tau) d\tau$$

$$\lambda = -\frac{(V_1 - V_2)}{2V_{12}}$$

Let us take γ to be zero at the crossing. Consequently,
at the turning point $\left(R_T < R_C \right)$:

$$s = s_T < 0$$

$$\ell = \ell_T = -\epsilon \quad \text{with} \quad \epsilon > 0$$

$$\frac{d\ell}{ds} \propto \frac{d\ell}{d\gamma} = \frac{d\ell}{dR}\frac{dR}{d\gamma}$$

but at $\quad R = R_T$, $\frac{dR}{d\gamma} = 0$ so

$$\left.\frac{d\ell}{ds}\right|_{s_T} = 0$$

at the crossing point;

$$s = 0, \quad \ell \propto V_1 - V_2 = 0$$

and as $\quad \gamma \to \infty$;

$$V_{12}\left(R(\gamma) \right) \to 0$$

$$\ell_\infty \to \infty$$

$$s_\infty = \int_0^\infty V_{12}\left(R(\gamma) \right) d\gamma \quad \text{and is finite since} \quad V_{12} \to 0$$
$$\text{as } R \to \infty$$

The function $\ell(s)$ is plotted as a solid line in figure 32.

Delos approximates the real $\ell(s)$ by the quadratic[7]

$$\ell(s) = \frac{1}{2}\left[\ell_1 s + \ell_2 \frac{s^2}{2} \right]$$

shown as a dashed line in figure 32.
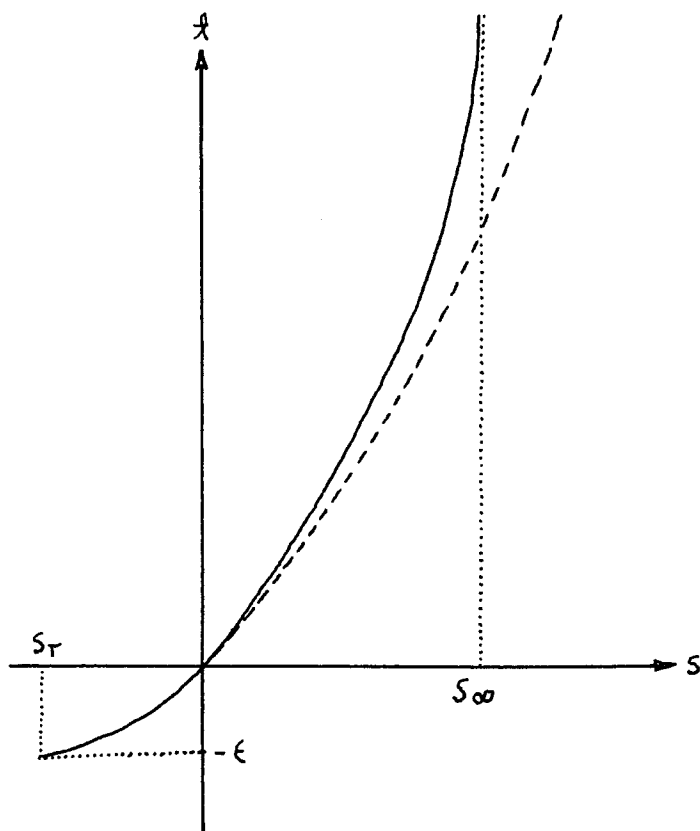
Figure 32: solid line - the function $\mathcal{f}(s)$; dashed line - the quadratic approximation of Delos.[7]

The parameters $\mathcal{f}_1$ and $\mathcal{f}_2$ are evaluated using the definitions IV-28 and explicit expansions for $V_{1,2}(R)$, $V_{12}(R)$ and $R(\tau)$ around the crossing point — namely:[36]

$$V_{1,2}(R) = -F_{1,2} \cdot R - F'_{1,2} \cdot \frac{R^2}{2}$$

$$V_{12}(R) = V_{12}(R_c) - \oint \cdot R$$

$$R(\tau) = v \cdot \tau + \frac{F}{M} \frac{\tau^2}{2}$$

with

$$F_{1,2} \equiv \frac{d}{dR} V_{1,2}(R) \Big|_{R=R_c}$$

$$F'_{1,2} \equiv \frac{d^2}{dR^2} V_{1,2}(R) \Big|_{R=R_c}$$

$$\mathfrak{f} \equiv \frac{d}{dR} V_{12}(R) \Big|_{R=R_c}$$

$$\nu \equiv \frac{dR}{d\tau} \Big|_{\tau=0}$$

where F is an average force which acts on the system at $R=R_c$
This gives for $\mathcal{t}_1$ and $\mathcal{t}_2$

$$\mathcal{t}_1 = \hbar \nu \left(\frac{F_1 - F_2}{V_{12}^2} \right)$$

(IV-29)

$$\mathcal{t}_2 = \hbar^2 \left(\frac{F_1 - F_2}{M V_{12}^3} \right) \cdot \left[F + 2E \left(\frac{F'_1 - F'_2}{F_1 - F_2} \right) + 2E \left(\frac{3\mathfrak{f}}{V_{12}} \right) \right]$$

Using these results, defining,

(IV-30) $b = \dfrac{4}{\sqrt{\mathcal{t}_2}}$ and $\epsilon = \dfrac{\mathcal{t}_1^2}{4 \mathcal{t}_2}$

and noticing that,

$$ds = \frac{b}{4} \frac{1}{\sqrt{\epsilon + \mathcal{t}}} d\mathcal{t}$$

we may rewrite equations IV-22

$$\frac{dz}{dt} = -H \sqrt{1-z^2} \, \sin\left(\Delta + \Gamma_2 - \Gamma_1\right)$$

(IV-31)

$$\frac{d\Gamma_1}{dt} = -H \frac{z}{\sqrt{1-z^2}} \, \cos\left(\Delta + \Gamma_2 - \Gamma_1\right)$$

$$\frac{d\Gamma_2}{dt} = -H \frac{\sqrt{1-z^2}}{z} \, \cos\left(\Delta + \Gamma_2 - \Gamma_1\right)$$

with

$$H = \frac{b}{4\sqrt{\epsilon + t}}$$

$$\Delta = -\frac{b}{2} \int_{-\epsilon}^{t} \frac{t \, dt}{\sqrt{\epsilon + t}}$$

and the boundary conditions:

$$z(-\epsilon, -\epsilon) = 0$$

$$\Gamma_1(-\epsilon, -\epsilon) = 0$$

$$\Gamma_2(-\epsilon, -\epsilon) = \pi$$

These boundary conditions present some difficulty in the numerical solution of equations IV-31 (see for example the third equation in the set). No such difficulties, however, exist in the result of the adaibatic configuration space treatment which we have touched on previously.

Here, expansion of $F_{1,2}(R)$ in terms containing, as arguments, action integrals over adiabatic momenta results in

the classical equations:

$$(IV-32) \quad \frac{d}{dt}\begin{pmatrix} c_1 \\ c_2 \end{pmatrix} = \begin{pmatrix} 0 & \frac{1}{2(1+\lambda^2)}e^{i\Delta} \\ -\frac{1}{2(1+\lambda^2)}e^{-i\Delta} & 0 \end{pmatrix}\begin{pmatrix} c_1 \\ c_2 \end{pmatrix}$$

with

$$(IV-33) \quad \Delta = \frac{1}{\hbar}\int_{R_\tau}^{R} \left(\pi_2(R) - \pi_1(R)\right) dR$$

where $\pi_{1,2}$ are the adiabatic momenta given by the plus and minus roots of the equation:

$$(IV-34) \quad \pi_{1,2} = \left\{ 2M\left[\frac{(E+V_1)+(E+V_2)}{2} \right.\right.$$
$$\left.\left. \pm \sqrt{\left(\frac{(E+V_1)-(E+V_2)}{2}\right)^2 + V_{12}^2} \right]\right\}^{1/2}$$

Equations IV-32 may be brought into the form of equations IV-18, by multiplying both sides by $i = e^{i\frac{\pi}{2}}$.

This being done, we may proceed as before and write

$$(IV-35) \quad \begin{aligned} \frac{dz}{dt} &= -\frac{1}{2(1+\lambda^2)}\sqrt{1-z^2}\cos\left(\Delta + \Gamma_2 - \Gamma_1\right) \\ \frac{d\Gamma_1}{dt} &= \frac{1}{2(1+\lambda^2)}\frac{z}{\sqrt{1-z^2}}\sin\left(\Delta + \Gamma_2 - \Gamma_1\right) \\ \frac{d\Gamma_2}{dt} &= \frac{1}{2(1+\lambda^2)}\frac{\sqrt{1-z^2}}{z}\sin\left(\Delta + \Gamma_2 - \Gamma_1\right) \end{aligned}$$

Where, it is noted, how the extra phase $\frac{\pi}{2}$ has been absorbed in the trigonometric functions.

These equations are to be integrated from $\xi = -\epsilon$ to $\xi = +\infty$ In practice the solutions converge to their limits[37]at $\xi \sim +20$ thus rendering the numerical problem possible and making the parabolic approximation to $\xi(s)$ reasonable.

The phase Δ in equations IV-35 must be written in terms of ξ . From the definition of the adiabatic momenta in equation IV-34 we find:

$$\pi_2^2 - \pi_1^2 = -4 M V_{12} \sqrt{1-\xi^2}$$

and letting

$$M \frac{dR}{d\tau} = \frac{\pi_1 + \pi_2}{2}$$

we have

$$dR = \frac{dR}{d\tau} \frac{d\tau}{ds} \frac{ds}{d\xi} d\xi$$

$$dR = \left[\frac{1}{M}\left(\frac{\pi_1+\pi_2}{2} \right) \right] \cdot \left[\frac{\hbar}{V_{12}} \right] \cdot \left[\frac{b}{4\sqrt{\epsilon+\xi}} \right] d\xi$$

and from equation IV-33 :

$$(\text{IV-36}) \qquad \Delta = -\frac{b}{2} \int_{-\epsilon}^{\xi} \frac{\sqrt{1+\xi^2}}{\sqrt{\epsilon+\xi}} \, d\xi$$

Here, the boundary conditions are no problem since

$$\frac{d\Gamma_2}{dA} = 0$$

at the boundary.

Equation IV-27 can then be employed to find $f(\theta)$; the one change being that η_1 now corresponds to an action integral over the π momenta, that is to say η_1 in equation IV-27 is now the adiabatic phase shift function.

Delos' adiabatic momentum space treatment[7] shows the validity[38] of equations IV-35 and IV-36 for the classical turning point close to the crossing; the adiabatic configuration space treatment just presented is valid elsewhere. Consequently equations IV-35 and IV-36 should be correct and useful for all classically allowed regions of space.

Let us conclude this section with a summary of the current results which we shall presently use to solve the low energy $(NeHe)^+$ curve crossing problem.

The diatomic system $(NeHe)^+$ is initially prepared in the state 1 (He^+ and Ne both in their ground states at $R=\infty$ long before the interaction). The scattering occurs; and at some small internuclear separation the adiabatic potentials for state 1 and for state 2 (asymptotically $He^+ + Ne^*$) become quite close together. The elastic scattering amplitude for state 1 may be computed from:

$$\text{(IV-27)} \quad f(\theta) = \frac{1}{2ik} \sum_{\ell} (2\ell+1) P_\ell(\cos\theta) \left[z^2 e^{2i(\eta_a - \Gamma_2)} + (1-z^2) e^{2i(\eta_a + \Gamma_1)} - 1 \right]$$

Here η_a is the JWKBL phase shift function resulting from the adiabatic potential for channel 1. The values of the functions z, Γ_1, Γ_2 (which also must be computed for each ℓ in the sum) are the solutions to the three coupled first order equations:

$$\frac{dz}{d\ell} = -\frac{1}{2(1+\ell^2)} \sqrt{1-z^2} \; \cos\left(\Delta + \Gamma_2 - \Gamma_1\right)$$

$$\text{(IV-35)} \quad \frac{d\Gamma_1}{d\ell} = \frac{1}{2(1+\ell^2)} \frac{z}{\sqrt{1-z^2}} \; \sin\left(\Delta + \Gamma_2 - \Gamma_1\right)$$

$$\frac{d\Gamma_2}{d\ell} = \frac{1}{2(1+\ell^2)} \frac{\sqrt{1-z^2}}{z} \; \sin\left(\Delta + \Gamma_2 - \Gamma_1\right)$$

with

$$\text{(IV-36)} \quad \Delta = -\frac{b}{2} \int_{-\epsilon}^{\ell} \frac{\sqrt{1+\ell^2}}{\sqrt{\epsilon+\ell}} \; d\ell$$

These equations are numerically integrated from $\ell = -\epsilon$ with the boundary conditions,

$$z(-\epsilon, -\epsilon) = 0$$

$$\Gamma_1(-\epsilon, -\epsilon) = 0$$

$$\Gamma_2(-\epsilon, -\epsilon) = -\pi$$

to $\ell = +\infty$. In actual practice the integration is truncated when Z, Γ_1 and Γ_2 have converged[37] which is usually at $\ell \sim +20$ The values of the parameters ϵ, b (which are different for each value of ℓ) have resulted, in this case, from further specializing the Delos approximations to linear potentials $V_{1,2}$ and constant interaction element V_{12}

$$\epsilon = \frac{\ell_1^2}{4\ell_2} \quad , \quad b = \frac{4}{\sqrt{\ell_2}}$$

$$\ell_2 = \hbar^2 \left[\frac{\frac{dV_1}{dR}\Big|_{R_c} - \frac{dV_2}{dR}\Big|_{R_c}}{M V_{12}^3(R_c)} \right] \cdot F(R_c)$$

(IV-30)

$$\ell_1 = \hbar \, v(R_c) \left[\frac{\frac{dV_1}{dR}\Big|_{R_c} - \frac{dV_2}{dR}\Big|_{R_c}}{V_{12}^2(R_c)} \right]$$

$$v(R_c) = \sqrt{\frac{2}{M}\left[E - V(R_c) - \frac{\hbar^2(\ell+\frac{1}{2})^2}{2MR_c^2} \right]}$$

where $F(R_c)$ is an average force at the crossing. The values of the parameters $\left(R_c, \frac{d}{dR}V_{1,2}\Big|_{R_c}, V(R_c) = V_1(R_c) = V_2(R_c), \text{ and } V_{12}(R_c) \right)$ have been initially taken to be those calculated by Sidis in the quasi-diabatic representation.

At this point, the curve crossing problem should appear much more complex than the relatively straightforward one state theory of the previous chapter. In fact the present lack of parameterization of Z, Γ_1, Γ_2 does expand the numerical work

to a considerable extent. However plotting the quantities Z, $\alpha \frac{d\Gamma_1}{d\ell}$, and $\alpha \frac{d\Gamma_2}{d\ell}$ as functions of ℓ provides the needed insight into the scattering problem. This, we shall do and discuss in the next section.

IVC. Experimental Results for the
He⁺ + Ne Curve Crossing System

We believe that, in our series of experiments on the
(NeHe)⁺ system, we have isolated the effect of the lowest
energy crossing of the intermolecular curves.   In the 6eV
experiment, shown in figure 34c, no perturbation appears in
the differential cross section; and the scattering is such
as would result from a smooth repulsive potential.   In this
case, the energy is too low to sample the crossing (see
figure 33)
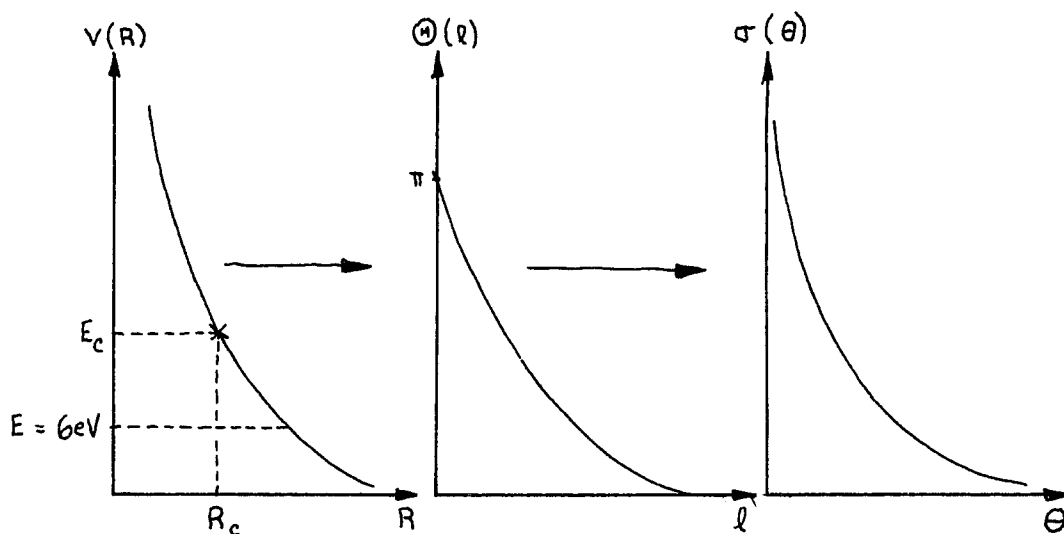
Figure 33:   the monotonic behavior of $\sigma(\theta)$ for the 6 eV
He⁺ + Ne scattering system.

At 30eV collison energy, however, the energy is some-
what greater than E_c and a perturbation is seen in the cross
section, shown in figure 34b, at large angle. Why the pertur-
bation should appear so far out is explained by figure 35.
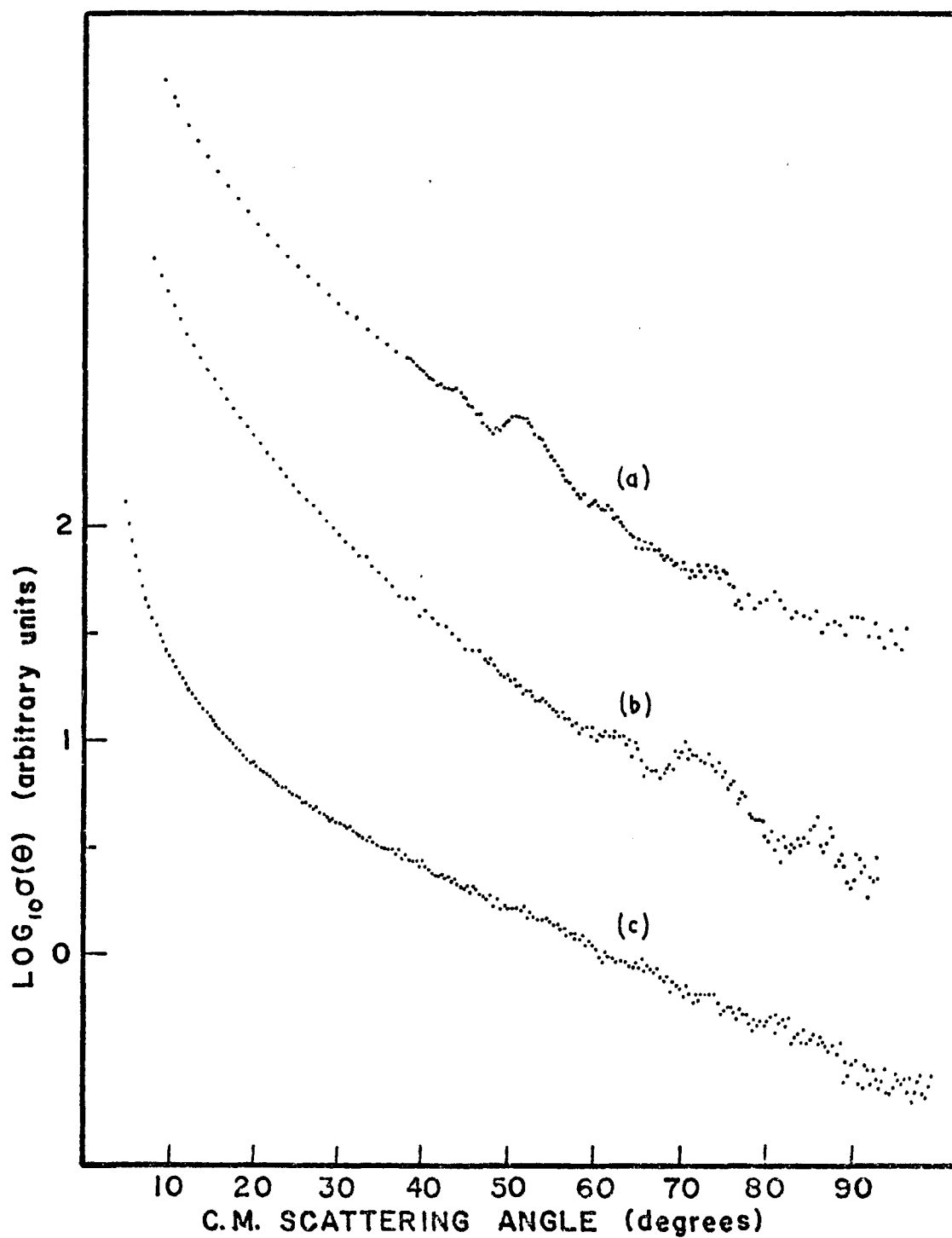
Figure 34: experimental differential elastic scattering cross sections for He^+ + Ne at; (a) 40eV, (b) 30eV, (c) 6eV.

At this low energy the impact parameter of the classical particle does not have to be very large before the turning point, R_T, is greater than R_c. Consequently at a small value of ℓ, ℓ becomes equal to ℓ_c corresponding to large Θ_c in the deflection function; and the JWKBL phase shifts[39] for a smooth repulsive potential will again provide a fairly accurate description of the scattering.
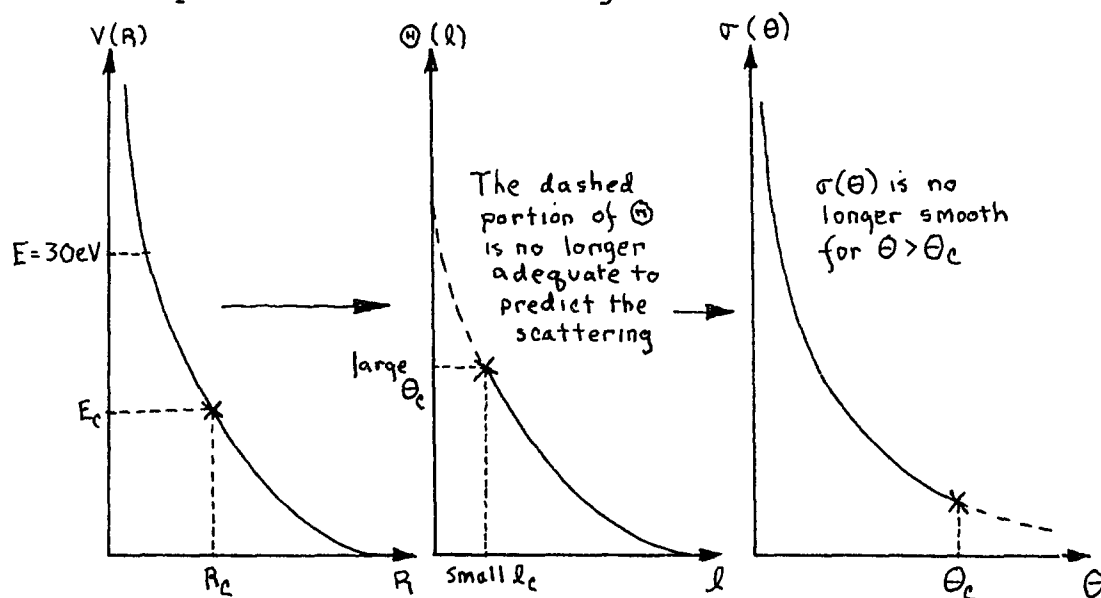
Figure 35: the onset of curve crossing perturbations in $\sigma(\theta)$ for the 30 eV He^+ + Ne scattering system.

As the collision energy is increased ℓ_c becomes larger and Θ_c smaller, until at 40eV the perturbation in the differential cross section, figure 34a, is nicely centered in the angular range of our equipment.

The simple discussion thus far is not really correct. In analogy to rainbow scattering,[40] the onset of the effects seen in the cross section occurs at a somewhat smaller angle

than Θ_c in figure 35. Since our insight into the quantitative aspects of the problem is considerably less developed than for rainbow scattering, an actual calculation was made.

An analytic function for the adiabatic curve was carefully constructed using the points of Sidis,[6] shown in figure 36, and his value for V_{12} ; the small value for the interaction term $\left(V_{12} = .26eV\right)$ necessitated a very sharp "knee" in the adiabatic potential. The functions $\mathcal{Z}(\ell)$, $\Gamma_1(\ell)$, $\Gamma_2(\ell)$ were found by numerical integration[41] of the set IV-35; and the partial wave sum of IV-27 was used to find the cross section.

The results showed, among other things, that the predicted perturbation was at too small an angle (about a 7° shift to the left). Using the type of reasoning with which we began this section, we shifted the crossing point up by 1.3eV. Further, a more simple function, which still closely approximated the Sidis points,[6] was used for the adiabatic curve. The explicit form used was:

$$\text{for } R < 1.86\, a_0 : \quad V_a(R) \ (\text{in } eV) = e^{-5.314487\,R\,+\,8.692006}$$
$$- e^{34.974496\,R\,-\,63.653678966\,+\,18.95}$$

$$\text{(IV-37)} \qquad \text{for } 1.86\, a_0 < R < 1.89\, a_0 : \quad V_a(R) = e^{-5.314487\,R\,+\,8.692006}$$
$$- e^{34.974496\,R\,-\,63.653678966\,+\,17.5} + 1.45\, e^{-\frac{(R-1.86)^2}{.0841}}$$

$$\text{for } R > 1.89\, a_0 : \quad V_a(R) = e^{-2.074\,R\,+\,6.745} + 1.45\, e^{-\frac{(R-1.86)^2}{.0841}}$$
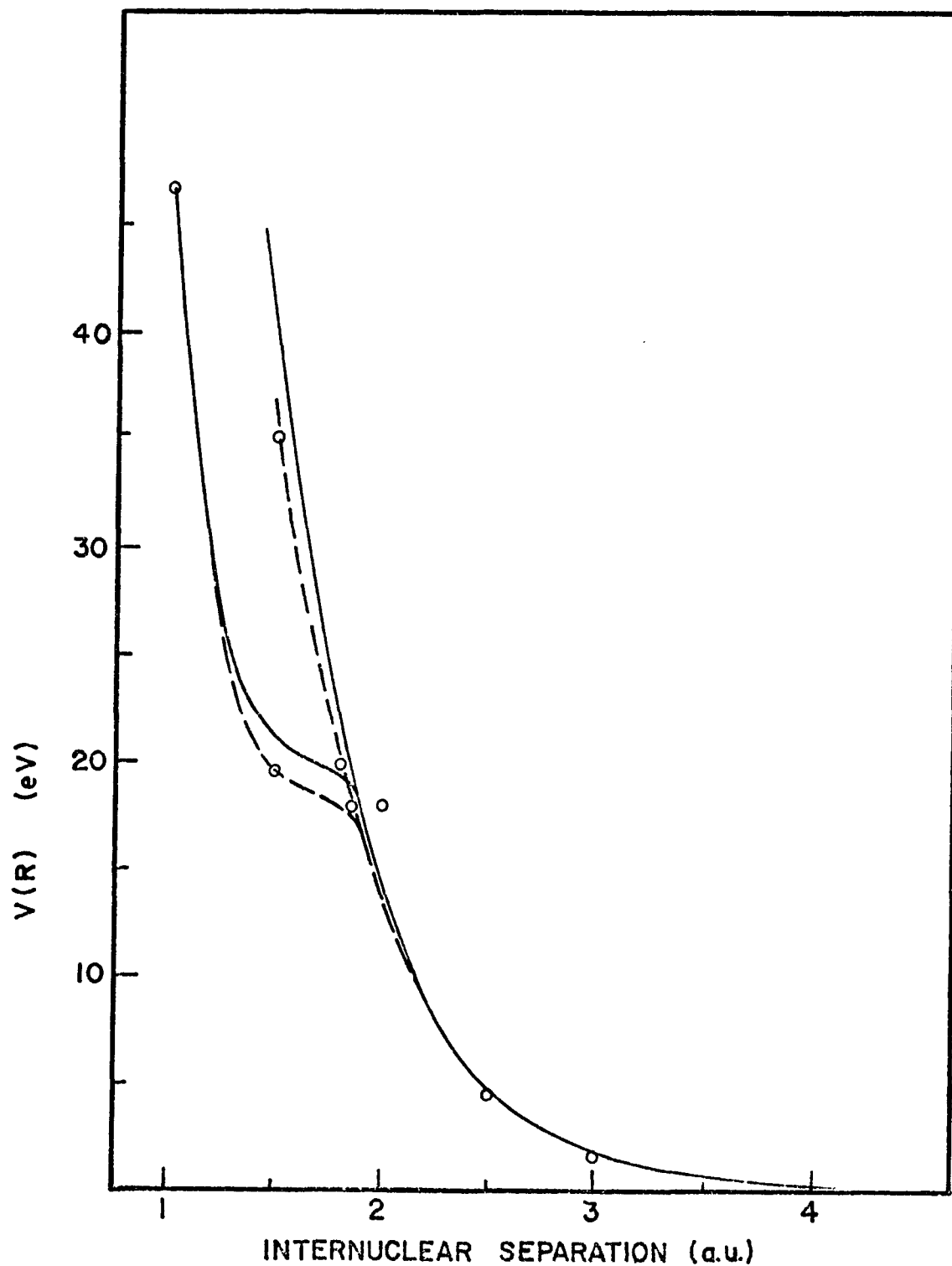
Figure 36: circles - result of the Sidis calculation, solid lines - analytic functions representing the adiabatic and diabatic curves corresponding to these circles, dashed lines - curves which were used to calculate the differential cross section in figure 37.

and is shown, along with the diabatic curve as dashed lines in figure 36. Using these potentials the parameters in IV-30 were found:

$$\frac{dV_1}{dR}\bigg|_{R_c} - \frac{dV_2}{dR}\bigg|_{R_c} = 35.0 \frac{eV}{a_0}$$

$$V_{12}(R_c) = .26 \, eV$$

(IV-38)
$$V(R_c) = E_c = 19.1 \, eV$$

$$R_c = 1.86 \, a_0$$

$$F(R_c) = 35.742 \frac{eV}{a_0}$$

The calculation for $\sigma(\theta)$ was again performed by using equations IV-35 and IV-27 with the result shown in figure 37. The perturbations in the theoretical prediction are seen to be in quantitative agreement with those resolved in the experiment (figure 37). Furthermore, the qualitative aspects of the experimental cross section (a smooth decrease before and fairly smooth, with very minor oscillations, after the crossing perturbation) are satisfactorily reflected by the calculation. The major difference between $\sigma_{Expt}(\theta)$ and $\sigma_{calc}(\theta)$ is the general rate of decay of the cross section with increasing angle.

We do not wish to belabor this disparity too strongly. Too many experimental factors[42] can affect the general decay

Figure 37: dashed line - calculated differential cross section, solid line - convolution of the calculated differential cross section, points - experimental data. All curves pertain to the 40eV He^+ + Ne elastic scattering.

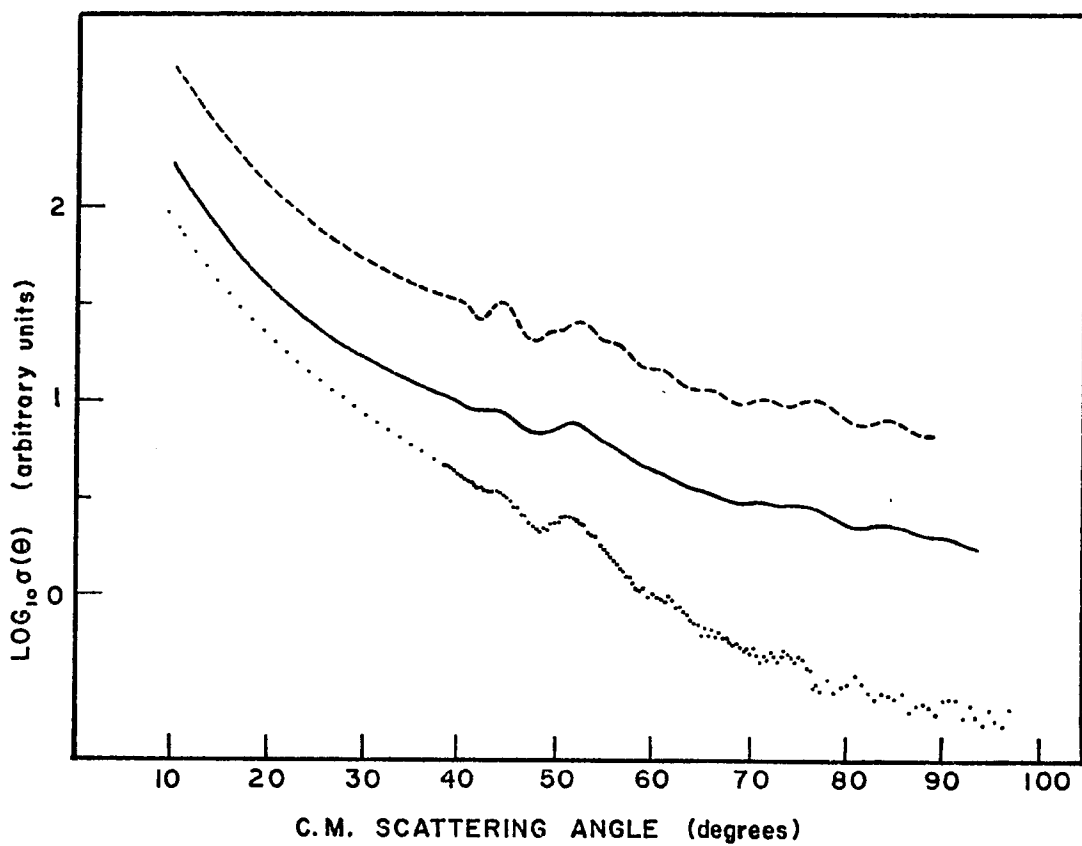rate (over ninety laboratory degrees and about three hours in time) for us to put a great deal of faith in this aspect of the data. On the other hand, we very strongly believe that the periodicties and locations of experimentally resolved oscillations are highly accurate.

We shall now discuss the origin of the observed scattering features in semiclassical terms. Our discussion shall be based on the two pseudo-deflection functions which shall be defined:

$$\Theta_1(\ell) \equiv 2\frac{d}{d\ell}\eta_1(\ell) \equiv 2\frac{d}{d\ell}\left(\eta_a(\ell) + \Gamma_1(\ell)\right)$$

(IV-39)
$$\Theta_2(\ell) \equiv 2\frac{d}{d\ell}\eta_2(\ell) \equiv 2\frac{d}{d\ell}\left(\eta_a(\ell) - \Gamma_2(\ell)\right)$$

which we have constructed by extending the equivalence relation to the partial wave sum

(IV-27)
$$f(\theta) = \frac{1}{2ik}\sum_{\ell}(2\ell+1)P_{\ell}(\cos\theta)\left[z^2 e^{2i(\eta_a - \Gamma_2)} + (1-z^2)e^{2i(\eta_a + \Gamma_1)}\right]$$

$\Theta_1(\ell)$ and $\Theta_2(\ell)$ have been plotted along with the adiabatic and diabatic deflection functions $\Theta_a(\ell)$ and $\Theta_d(\ell)$ in figure 38. Their shape may easily be inferred from the functions $\Gamma_1(\ell)$, $\Gamma_2(\ell)$ and $Z(\ell)$ which are shown in figure 39. $\Gamma_1(\ell)$ is essentially a step function around ℓ_c; this produces a negative going pulse in the deflection function which serves to decrease $\Theta_a(\ell)$ only in the region immediately to the left of ℓ_c. Delos[7] has noted that as ℓ becomes small

$$\Gamma_2(\ell) \longrightarrow \eta_a(\ell) - \eta_d(\ell) - \pi$$
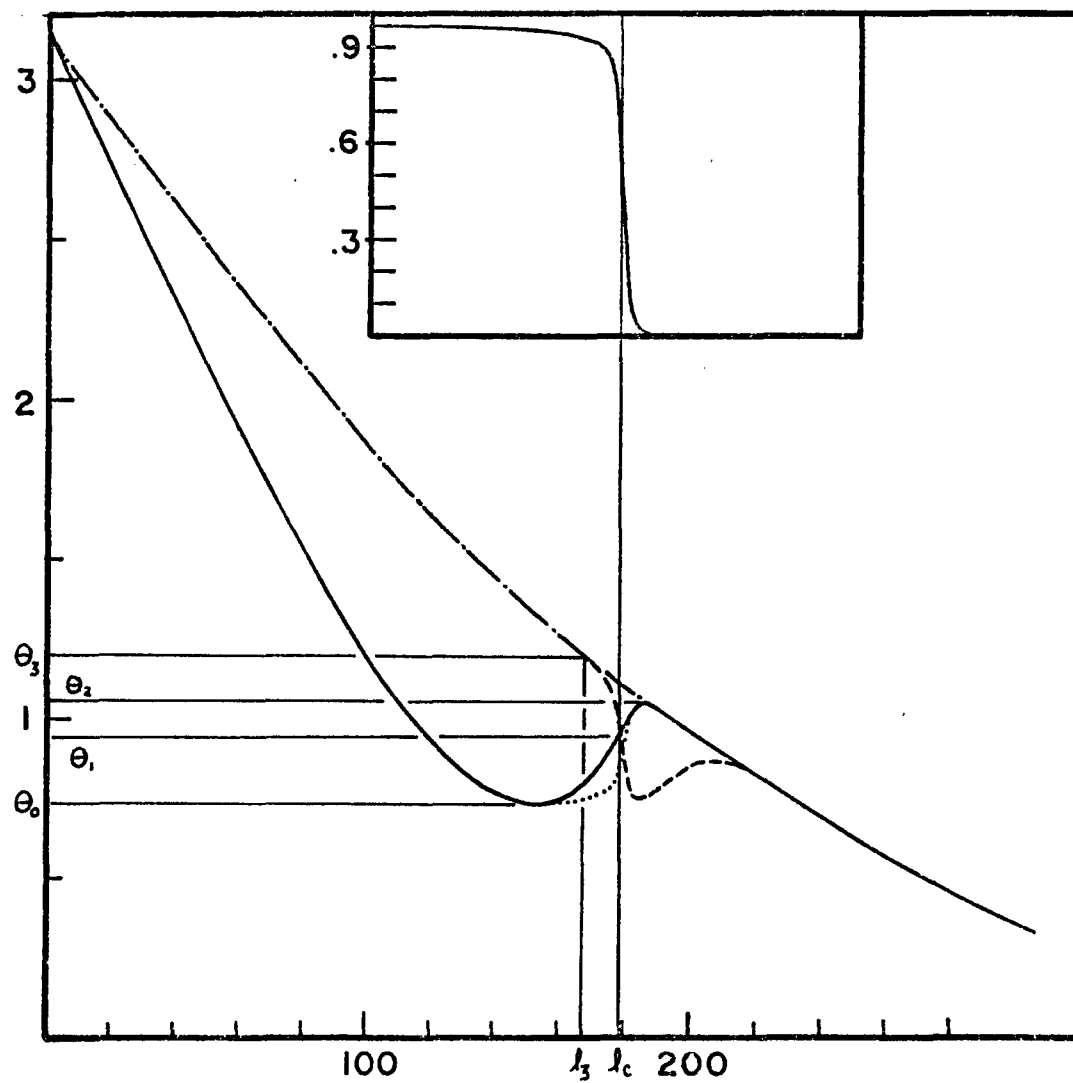
ANGULAR MOMENTUM QUANTUM NUMBER

Figure 38: inset - the function $Z^2(\ell)$; solid line - adiabatic deflection function Θ_a , chain line - diabatic deflection function Θ_d , dashed line - the pseudo deflection function Θ_2 , dotted line - the pseudo deflection function Θ_1
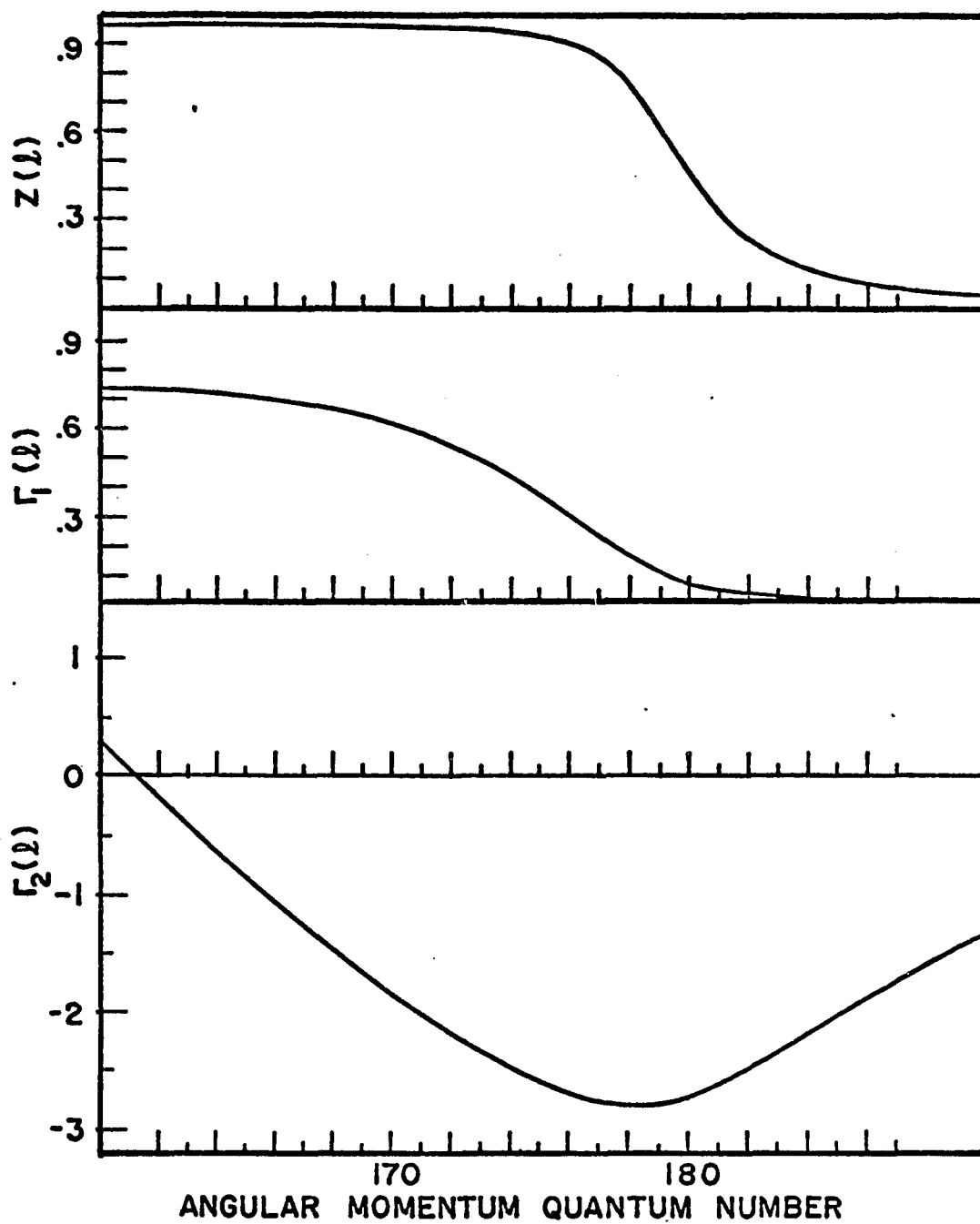
Figure 39 : the functions $Z(\ell), \Gamma_1(\ell), \Gamma_2(\ell)$

So that, to the right of ℓ_c,

$$\Theta_2(\ell) \longrightarrow \Theta_d(\ell)$$

The difference between $\Theta_2(\ell)$ and $\Theta_d(\ell)$ is the approximately wedge-shaped region of area 2π which has been removed from $\Theta_d(\ell)$ around ℓ_c. We also note that, since $\Gamma_2(\ell)$ has approximately zero slope at ℓ_c:

$$\Theta_2(\ell_c) \sim \Theta_a(\ell_c)$$

In our numerical procedures we have not solved the set IV-35 over the entire range of ℓ but only for values of ℓ around ℓ_c. For ℓ only a few units larger than ℓ_c, $Z(\ell)$ is almost zero and Z^2 is entirely negligible. Consequently for large ℓ, the adiabatic phase shifts are all that one needs to know. For ℓ about twenty units smaller than ℓ_c, $\Theta_2(\ell)$ has converged to $\Theta_d(\ell)$. So that for values of ℓ to the left of ℓ_3 in figure 38 we have explicitly used the diabatic path. In this same region we have analytically approximated $\Gamma_1(\ell)$, which makes negligible difference to the calculation since it has already saturated to its limit and makes no further contribution to $\Theta_1(\ell)$. For $Z(\ell)$ we have used the Landau-Zener formula[4]

(IV-40) $$Z^2(\ell) = e^{-2\pi \hbar^2 \left[\left(\frac{dV_1}{dR}\Big|_{R_c} - \frac{dV_2}{dR}\Big|_{R_c} \right) v(R_c, \ell) \right]^{-1} V_{12}^2}$$

which is an excellent approximation in this region. We have
made one further approximation to the work of Delos[7]in that
we have removed the ℓ dependence from $F(R_c)$ and evaluated
this average force for $\ell = \ell_c$.

Let us now examine the semiclassical prediction of $\Theta_1(\ell)$
and $\Theta_2(\ell)$ for the differential cross section; where, as before,
our references to angles and values of ℓ will be to figure 38
For $\theta > \theta_3$ there are two paths the system may follow, i.e.
$\Theta_1(\ell) = \Theta_a(\ell)$ and $\Theta_2(\ell) = \Theta_d(\ell)$. Since $Z(\ell)$ is almost unity
here we would expect $\Theta_d(\ell)$ to basically account for the
differential cross section in this region. Since $Z(\ell)$ is
not identically one, however, there should be some small
amplitude interference in $\sigma(\theta)$ for $\theta > \theta_3$. We can be more
explicit: since both $\Theta_1(\ell)$ and $\Theta_2(\ell)$ are smooth monatonic
functions we adapt equation III-19 to this situation and write

$$(\text{IV-41}) \qquad f(\theta) = Z^2 \sqrt{\sigma_{c_2}} \, e^{i A_2} + (1-Z^2) \sqrt{\sigma_{c_1}} \, e^{i A_1}$$

with

$$Z = .96$$

$$A_{1,2} = 2\eta_{1,2} - \theta \ell_{1,2} - \frac{\pi}{2}$$

$$\sigma_{c_{1,2}} = \frac{\ell_{1,2}}{k^2 \sin\theta \left| \frac{d\Theta}{d\ell} \right|_{\ell=\ell_{1,2}}}$$

So that

$$\sigma(\theta) = z^4 \sigma_{c_2} + (1-z^2)^2 \sigma_{c_1} + 2z^2(1-z^2)\sqrt{\sigma_{c_1}\sigma_{c_2}} \cos(A_1-A_2)$$

From figure 38 one can make the rough approximations

$$\theta_2 = \pi - \left(\frac{\pi-1.2}{170}\right)\ell_2 \longrightarrow \ell_2 = \frac{\theta-\pi}{1.2-\pi}170$$

$$\theta_1 = \pi - \left(\frac{\pi-1.2}{100}\right)\ell_1 \longrightarrow \ell_1 = \frac{\theta-\pi}{1.2-\pi}100$$

and ignore the term $(1-z^2)^2 \sigma_{c_1}$ which is very small; we find that

$$\sigma(\theta) = z^4 \sigma_{c_2}\left(1 + \frac{2(1-z^2)}{z^2}\sqrt{\frac{\sigma_{c_1}}{\sigma_{c_2}}}\cos\left(2(\eta_1-\eta_2)+\theta(\ell_2-\ell_1)\right)\right)$$

but

$$\frac{2(1-z^2)}{z^2}\sqrt{\frac{\sigma_{c_1}}{\sigma_{c_2}}} \sim .1$$

Consequently the cross section should oscillate with periodicity

(IV-42) $$\Delta\theta = \frac{2\pi}{\ell_2-\ell_1}$$

and amplitude of approximately one tenth the average intensity. Furthermore we have found (by measuring $\ell_2-\ell_1$) that formula IV-42 is essentially valid for all angles larger than θ_o;

and thus accounts for the high frequency component of the cross section in figure 37. Since only one classical trajectory $\Theta_1(\ell) = \Theta_a(\ell)$ exists for $\Theta < \Theta_0$ these oscillations are damped out in this region.

The large "rainbow-like" envelope (at 52°) in the cross section is essentially due to the negatively curved doubly-branched portion of $\Theta_1(\ell)$ immediately to the right of ℓ_c . Since $\Theta_1(\ell)$ possesses another doubly-branched portion to the left of ℓ_c this last assertion should be verified. In order to do so, we have added a large negative pulse to $\Theta_1(\ell)$ in the vicinity of its minimum and recalculated the cross section. The results are shown in figure 40. Since the rainbow structure has only moved about 2°, the small amount by which we changed the maximum of $\Theta_1(\ell)$, instead of the large amount by which we changed its minimum we believe that our initial assertion is correct. Also, since branch multiplicity has been extended below Θ_0, the high frequency oscillations appear at smaller angles.

The next few remarks are basically speculation on the part of the author. In addition to showing the source of the rainbow-like structure seen in the cross section, figure 40 may also indicate the source of the peculiar perturbation seen between 75° and 80° in figure 37. Our previous discussion of this angular region predicted only small regular oscillations resulting from the two smooth interfering
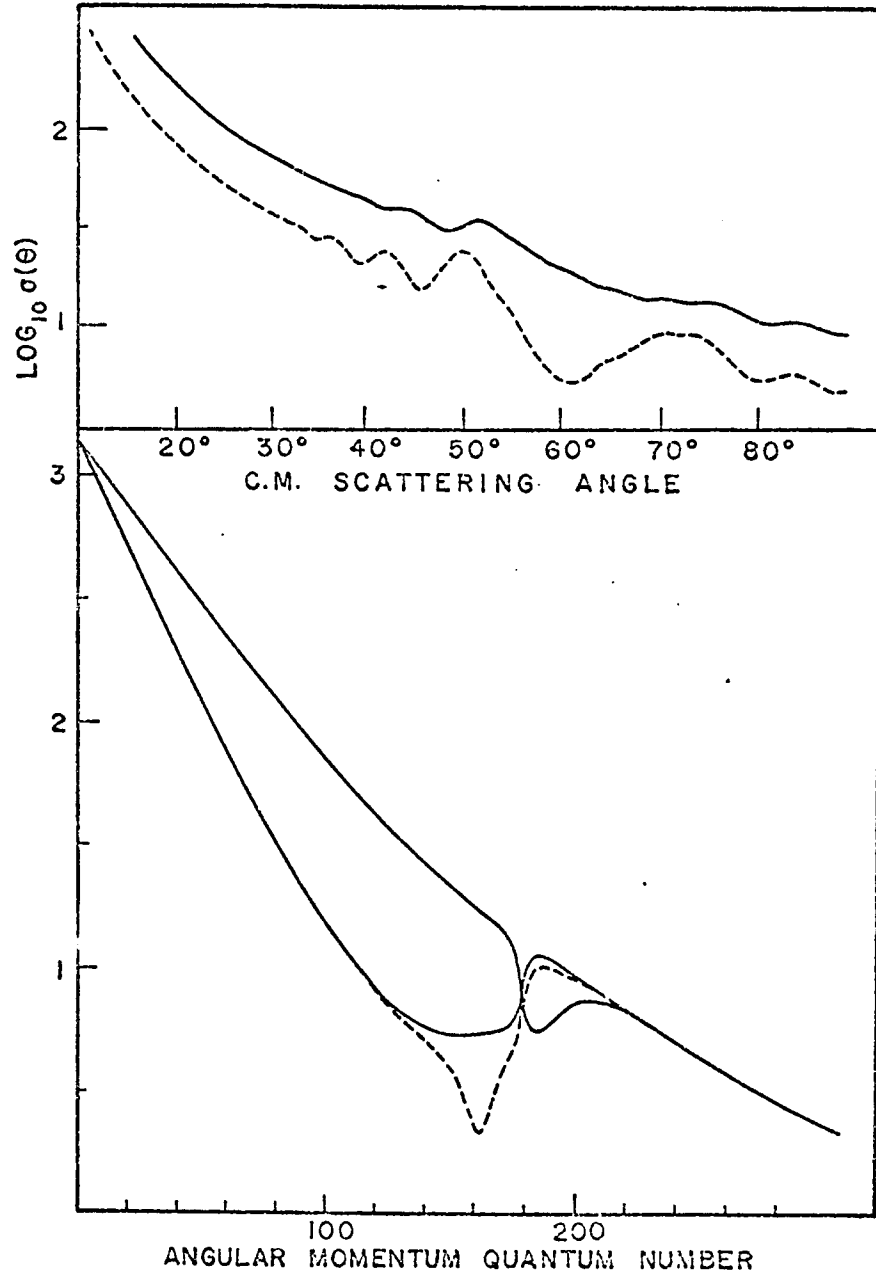
Figure 40: (bottom) solid lines – $\Theta_1(\ell)$
and $\Theta_2(\ell)$ from figure 38, dashed line
– the distortion introduced into Θ_1; (top)
solid line – convoluted differential cross
section corresponding to undistorted Θ_1
and Θ_2, dashed line – convoluted differen-
tial cross section where Θ_1 has been dis-
torted. Both relative cross sections have
been calculated for the 40 eV He$^+$ + Ne
elastic scattering system.

trajectories shown in figure 38. We believe: (1) that for $\Theta > \Theta_3$, it is reasonable to consider the scattering as resulting from an average deflection function, $\Theta_{av}(\ell)$, lying close to $\Theta_2(\ell)$ since z^2 is almost unity; and (2) that the angular momentum coupling between $\Theta_1(\ell)$ and $\Theta_2(\ell)$ leads to a distortion in $\Theta_{av}(\ell)$ for values of ℓ around the minimum of $\Theta_1(\ell)$, and that this distortion produces the irregular perturbation is the cross section at large angles. The deeper minimum introduced into $\Theta_1(\ell)$ in figure 40 augments the distortion in $\Theta_{av}(\ell)$ and therefore enhances the resulting perturbation in the calculated cross section. Since we cannot, as yet, mathematically define a single smooth average deflection function, we cannot prove what we have just presented but we believe that it is so anyway.

As a conclusion to this section we shall introduce two quantities, $A(\ell)$ and $\overline{\Theta}(\ell)$, and discuss a possible parameterization of the curve crossing problem which may facilitate the calculation of the differential cross section. If we write

$$\mathscr{S}_{11} = (1-z^2)\, e^{2i(\eta_a + \Gamma_1)} + z^2\, e^{2i(\eta_a - \Gamma_2)} \equiv A\, e^{2i\overline{\eta}}$$

we find the deflection function semiclassically equivalent to $\overline{\eta}$ is

$$\text{(IV-43)} \quad \overline{\Theta}(\ell) = \frac{1}{A^2(\ell)} \left\{ z^4 \Theta_2 + (1-z^2)^2 \Theta_1 - 2 z \frac{dz}{d\ell} \sin(2\Gamma_1 + 2\Gamma_2) \right.$$

$$\left. + z^2(1-z^2)(\Theta_1 + \Theta_2) \cos(2\Gamma_1 + 2\Gamma_2) \right\}$$

with

(IV-44) $A(\ell) = \sqrt{z^4 + (1-z^2)^2 + 2z^2(1-z^2)\cos(\Gamma_2 + \Gamma_1)}$

$\overline{\Theta}(\ell)$ and $A(\ell)$ have been determined in the 40eV He^+ + Ne case and are plotted in figure 41. The surprising result is that, for $\ell < \ell_c$, $\overline{\Theta}(\ell)$ oscillates around $\Theta_2(\ell)$. The periodicity of these oscillations is given by

(IV-45) $\cos\left[2\left(\Gamma_1(\ell) + \Gamma_2(\ell)\right) + constant\right]$

The oscillations in $A(\ell)$ also conform to IV-45 with a phase difference of π . In both cases the frequency approaches zero as ℓ becomes small since

$$\frac{d\Gamma_1}{d\ell} \to 0$$

$$\frac{d\Gamma_2}{d\ell} = \frac{d}{d\ell}(\eta_a - \eta_d) \to \frac{\pi}{2} - \frac{\pi}{2} = 0$$

For $\ell < \ell_c$ in the region where $\frac{dz}{d\ell}$ is small the lower envelope of the oscillations of $\overline{\Theta}(\ell)$ is

$$(1-z^2)\,\Theta_1(\ell) + z^2\,\Theta_2(\ell)$$

and neglecting $(1-z^2)^2$ the upper envelope is

$$z^2\Theta_2(\ell) - (1-z^2)\left[\Theta_1(\ell) + \Theta_2(\ell)\right]$$

It is clear that as $\Theta_1(\ell) \to \Theta_2(\ell)$ (i.e. as ℓ becomes small) the amplitude of the oscillations is strongly damped.
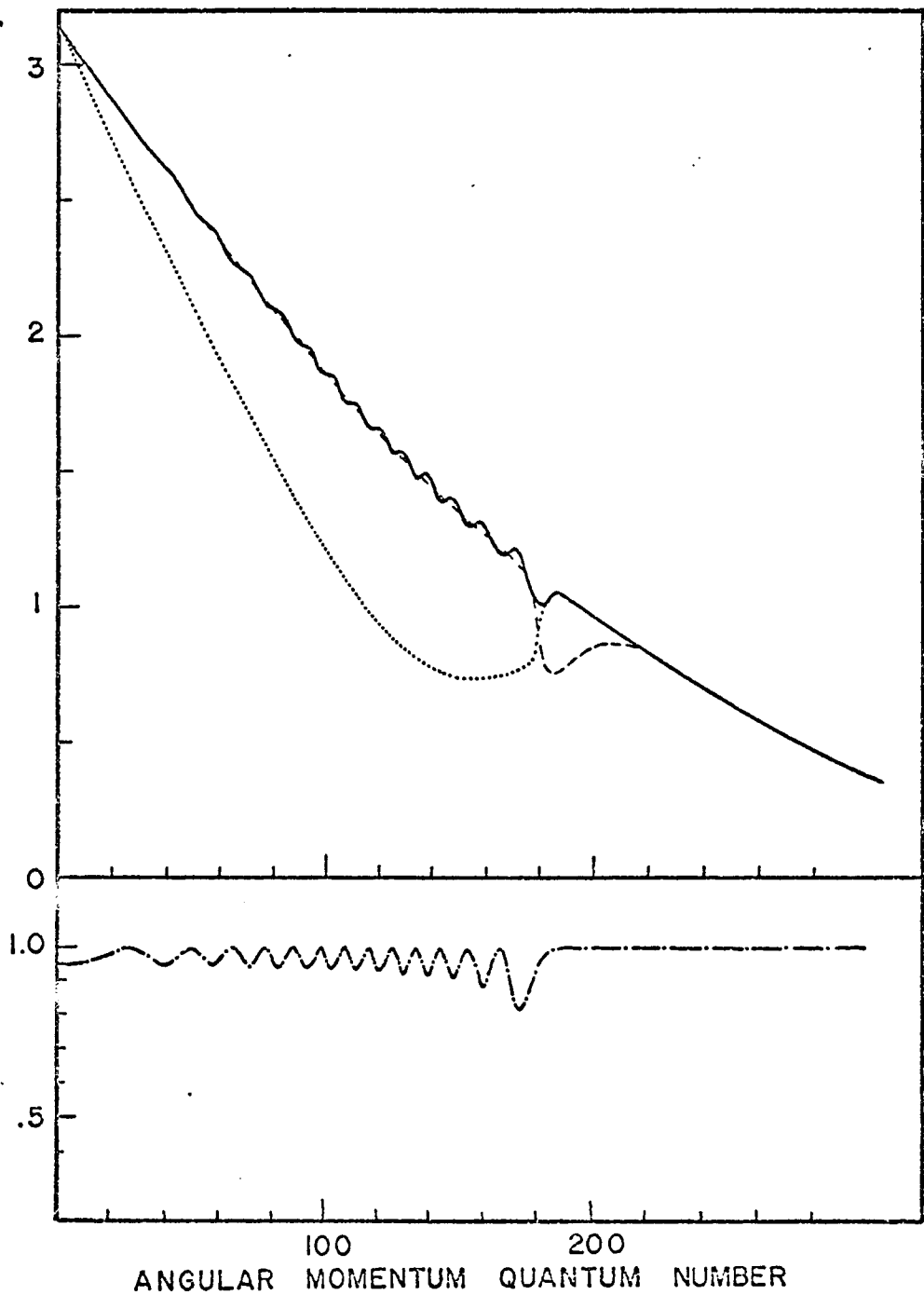
Figure 41: (bottom) chain line - $A(\ell)$; (top) dashed line - $\Theta_2(\ell)$, dotted line - $\Theta_1(\ell)$, solid line - $\overline{\Theta}(\ell)$.

The form of $\overline{\textcircled{H}}(\ell)$ suggests a parameterization in terms of the Remler-Regge method.[3] A set of pole configurations could be placed as shown in figure 42.
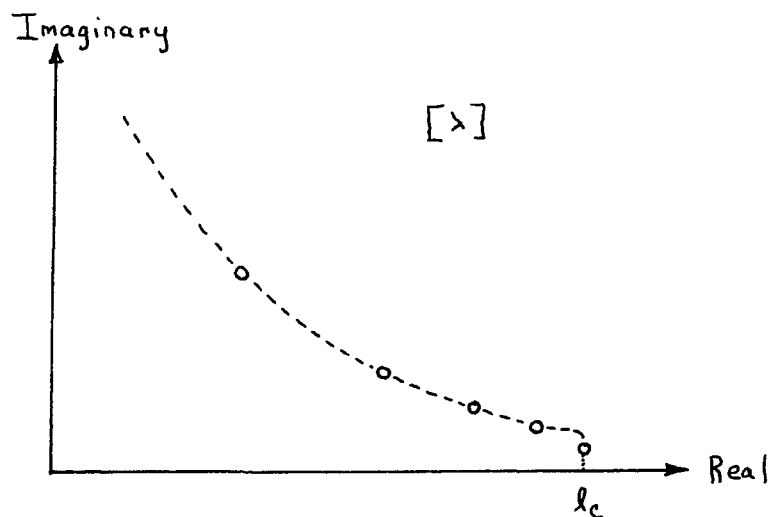
Figure 42: location of poles in the $[\lambda]$ plane which would reproduce oscillations of $\overline{\textcircled{\Theta}}(\ell)$ in figure 41.

The spacing between them is related to the local period of IV-45; while the constellations which have small real parts also have larger imaginary parts since the oscillations in the deflection function are damped as $\ell \to 0$. Additionally, to continue the phase shift and deflection functions to large ℓ, a circular array of poles could be positioned at $Re\,\lambda_p = \ell_c$ in the fourth quadrant of the $[\lambda]$ plane.[44] An analytic function $\Theta_c(\ell)$ which goes smoothly to zero at ℓ_c would continue $\overline{\textcircled{\Theta}}(\ell)$ to the point $(0,\pi)$ as shown in figure 43.

$\tilde{\Theta}(\ell)$ and contributions to it
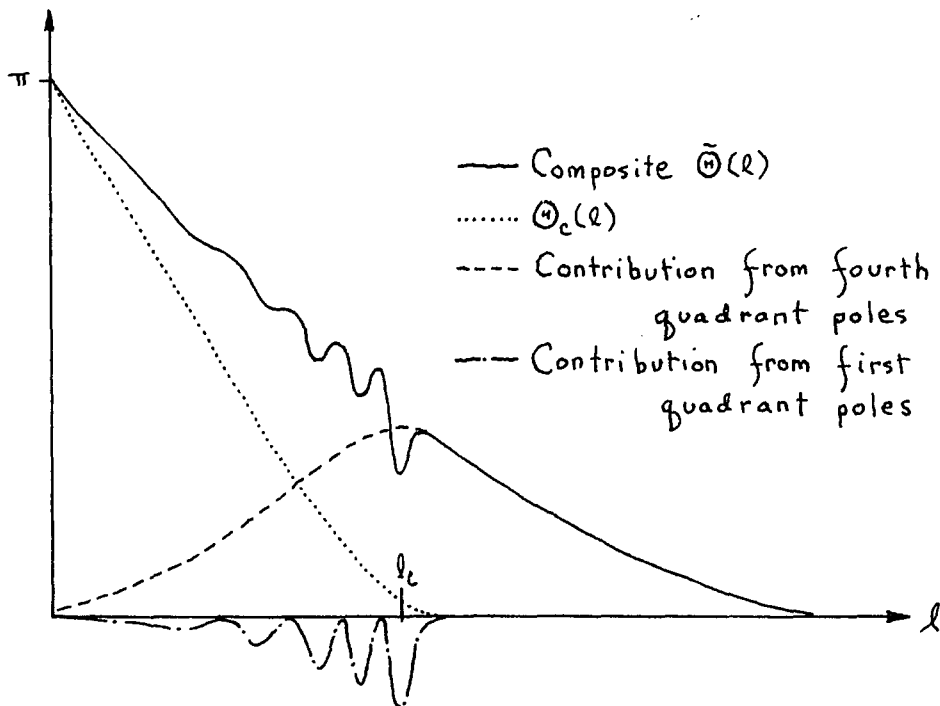
Figure 43: the composition of $\tilde{\Theta}(\ell)$ from pole and core contributions.

The parameterization of $A(\ell)$ is not so apparent. It may, as Remler[45] suggests, prove possible to modify the form of the singularities in the first quadrant such that the matrix elements no longer obey the unitarity condition. Then the resulting complex phase shifts are $\eta_A(\ell)$ which are adjusted so that:

$$\text{Im } \eta_A(\ell) = \log_e A(\ell)$$

Unfortunately, time prohibits our undertaking this task; and our last few comments should only be regarded as possibilities which may effect a quantitative treatment of more complicated systems where many crossings are seen.

V. CONCLUSION

Our conclusion for the one state elastic scattering systems is straightforward. The Remler-Regge and Vollmer methods allow the inversion of the intermolecular potential from well-resolved experimental data. Furthermore, through the semiclassical method, specifically the deflection function, the origin of the observed scattering features is well understood. In fact, the analysis and inversion techniques presented in Section III should be applicable to any spherically symmetric scattering system for which the JWKBL phase shifts are thought to be adequate.

In the more complicated curve crossing problem, presented in Section IV, semiclassical ideas again give insight into the scattering. Here, however, the deflection functions which we have constructed are rapidly changing when the classical turning point approaches the crossing; and therefore in certain angular regions the semiclassical method is not strictly applicable. In any case, the full partial wave prediction of the cross section based on the Sidis potentials and the Delos semiquantal method is in good agreement with our experimental result for the $(NeHe)^+$ system at 40eV collision energy. The major difference between calculated and experimental cross sections in this case is a discrepency between the overall decay rates of the two curves, the experimental result appearing to fall faster with increasing angle. A number of explanations for this disagreement suggest themselves. The potentials used in the calculation could well be too hard and more slowly rising

functions for $V_{1,2}(R)$ would improve the situation. The possibility of another curve crossing accounting for a further decrease in intensity at large scattering angles does exist. One would suspect, however, that if this were the case there should also appear oscillatory features in the differential cross section due to this second crossing; and, further, that these features should appear at large angles, well-separated from those already observed. Since we have not experimentally resolved such features and since the slope discrepency begins to be apparent as close-in as 35° we do not believe very strongly in this second possibiilty. As mentioned in Section IVD the overall experimental slope may itself be questionable. We will, therefore, turn briefly to the problem of experimental error.

Many experimental factors might lead to an apparent decrease in intensity at large angles. We mention in passing the possibility of the primary beam and the target gas pressure changing during the course of the experiment. Also, some discrepency may enter in our treatment of the experimental data. Specifically, if the primary beam were strongly focused in the vertical direction the reaction volume correction in Section IIB would not be accurate. Perhaps most important is the effect that a slightly improper setting of the product accelerating voltage (ΔE_3 in Section IIB) would have upon the intensity. Uncertainties in this setting could result from an incorrect estimation of the scattering angle ($\pm 2/3^{\circ}$ at large angle) and from angular shifts or, worse, energy shifts of the primary beam during the experiment. For the higher energy beams with narrow energy profiles where the C. M. and laboratory systems are quite different this effect could be profound. Thus, rough estimation (using the formula for ΔE_3 in Section IIB) of the effect of percentage uncertainties in ΔE_3

upon the scattered intensity indicates the effect to be about sixty times larger for the 40eV $(NeHe)^+$ system than for the 5eV $(ArH)^+$ system at large scattering angles.

At this point it is appropriate to make two speculative comments concerning the curve crossing problem. In Section IV we have seen indications that a single "average" deflection function would be a useful concept in describing the differential cross section. We have attempted to define this function but the result was oscillatory over a large range of ℓ . Therefore our particular result for cannot be considered to be a reasonable basis for a semiclassical interpretation of the problem. It could however, in connection with the Remler-Regge method, be most useful for the numerical calculation of the differential cross section.

Appendix A: Classical Orbiting

We have already introduced V_{eff} as the potential which describes the radial motion of a classical particle, we had

$$V_{eff}(R) \equiv V(R) + \frac{L^2}{2MR^2}$$

Let us sketch a family of such curves for a realistic $V(R)$
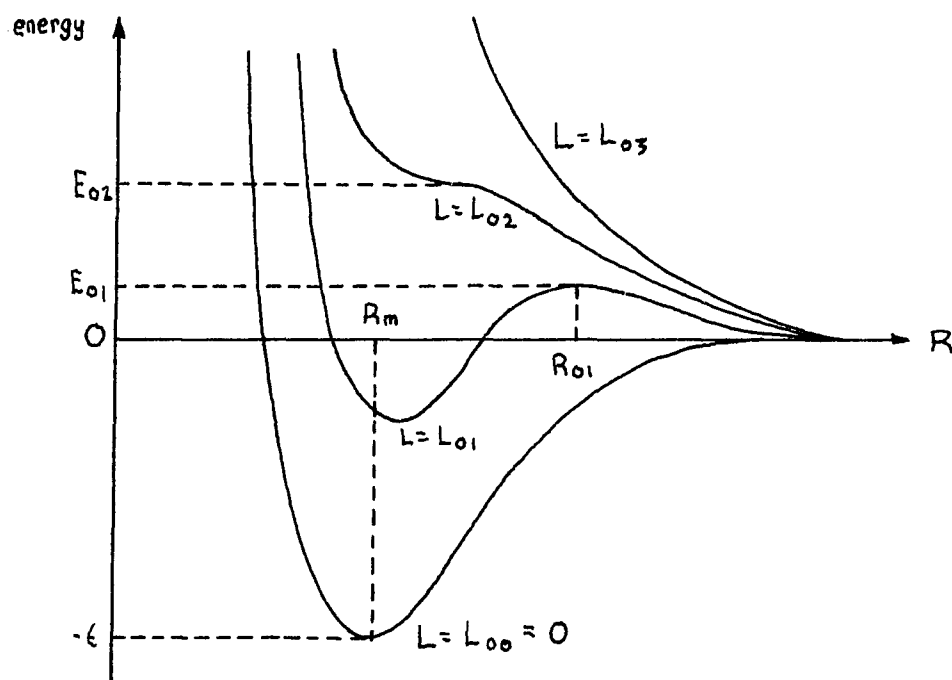
Figure 44: a family of effective potentials showing centrifugal effects.

If a classical particle with impact parameter corresponding to L_{o1} is incident on a scattering center with energy E_{o1} no radial force acts on it at the turning point R_{o1} and consequently it stays at this radius forever. In this case $\Theta(L)$ possesses a pole at $L = L_{o1}$ and an infinite number of branches contribute to the scattering (shown in

figure 45).
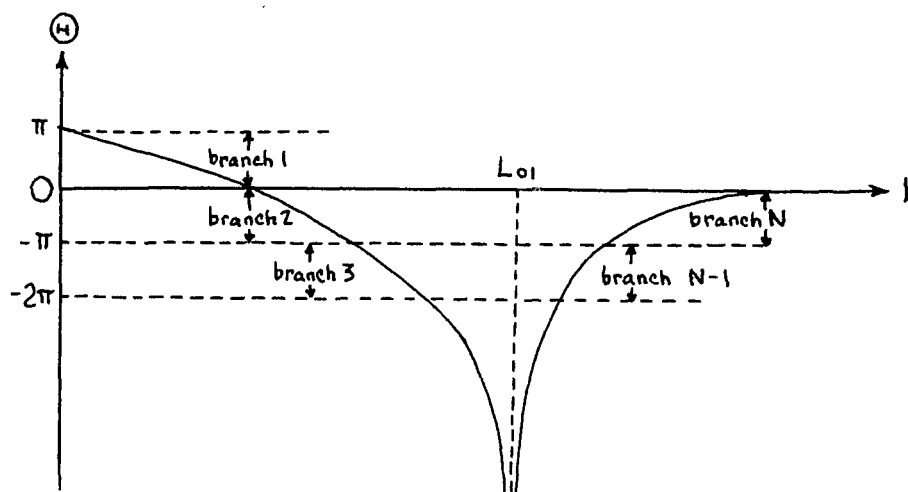
Figure 45: $\Theta(L)$ for classical orbiting.

The conditions for classical orbiting are

$$(A1) \qquad V_{eff}\Big|_{R_T} = E \quad , \quad \frac{d V_{eff}}{dR}\Big|_{R_T} = 0 \quad , \quad \frac{d^2 V_{eff}}{dR^2} \leq 0 \quad \text{where the equals sign corresponds to } E_{02}$$

We have graphically determined that for the inverted $(ArH)^+$ potential in figure 23 E_{02} is 1.1eV. Since classical orbiting cannot occur for incident beam energies which are above E_{02} we are justified in neglecting this phenomena in our analyses in Section III.

Appendix B: A Discussion of the Circular Pole Configuration

In Appendix B we will repeat an argument[45] which demonstrates
the lack of dependence of $\textcircled{H}_p$ (and hence of $\sigma(\theta)$)
upon ρ . We have

$$(B1) \qquad \textcircled{H}_p = -\sum_{p=1}^{N} \frac{4\lambda\, Im\, \lambda_p^2}{|\lambda^2 - \lambda_p^2|^2} = -2\lambda \left(\sum_p \frac{1}{\lambda^2 - \lambda_p^2} - \sum_p \frac{1}{\lambda^2 - \lambda_p^{*2}} \right)$$

where λ is the real angular momentum $\ell + \frac{1}{2}$. We shall work
out the first $\left(\sum_p \frac{1}{\lambda^2 - \lambda_p^2} \right)$ term above. Consider figure 46
where N poles are positioned on a circle of radius ρ .
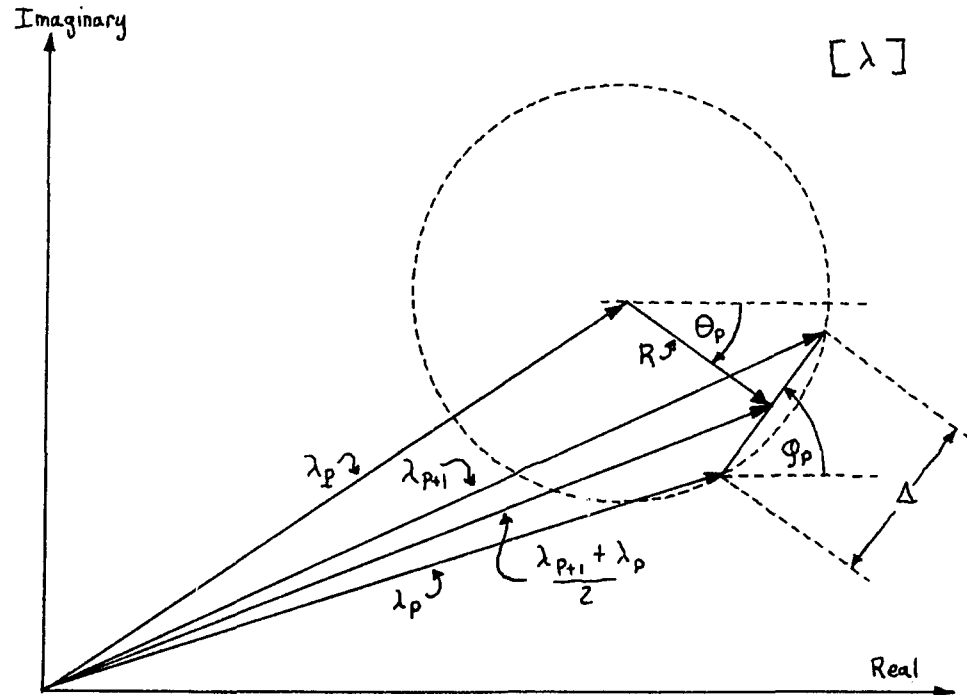
Figure 46: geometry of the pole configuration in the $[\lambda]$ plane.

So that

(B2) $$\lambda_{P+1} - \lambda_P = \Delta e^{i \varphi_P}$$

and

(B3) $$R = \frac{\lambda_{P+1} + \lambda_P}{2} - \lambda_P \equiv \rho e^{i \Theta_P}.$$

If Δ is small

$$\rho \approx |R|$$

Here

$$\Theta_P = -\frac{\pi}{2} + \varphi_P$$

Now let

$$\sum_P \frac{1}{\lambda^2 - \lambda_P^2} = \int_0^{2\pi\rho} \frac{dS}{\Delta} \frac{1}{\lambda^2 - \lambda_P^2}$$

where dS is the real differential displacement along the circumference of the circle in figure 46. This is valid when $1/(\lambda^2 - \lambda_P^2)$ is a slowly varying function between poles (in other words for a relatively large number of poles). So using

$$dS = d\lambda_P e^{-i\varphi_P}$$

we have

$$\sum_P \frac{1}{\lambda^2 - \lambda_P^2} = \oint_{\substack{\text{circle of} \\ \text{poles, } C}} \frac{d\lambda_P e^{-i\varphi_P}}{\Delta} \frac{1}{\lambda^2 - \lambda_P^2}$$

But from equation B1 and B2

$$e^{-i\varphi_P} = \rho \left(\frac{\lambda_{P+1} + \lambda_P}{2} - \lambda_{\underline{P}} \right)^{-1} e^{-i\frac{\pi}{2}} \sim -i\rho \frac{1}{\lambda_P - \lambda_{\underline{P}}}$$

So

$$\sum_P \frac{1}{\lambda^2 - \lambda_P^2} = \oint_C \frac{d\lambda_P}{\Delta} (-i\rho) \left(\frac{1}{\lambda_P - \lambda_{\underline{P}}} \right) \left(\frac{1}{\lambda^2 - \lambda_P^2} \right)$$

However if all the poles are off the axis, λ never equals λ_P and the only singularity contained within the contour is $\lambda_P = \lambda_{\underline{P}}$, therefore

$$\sum_P \frac{1}{\lambda^2 - \lambda_P^2} = 2\pi i \left[-\frac{i\rho}{\Delta} \frac{1}{\lambda^2 - \lambda_{\underline{P}}^2} \right] = \frac{2\pi\rho}{\Delta} \frac{1}{\lambda^2 - \lambda_{\underline{P}}^2} = \frac{N}{\lambda^2 - \lambda_{\underline{P}}^2}$$

The same argument could be applied to the second term of equation B1 with the final result:

$$\textcircled{H}_{\underline{P}} = -2\lambda N \left(\frac{1}{\lambda^2 - \lambda_{\underline{P}}^2} - \frac{1}{\lambda^2 - \lambda_{\underline{P}}^{*2}} \right)$$

$$\textcircled{H}_{\underline{P}} = N \textcircled{H}_{\lambda_P}$$

It should be noted that if the poles are too close together numerical difficulties preclude accuracy in the calculation. We have found that if ρ is chosen anywhere within the limits $\frac{N}{20} < \rho < (\text{Im}\lambda_p - 1)$ the calculation for $f(\theta)$ is not perceptibly changed.

Appendix C: Recovering the Deflection Function
from Low Resolution Data

This Appendix will present some thoughts on fixing the

scale of L for the deflection function in low resolution

experiments.

The two deflection functions in figure 47 should produce

the corresponding cross sections in figure 48.
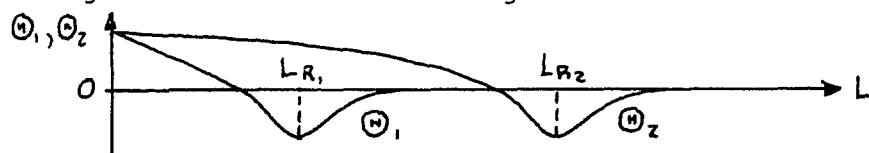
Figure 47: two deflection functions with identically
shaped attractive wells.
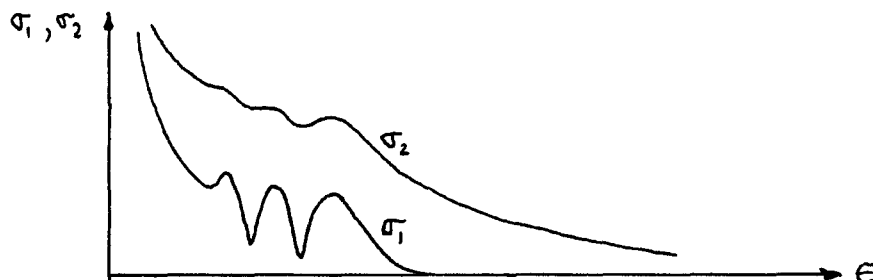
Figure 48: the differential cross sections corresponding
to the two deflection functions in figure 47.

The shapes of the attractive wells of Θ_1 , and Θ_2 are

identical so that the periodicities of the low frequency

oscillations in both cross sections are the same. However

the smaller repulsive contribution of Θ_1 leads to better

resolution of the interference phenomena and smaller total

cross section. This suggests two possibilities.

If our understanding of smearing in the data is put on a

quantitative basis, the degree of experimental resolution of

the low frequency component may itself aid in a determination of L_R . Further, if accurate absolute cross sections can be measured then Ⓗ$_1$ and Ⓗ$_2$ should definitely be distinguishable. Along this same line a third, and more feasible, idea suggests itself.

If, in addition to the low resolution relative differential cross section, the relative total cross section[46] could be measured for the low resolution system as well as for a high resolution system (for instance $5eV$ $H^+ + Ar$) then the calculation[47] could be adjusted such that:

$$\begin{pmatrix} Calculated \ \sigma_{Total} \\ for \ low \ resolution \\ system \end{pmatrix} = \frac{\begin{pmatrix} Experimental \ \sigma_{Total} \\ for \ low \ resolution \\ system \end{pmatrix}}{\begin{pmatrix} Experimental \ \sigma_{Total} \\ for \ high \ resolution \\ system \end{pmatrix}} \times \begin{pmatrix} Calculated \ \sigma_{Total} \\ for \ high \ resolution \\ system \end{pmatrix}$$

This additional requirement coupled with a good fit to the low frequency oscillations might well determine L_R in the deflection function. The basic difficulty in this procedure is that both relative total cross section measurements must be carried out under <u>exactly</u> the same experimental conditions.

Appendix D: <u>The Non-Crossing Rule</u>

In this Appendix we will show why the adiabatic curves can not cross. To do this we will follow the treatment of Landau and Lifshitz.[48]

Let us suppose that the system is at an internuclear separation R_o where the adiabatic binding energy curves $E_1^a(R)$ and $E_2^a(R)$ are close but not equal. Let us now see whether we can displace the separation coordinate, R, by a small amount ΔR so that the eigenvalues are equal, i.e.:

$$E_1^a(R_o + \Delta R) = E_2^a(R_o + \Delta R) \equiv E(R_o + \Delta R)$$

To investigate this question we shall use degenerate perturbation theory. Accordingly, we let

$$(D1) \qquad \varphi = C_1 \varphi_1 + C_2 \varphi_2$$

where

$$H_{el}\, \varphi_1 = E_1^a \varphi_1$$

$$H_{el}\, \varphi_2 = E_2^a \varphi_2$$

and

$$(D2) \qquad \left(H_{el} + \Delta V \right) \varphi = E \varphi$$

Where $\Delta V = \Delta R \left. \dfrac{d H_{el}}{d R} \right|_{R_o}$ is the small perturbation operator re-

sulting from a displacement of the system by an amount ΔR . Substitution of D1 into D2 gives

(D3) $\quad C_1 \left(E_1^a + \Delta V - E \right) \varphi_1 + C_2 \left(E_2^a + \Delta V - E \right) \varphi_2 = 0$

Premultiplying equation D3 by φ_1^* and integrating over electron coordinates we find:

(D4) $\quad C_1 \left(E_1^a + V_{11} - E \right) + C_2 V_{12} = 0$

with

$$V_{11} \equiv \langle \varphi_1 | \Delta V | \varphi_1 \rangle$$

$$V_{12} \equiv \langle \varphi_1 | \Delta V | \varphi_2 \rangle$$

Doing the same with φ_2^* results in

(D5) $\quad C_1 V_{21} + C_2 \left(E_2^a + V_{22} - E \right) = 0$

with

$$V_{22} \equiv \langle \varphi_2 | \Delta V | \varphi_2 \rangle$$

$$V_{21} \equiv \langle \varphi_2 | \Delta V | \varphi_1 \rangle$$

Since $\Delta V^* = \Delta V$ we have,

$$V_{21}^* = V_{12}$$

and let us assume V_{12} is real so that $V_{21} = V_{12}$.

The condition for the solution of the simultaneous equations D4 and D5 is that the determinant of the system

vanish:

$$\begin{vmatrix} E_1^a + V_{11} - E & V_{12} \\ V_{12} & E_2^a + V_{22} - E \end{vmatrix} = 0$$

So that

$$E = \frac{1}{2}\left(E_1^a + E_2^a + V_{11} + V_{22}\right) \pm \sqrt{\frac{1}{4}\left(E_1^a - E_2^a + V_{11} - V_{22}\right)^2 + V_{12}^2}$$

Consequently,

$$\sqrt{\frac{1}{4}\left(E_1^a - E_2^a + V_{11} - V_{22}\right)^2 + V_{12}^2} = 0$$

That is

(D6) $$E_1^a - E_2^a + V_{11} - V_{22} = 0$$

and

(D7) $$V_{12} = 0$$

We have, in equations D6 and D7, placed two conditions on the term ΔR which can not, in general be satisfied.

The only way in which D6 and D7 can be simultaneously true is if $V_{12} = 0$ for some other reason. This is the case if φ_1 and φ_2 have different molecular symmetry.[49]

The results of this appendix may then be summarized. The curves for which H_{el} is diagonal, that is the adiabatic

curves, may not cross if the molecular symmetry of the two states is the same; conversly, if $H_{e\ell}$ is not diagonal for some representation (e.g. the diabatic) the curves can cross since equation D7 does not apply.

Appendix E: <u>Mathematical Detail</u>

In order to derive,

$$\langle \varphi_K | \frac{d}{dR} | \varphi_J \rangle = \frac{\langle \varphi_K | \left(\frac{d\, H_{el}}{dR} \right) | \varphi_J \rangle}{E_J - E_K}$$

we have used the relation:

(E1) $\qquad \langle \varphi_K | H_{el} \frac{d}{dR} | \varphi_J \rangle = E_K \langle \varphi_K | \frac{d}{dR} | \varphi_J \rangle$

We shall, in this Appendix, establish equation E1. Consider

(E2) $\qquad \int \nabla_r \left[\left(\frac{d}{dR} \varphi_J \right) \cdot \nabla_r \varphi_K^* \right] d^3r$

$$= \int \left(\nabla_r \frac{d}{dR} \varphi_J \right) \cdot \left(\nabla_r \varphi_K^* \right) d^3r + \int \left(\frac{d}{dR} \varphi_J \right) \cdot \left(\nabla_r^2 \varphi_K^* \right) d^3r$$

and also

(E3) $\qquad \int \nabla_r \left[\left(\nabla_r \frac{d}{dR} \varphi_J \right) \cdot \varphi_K^* \right] d^3r$

$$= \int \left(\nabla_r^2 \frac{d}{dR} \varphi_J \right) \cdot \varphi_K^* \, d^3r + \int \left(\nabla_r \frac{d}{dR} \varphi_J \right) \cdot \left(\nabla_r \varphi_K^* \right) d^3r$$

So, from equations E2 and E3, we have:

$$\int \nabla_r \left[\left(\frac{d}{dR} \varphi_J \right) \cdot \nabla_r \varphi_K^* \right] d^3r = \int \nabla_r \left[\left(\nabla_r \frac{d}{dR} \varphi_J \right) \cdot \varphi_K^* \right] d^3r$$

(E4)

$$- \int \left(\nabla_r^2 \frac{d}{dR} \varphi_J \right) \cdot \varphi_K^* \, d^3r + \int \left(\frac{d}{dR} \varphi_J \right) \cdot \left(\nabla_r^2 \varphi_K^* \right) d^3r$$

The term on the left and the first term on the right of equation E4 may be converted to surface integrals, so that:

$$\oint_S \left[\left(\frac{d}{dR} \varphi_J \right) \cdot \nabla_r \varphi_K^* \right]_{normal} \cdot dS \;-\; \oint_S \left[\left(\nabla_r \frac{d}{dR} \varphi_J \right) \cdot \varphi_K^* \right]_{normal} \cdot dS$$

$$= \int \left(\nabla_r^2 \frac{d}{dR} \varphi_J \right) \cdot \varphi_K^* \, d^3r \;+\; \int \left(\frac{d}{dR} \varphi_J \right) \cdot \left(\nabla_r^2 \varphi_K^* \right) d^3r$$

But since the integrations, $\int d^3r$, are over all space the surface integrals may be taken at infinity where the integrands vanish; consequently:

(E5)
$$\int \left(\nabla_r^2 \varphi_K^* \right) \frac{d}{dR} \varphi_J \, d^3r \;=\; \int \varphi_K^* \, \nabla_r^2 \frac{d}{dR} \varphi_J \, d^3r$$

Using the result that:

$$H_{el}^* \varphi_K^* = E_K^* \varphi_K^* = H_{el} \varphi_K^* = E_K \varphi_K^*$$

as well as the fact that $V(r,R)$ is a scalar, we find:

$$E_K \left\langle \varphi_K \left| \frac{d}{dR} \right| \varphi_J \right\rangle = \left\langle \varphi_K \left| H_{el} \frac{d}{dR} \right| \varphi_J \right\rangle$$

FOOTNOTES AND REFERENCES

1. Champion, R. L.; Doverspike, L. D.; Rich, W. G.; Bobbio, S.M.
   Phys. Rev. A $\underline{2}$, 2327 (1970)

2. Ford, K. W.; Wheeler, J. A.
   Ann. Phys. (n. Y.) $\underline{7}$, 259 (1959); $\underline{7}$, 287 (1959)

3. Remler, E. A.
   Phys. Rev. A $\underline{3}$, 1949 (1971)

4. The most useful reference to the inversion technique is:
   Vollmer, G.
   Z. Physik $\underline{226}$, 423 (1969)
   Included to give due credit to an earlier publication is:
   Vollmer, G.; Krüger, H.
   Phys. Letters 28A, 165 (1968)

5. Olson, R. E.; Smith, F. T.
   Phys. Rev. A $\underline{3}$, 1607 (1971)

6. Sidis, V.; Lefebvre-Brion, H.
   to be published in
   J. Phys. B

7. Delos, J.
   "A Semiclassical Study of the Potential Crossing Problem in
   Atomic Collision Theory."
   (doctoral dissertation, M. I. T. 1970)

8. Aberth, W.; Peterson, J. R.
   Rev. Sci. Instr. $\underline{38}$, No. 6, 745 (1967)

9. Paul, W.; et al
   Z. Phys. $\underline{152}$, 143 (1958)

10. For a small region in the immediate vicinity of the entrance
    and exit slits, the gas target may not be in equilibrium,
    but rather manifest some slight streaming motion. The energy
    associated with this motion should be quite small however.

11. Champion, R. L.; Doverspike, L. D.
    J. Chem. Phys. $\underline{49}$, 4321 (1968)

12. Ioup, G. E.; Thomas, B. S.
    J. Chem. Phys. $\underline{50}$, 5009 (1969)

13. Schiff, L. I.
Quantum Mechanics, 2nd edition
McGraw-Hill Book Company, New York, 1955, p. 105

14. The reference used for the JWKB method was basically:
Powell, J. L.; Crasemann, B.
Quantum Mechanics
Addison-Wesley Publishing Company, Inc., Mass., 1961, p. 140

15. Sidis, V.
In a private communication, states that he has calculated
the ground state potential for the (ArH)$^+$ system and has
found no other states which cross it at low energy.

16. Partial waves may be thought of as having velocity (increased,
decreased) and wave-length (decreased, increased) at small
values of R for (attractive, repulsive) potentials and thus
show (advanced, retarded) phase as R becomes infinite after
the interaction.

17. Marchi; R. P.; Mueller, C. R.
J. Chem. Phys. 38, 740 (1963)

18. The paper of reference 1) For a more sophisticated approach
using the same general method the reader should see:
Mittmann, H. U.; Weise, H. P.; Ding, A.; Henglein, A.
To be published in
Z. Naturforschung

19. Bernstein, R. B.
Molecular Beams, edited by John Ross, Vol. X
Interscience Publishers, N. Y., 1966, p. 75.

20. Goldstein, H.
Classical Mechanics
Addison-Wesley Publishing Company, Inc., Mass., 1959, p. 73.

21. See Appendix A for classical orbiting, an important exception.

22. Landau, L. D.; Lifshitz, E. M.
Quantum Mechanics, 1st edition
Addison-Wesley Publishing Company, Inc., Mass., 1965 p. 401.

23. Berry has accomplished this by parameterizing the attractive phase, $\beta_x(\ell)$, in cubic form. The reference is:
Berry, M. V.
Proc. Phys. Soc. (London) 89, 479 (1966).

24. Regge, T.
Nuovo Cimento 14, 951 (1959).

25. Squires, E. J.
Complex Angular Momenta and Particle Physics
W. A. Benjamin, Inc., N. Y., 1963, p. 4.

26. For example, for a hard sphere of radius a:

$$\lambda \equiv \lambda_{core} = \sqrt{2ME}\left(\frac{a}{\hbar}\right) - \frac{1}{2}$$

27. Rich, W. A.; Bobbio, S. M.; Champion, R. L.; Doverspike, L. D.
To be published in
Phys. Rev. A.

28. Wolniewicz, L.
J. Chem Phys. 43, 1087 (1965).

29. To see that $E_K^a(R)$ cannot be degenerate with $E_J^a(R)$ if φ_K and φ_J have the same molecular symmetry, turn to Appendix D.

30. Lichten, W.
Phys. Rev. 131, 229 (1963; 139, A27 (1965); 164, 131 (1967).

31. Smith, F. T.
Phys. Rev. 179, 111 (1969).

32. Gilbert, T. L.; Wahl, A. C.
J. Chem. Phys. 47, 3425.

33. Equations IV-11 are derived from equations IV-10 by exactly the same type of partial wave expansion used to obtain equation III-6 from equation III-2 (where the additional assumption of spherical symmetry for V_{12} and V_{21} has been invoked). Clearly then, V_1 and V_2 are ℓ dependent as:

$$V_{1,2}(R) = V_{1,2}(R, \ell=0) + \frac{\ell(\ell+1)}{2MR^2}$$

and the set IV-11 must be solved for each value of ℓ.
In order to minimize notational complication as well as to be consistent with the Delos dissertation[7] we have deleted explicit mention of the ℓ parts; the reader should, however, realize that the ℓ dependence is implicitly included.

34. If the reader is not interested in my outline of Delos's work he may skip to the results of this section, beginning on page 108.

35. To prove unitarity for instance:

$$i\frac{d}{dt} G = HG$$

$$\left(i\frac{d}{dt} G\right)^\dagger = G^\dagger H^\dagger = G^\dagger H = -i\frac{d}{dt} G^\dagger$$

So that

$$i\frac{d}{dt}\left(G^\dagger G\right) = G^\dagger H G - G^\dagger H G = 0$$

and

$$G^\dagger G = \text{constant} = G^+(\mathcal{C}_T, \mathcal{C}_T)\, G(\mathcal{C}_T, \mathcal{C}_T) = 1$$

36. Please note, the origin has been shifted to coincide with the crossing.

37. Delos, in a private communication, states that the quantities Z, Γ_1, and Γ_2 converge to their limits in an oscillatory fashion, and that the amplitude of oscillation is damped more quickly than 1/t. We have not thoroughly examined this convergence since, to test our integration method, we have reproduced the numerical results of Delos[7] to four significant figures (for values of b and ϵ in the vicinity of the actual ones used for the (NeHe)$^+$ cross section calculation).

38. The one exception to this is in the special case that the signs of the forces dV_1/dR and dV_2/dR are different at the crossing point.

39. Please recall that the JWKBL phase shifts are proportional to :

$$\int_{R_T}^{\infty} dR .$$

40. Please recall that the rainbow angle is to the right of the largest angle maximum in the cross section. See, for example, figure 17.

41. The actual program utilized Hamming's predictor-corrector method.

42. Many slowly and smoothly changing conditions could affect this decay rate, for example: (1) the primary beam intensity, (2) the target gas pressure, (3) the efficiency of the entire detection system as the elastically scattered product loses energy in the laboratory coordinates with increasing scattering angle. Some discrepancy may also enter in our treatment of the data: e.g., for a beam strongly focused in the vertical direction our reaction volume correction (discussed in Section IIB) would not be correct.

43. The Landau-Zener method assumes that the approximations:

$$\eta_a + \Gamma_1 = \eta_a \qquad ; \qquad \eta_a - \Gamma_2 = \eta_d$$

are valid for all values of ℓ . It, therefore, does not take into account phase changes in the vicinity of the crossing. See, for example:
Marchi, R. P.
Phys. Rev. <u>183</u>, 185 (1969).

44. Corresponding to the negative attractive pulse caused in the deflection function by first quadrant singularities, fourth quadrant poles result in a positive pulse in $\Theta(\ell)$.

45. Private communication of E. A. Remler.

46. The relative total cross section for systems where only one channel is open (or manifestly dominant) may be found by measuring the difference in the ion beam intensity at $O°$ with the scattering gas in and with it out.

47. The optical theorem:

$$\sigma_{Total} = \frac{4\pi}{k} \, Im \, f(o)$$

would provide a convenient way of retrieving the total cross section from existing computer programs.

48. Reference 22, p. 263.

49. Reference 22, p. 264.

VITA

The author, Stephen Michael Bobbio, was born in Norfolk, Virginia, on July 28, 1943. He completed his elementary and secondary education in Detroit, Michigan. He received a bachelor of science degree in Physics from the University of Detroit, Detroit, Michigan in 1965. After receiving his bachelor's degree he continued at the University of Detroit until he received his master of science degree in Physics in 1967. While at the University of Detroit he became a member of Sigma Pi Sigma (physics honor society). In August 1967 he married the former Miss Betty Mathis. In September of 1967 he began his work toward the doctor of philosophy in Physics degree at the College of William and Mary in Williamsburg, Virginia. While at William and Mary he was supported by departmental teaching and research assistantships.